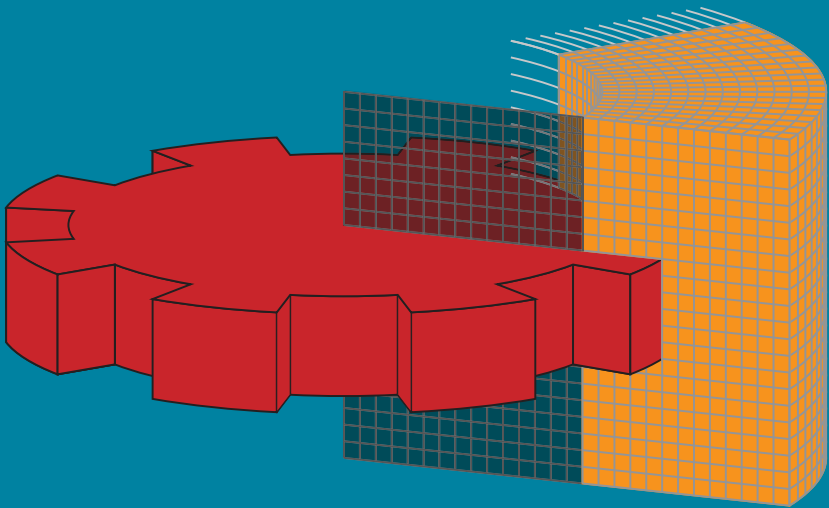


Cylindrical and Nonconformal Material Interfaces in the Finite Integration Technique

Stefan Kirsch



Cylindrical and Nonconformal Material Interfaces in the Finite Integration Technique

vorgelegt von
Dipl.-Ing. Stefan Kirsch
geb. in Soest

von der Fakultät IV – Elektrotechnik und Informatik
der Technischen Universität Berlin
zur Erlangung des akademischen Grades

DOKTOR DER INGENIEURWISSENSCHAFTEN
— DR.-ING. —

genehmigte Dissertation

Promotionsausschuss:

Vorsitzender:	Prof. Dr.-Ing. Ronald Plath,	TU Berlin
Gutachter:	Prof. Dr.-Ing. Rolf Schuhmann,	TU Berlin
	Prof. Dr. rer. nat. habil. Ursula van Rienen,	Universität Rostock
	Prof. Dr.-Ing. Wolfgang Heinrich,	TU Berlin

Tag der wissenschaftlichen Aussprache: 8. April 2016

Except otherwise noted, this work is
© 2016 **Stefan Kirsch**,
under a *Creative Commons Attribution* license:
<http://creativecommons.org/licenses/by/4.0/>



Dedicated to Henri

Contents

Abstract	IX
Kurzfassung	XI
Acknowledgment	XIII
1 Introduction	1
1.1 Motivation	1
1.2 Contribution	2
1.3 Outline	2
2 Basic Principles	5
2.1 Electromagnetic Field Theory	5
2.1.1 Maxwell's Equations	5
2.1.2 Material Relations	6
2.1.3 Continuity of Field Components	7
2.1.4 Derived Formulations	7
2.2 Finite Integration Technique	8
2.2.1 Maxwell's Grid Equations	9
2.2.2 Discrete Material Relations	14
2.2.3 Boundary Conditions	15
2.2.4 Cartesian Mesh	15
2.2.5 Cylindrical Mesh	17
2.3 Temporal Discretization	23
2.3.1 The Leapfrog Algorithm	24
2.3.2 Convergence	25
2.3.3 Newmark-Beta	26
3 Time Domain Methods on Cylindrical Meshes	29
3.1 Criteria for Numerical Stability	30
3.1.1 Standard 3D Mesh Cell	32
3.1.2 Body of Revolution Mesh Cell	34
3.1.3 Practical Implications	37

3.2	Compensation of Degraded Time Step Size	38
3.2.1	The Coupled Multi-Mode Method	39
3.2.2	The Hybrid Newmark-Beta Method	44
3.2.3	Combination of Coupled Multi-Mode with Hybrid Newmark-Beta	51
3.2.4	Validation and Comparison by Numerical Example	52
3.3	Summary	59
4	Nonconformal Material Interfaces	61
4.1	The Conformal Case	62
4.2	The Nonconformal Case	64
4.2.1	Artificially Induced Application of Conventional Coefficients	66
4.2.2	Bulk Material	67
4.2.3	Implications of the Generalized Material Coefficient	68
4.3	Validation	70
4.3.1	Angle Dependence and Introduced Error	72
4.3.2	Impact on Simulation Results	72
4.3.3	Sensitivity Analysis	75
4.4	Estimation of Field Information	76
4.4.1	Iterative Approach	78
4.4.2	Nondiagonal Matrix Approach	81
4.5	Summary and Concluding Remarks	85
4.5.1	Remarks	87
5	Practice-Oriented Applications	91
5.1	FDTD on Cylindrical Meshes	91
5.1.1	Microgear Resonator	92
5.1.2	Pierced Microdisk	96
5.2	Time Domain Magnetoquasistatics with Nonconformal Material Interfaces	99
6	Summary and Outlook	105

A	Maxwell's Grid Equations for Bodies of Revolution	109
B	Stability and Accuracy of Newmark-Beta Schemes	113
B.1	Discrete Dispersion Relation	113
B.2	Numerical Stability	114
B.3	Accuracy	114
C	Detailed Deduction of Convergence Rates	117
C.1	Generalized Material Coefficient	117
C.2	Conventional Material Coefficient	118
D	Extended Example of Pierced Microdisk	121
	Nomenclature	123
	General and Mathematical Symbols	123
	Space- and Time-Continuous Field Theory	123
	(Time-Discrete) Finite Integration Technique	125
	Bibliography	129
	External Literature	129
	Own Publications	136
	Own Talks and Poster Presentations	136
	Software	138

Abstract

The present work addresses a fundamental issue of electromagnetic simulations by means of the Finite Integration Technique (FIT). This method is typically applied to Cartesian and, therefore, geometrically inflexible computational meshes. In order to achieve a high level of accuracy in a reasonable amount of time, the FIT commonly requires the simulated object's material interfaces to conform in a certain way to the mesh facets. Since this narrows its scope of application, we discuss two systematically different possibilities to transfer the expected accuracy from the conformal Cartesian case to other areas.

On one hand, we abandon the Cartesian mesh in favor of a cylindrical one, which naturally conforms to many circularly shaped objects. In this regard, our main objective is the investigation and compensation of time domain methods' limitations that arise specifically due to inherent properties of the cylindrical mesh system. On the other hand, we present a generalized theoretical framework to enable highly accurate material modeling even in the event of nonconformal interfaces. Different means of applying it to practical simulations are proposed.

Each introduced method is validated by means of numerical examples. Furthermore, a set of practice-oriented applications allows for comparing them to commercial simulation software and stresses their effectiveness.

Kurzfassung

Gegenstand der vorliegenden Arbeit ist die Behandlung eines grundlegenden Problems elektromagnetischer Feldsimulation auf Basis der Methode der Finiten Integration. Diese Methode wird üblicherweise auf kartesischen, und daher aus geometrischer Sicht unflexiblen, Rechengittern angewendet. Für ein hohes Maß an Genauigkeit in Verbindung mit moderatem Rechenaufwand wird in der Regel vorausgesetzt, dass die Grenzschichten zwischen verschiedenen Materialien in gewisser Weise konform mit Gitterflächen sind. Da dies die Anwendbarkeit des Verfahrens in der Praxis stark einschränken kann, werden im Verlauf der Arbeit zwei systematisch verschiedene Möglichkeiten aufgezeigt, mit deren Hilfe sich die zu erwartende Genauigkeit des konformen, kartesischen Falls auf andere Bereiche übertragen lässt.

Zum einen wird die Abkehr von kartesischen zu Gunsten zylindrischer Gitter untersucht, die sich auf natürliche Weise zu einer Reihe von kreisförmigen Objekten konform verhalten. In dieser Hinsicht gilt das Hauptaugenmerk der Untersuchung und dem Ausgleich sich durch inhärente Eigenschaften des Zylindergitters ergebender Einschränkungen für Zeitbereichsverfahren. Zum anderen wird ein verallgemeinertes theoretisches Konzept eingeführt, in dessen Rahmen eine sehr genaue Abbildung nichtkonformer Materialgrenzen auf das Rechengitter möglich ist. Darauf aufbauend sind verschiedene Möglichkeiten zur Umsetzung dieses Konzepts in Simulationen gegeben.

Jede im Laufe der Arbeit vorgestellte Methode wird anhand numerischer Rechenbeispiele validiert. Darüber hinaus heben durch Praxisanwendungen motivierte Beispiele die Effektivität der Verfahren hervor, insbesondere durch den Vergleich zu kommerzieller Simulationssoftware.

Acknowledgment

I wish to express my sincere gratitude to all people who contributed to this thesis. In particular, I would like to thank

- Prof. Rolf Schuhmann, for providing an excellent working environment, for enabling the participation in conferences, and for his encouragement to self-dependent research while always having an open ear.
- Prof. Ursula van Rienen and Prof. Wolfgang Heinrich for co-reviewing this thesis and Prof. Ronald Plath for taking the chair of the committee.
- Dr. Bastian Bandlow for proofreading the manuscript and his numerous and valuable suggestions.
- all former and current colleagues at the chair of *Theoretische Elektrotechnik* in Paderborn and Berlin for countless technical and also non-technical discussions.
- my family and friends in Soest.

Last but not least, my heartfelt appreciation goes to my fiancée Daniela Brauner for her constant support, motivation and patience.

Introduction

1.1. Motivation

Prior to the invention, advancement and massive deployment of modern computer systems, the design process of electromagnetic components relies predominantly on building prototypes and determining their characteristic properties by means of measurements. Nowadays, the availability of affordable and powerful computer hardware has led to the increasing popularity of simulation software as a supplemental tool in the development process. As a consequence, the expensive and time-consuming prototype construction becomes more and more obsolete. In comparison to conventional measurements, simulation software offers several advantages, like non-intrusive or non-destructive means to obtain quantities of interest or the ability to eliminate undesired feedback of the measurement equipment to the device under test.

In order to model electromagnetic behavior in a manner that is machine-processable without strong simplifications, the governing set of partial differential equations, i.e. *Maxwell's equations*, needs to be subject to a process called *discretization*. A very popular method for this purpose is the Finite Integration Technique (FIT), which is developed by Thomas Weiland in 1977 [Wei77]. Since its initial publication, ongoing research has extended the method's scope to the entire range of the electromagnetic frequency spectrum, the inclusion of countless enhancements and different kinds of underlying mesh systems.

Specifically the last point is what the present thesis' main focus is on. To motivate its importance, we use the analogy of cells in a computational mesh with color pixels in a TV screen. Real life objects get represented on the TV screen by means of a finite and structured set of rectangular pixels. In principle, the same is true for typical mesh representations of simulated objects, only in three dimensions, i.e. with voxels instead of pixels. In both cases, this works remarkably well if the represented object's geometry inherently conforms well to the employed mesh, even with small numbers of pixels. If it does not, i.e. the mesh is nonconformal, the common strategy is to increase the number of pixels. The same what makes a television set with millions of pixels expensive is what makes an accurate simulation on a rectangular (Cartesian) mesh system slow or hardware-demanding.

1.2. Contribution

Since there exist objects, which are accurately mapped on a coarse mesh based on Cartesian coordinate lines, it seems obvious that different classes of objects also find an accurate representation on a different mesh system. Without sacrificing favorable properties of the Finite Integration Technique, these mesh systems cannot be chosen arbitrarily, i.e. material conforming in general. However, orthogonal coordinate systems as foundation of computational meshes, even if they are curvilinear, are permitted and well-documented. Specifically the cylindrical coordinate system enables a large class of technically relevant objects to be described much better than in Cartesian coordinates. Therefore, cylindrical meshes take up a vital part in the present work.

To illustrate their peculiarities, we stay in the TV screen analogy mentioned above. Accordingly, we modify each pixel's shape to conform to lines of a polar coordinate system, with its origin in the middle of the screen. Inevitably, the pixels near the origin are much smaller in their azimuthal extent than those at the outer perimeter. They would be technically challenging to manufacture. Even though computational cylindrical meshes in the FIT are implementable straightforwardly, they impose tedious restrictions to time domain simulation algorithms operating on top of them. We suggest methods to formally describe these restrictions and also to alleviate them based on hybrid implementations of nonstandard time integration schemes.

The modification of the pixel shape is a practicable method if the object to be represented by the mesh is known a priori and also suitable within narrow constraints. In other cases it would be advisable to stick to the approved and efficient to implement rectangular approach. However, a highly resolved mesh is not always a viable option due to cost restrictions in terms of hardware resources. For this reason, we first of all quantify the error made by the approximation of nonconformal objects by Cartesian meshes. Emerging from the framework we use to describe the discretization error, a method that is classifiable as a *subpixel smoothing technique* is derived and used to improve the accuracy on coarse, Cartesian meshes. In the context of the TV screen analogy, this can be interpreted as relieving pixels from their limitation of showing only one color at a time.

1.3. Outline

After giving a brief introduction to the basic principles we make use of in the course of this thesis (Chapter 2), we turn towards the time domain formulation of the

Finite Integration Technique on different kinds of cylindrical meshes in Chapter 3. A method to obtain conditions for numerical stability is applied to each of them. Subsequently, different methods for rectifying the stability analysis' outcome are developed and demonstrated by means of a simple numerical example with known reference solution.

The focus of Chapter 4 lies on more versatile and efficient to implement Cartesian meshes. We thoroughly investigate the implications of nonconformal material interfaces with respect to the Finite Integration Technique's accuracy. The abstract concept of *generalized material modeling* is introduced. We propose two distinctive means of using it in practice and validate their effectiveness. This chapter concludes with some important remarks on the method's extensibility to other use cases and limitations thereof.

To show the so far introduced approaches' usefulness beyond academic examples, we apply them to more practically oriented structures and time integration schemes in Chapter 5. After a conclusion that explicitly states the present work's results in a broader context, some appendix sections follow with the aim of giving comprehensive insight to concepts used or derived throughout this thesis.

Basic Principles

The aim of this chapter is to provide the basic framework for describing and calculating electromagnetic phenomena. Therefore, we first of all state *Maxwell's equations* and other well-known analytical identities in Section 2.1. By means of the *Finite Integration Technique* (cf. Section 2.2, [Wei77]), their representation in discrete space, called *Maxwell's grid equations*, is obtained. Since different kinds of computational meshes are employed in this work, we perform the spatial discretization in a general orthogonal coordinate system (u, v, w) , which is subsequently replaced by cylindrical (ρ, φ, z) or Cartesian (x, y, z) coordinates, respectively.

In order to obtain a space- and time-discrete, and thus machine processable formalism, Maxwell's grid equations' continuous time dependence is approximated on a discrete time axis in Section 2.3.

2.1. Electromagnetic Field Theory

The content of this section is a brief aggregation of fundamental concepts of electromagnetic field theory with focus on those aspects that are of importance for this thesis. For a more comprehensive insight, the reader is referred to the literature, e.g. [Jac98; Hen15], which also serve as guideline for the following deductions.

2.1.1. Maxwell's Equations

In 1865, James Clerk Maxwell publishes a set of partial differential equations [Max65] that quantitatively describe the relations between, and sources of electric and magnetic fields with respect to both space and time. Over the years, his original work is reformulated several times, which gives rise to Maxwell's equations in their nowadays commonly known form:

$$\oint_{\partial A} \vec{E}(\vec{r}, t) \cdot d\vec{s} = - \iint_A \frac{\partial \vec{B}(\vec{r}, t)}{\partial t} \cdot d\vec{A} \quad (2.1a)$$

$$\oint_{\partial A} \vec{H}(\vec{r}, t) \cdot d\vec{s} = \iint_A \left(\frac{\partial \vec{D}(\vec{r}, t)}{\partial t} + \vec{J}(\vec{r}, t) \right) \cdot d\vec{A} \quad (2.1b)$$

$$\oiint_{\partial V} \vec{D}(\vec{r}, t) \cdot d\vec{A} = \iiint_V \rho_q(\vec{r}, t) dV \quad (2.1c)$$

$$\oiint_{\partial V} \vec{B}(\vec{r}, t) \cdot d\vec{A} = 0 \quad (2.1d)$$

For the sake of brevity, we omit the explicit mention of space and time dependence throughout this thesis. The occurring quantities' symbols are assigned in the style of typical literature. For a detailed declaration the reader is referred to the Nomenclature on page 123. The current density \vec{J} comprises different parts like the movement of electrons due to an electric field (\vec{J}_c), impressed source currents (\vec{J}_s) or convection currents as a result of space charge densities moving at a certain speed (not regarded in this thesis).

By means of vector calculus methods, specifically Stokes' and Gauss' theorems [Coro8], it is possible to convert (2.1) into an equivalent differential formulation:

$$\nabla \times \vec{E} = -\frac{\partial \vec{B}}{\partial t} \quad (2.2a)$$

$$\nabla \times \vec{H} = \frac{\partial \vec{D}}{\partial t} + \vec{J} \quad (2.2b)$$

$$\nabla \cdot \vec{D} = \rho_q \quad (2.2c)$$

$$\nabla \cdot \vec{B} = 0 \quad (2.2d)$$

2.1.2. Material Relations

From a strictly mathematical point of view, Maxwell's equations, as given in (2.1) and (2.2), are two sets of mutually independent partial differential equations. However, there are physical relationships between the occurring quantities. Without further assumptions, they make all four equations dependent on each other. In general, these relationships are:

$$\vec{D} = \varepsilon \vec{E} \quad (2.3a)$$

$$\vec{B} = \mu \vec{H} \quad (2.3b)$$

$$\vec{J}_c = \sigma \vec{E} \quad (2.3c)$$

In the scope of this work, the material coefficients $\varepsilon = \varepsilon_0 \varepsilon_r$ (permittivity), $\mu = \mu_0 \mu_r$ (permeability) and σ (conductivity) are considered linear and time invariant. The quantities that are indexed with r are the relative permittivity/permeability and are material dependent.

2.1.3. Continuity of Field Components

The behavior of electromagnetic fields at interfaces from one domain to another follows directly from (2.1) under simple geometric considerations [Jac98]. Let \vec{n} be the normal vector of an arbitrarily shaped material interface \mathcal{J} pointing from domain a into domain b . In order for the fields to fulfill Maxwell's equations, they need to obey the following continuity conditions:

$$\vec{n} \times (\vec{E}_b - \vec{E}_a)|_{\mathcal{J}} = 0 \quad (2.4a)$$

$$\vec{n} \cdot (\varepsilon_b \vec{E}_b - \varepsilon_a \vec{E}_a)|_{\mathcal{J}} = \varsigma_q \quad (2.4b)$$

$$\vec{n} \times (\vec{H}_b - \vec{H}_a)|_{\mathcal{J}} = \vec{K} \quad (2.4c)$$

$$\vec{n} \cdot (\mu_b \vec{H}_b - \mu_a \vec{H}_a)|_{\mathcal{J}} = 0 \quad (2.4d)$$

Under the assumption of vanishing surface charge density ς_q and surface current density \vec{K} , the above equations' predication is that the electric and magnetic field's tangential components are continuous across \mathcal{J} . Their normal components jump by the ratio of the involved permittivities or permeabilities, respectively.

2.1.4. Derived Formulations

By making further assumptions, Maxwell's equations are transformed into more problem specific formulations. In the following, those of interest in the scope of this thesis are introduced.

2.1.4.1. Poisson's Equation for Electrostatics

In case only electric quantities are of interest and the time dependence is negligible, (2.2) reduces to the following set of equations:

$$\nabla \times \vec{E} = 0 \quad (2.5a)$$

$$\nabla \cdot \vec{D} = \rho_q \quad (2.5b)$$

The ansatz $\vec{E} = -\nabla\Phi$ with a scalar potential Φ satisfies (2.5a) directly and, substituted into (2.5b), leads to a Poisson equation for Φ :

$$\nabla \cdot \varepsilon \nabla \Phi = -\rho_q \quad (2.6)$$

2.1.4.2. Diffusion Equation for Magnetoquasistatics

A possible simplification of Maxwell's equations is the magnetoquasistatic approximation $\frac{\partial \vec{D}}{\partial t} = 0$, which is valid if $\sigma |\vec{E}| \gg \left| \frac{\partial \vec{D}}{\partial t} \right|$, i.e. if the electric field can be referred to as *slowly varying* with respect to the conduction current's amplitude. The magnetic flux density is obtained by means of a magnetic vector potential as $\vec{B} = \nabla \times \vec{A}$, so that (2.2d) is implicitly fulfilled. For a domain that includes no source currents and after Lorenz gauging [Jac98], Maxwell's equations lead to a diffusion equation:

$$\nabla^2 \vec{A} - \mu\sigma \frac{\partial \vec{A}}{\partial t} = 0 \quad (2.7)$$

2.1.4.3. Electromagnetic Wave Equation

If only the space charge density ρ_q is neglected, the electromagnetic wave equation is obtained by substituting (2.2b) into (2.2a):

$$\nabla^2 \vec{E} + \varepsilon\mu \frac{\partial^2 \vec{E}}{\partial t^2} + \mu \frac{\partial \vec{J}}{\partial t} = 0 \quad (2.8)$$

In some cases the dependence on time is strictly sinusoidal at a distinct frequency ω or can be decomposed into a series of sines and cosines. Then it is advantageous to express the time dependence by $e^{j\omega t}$ and, thereby, obtain the wave equation for the field's and current's complex amplitudes:

$$\nabla^2 \underline{\vec{E}} - \omega^2 \varepsilon \mu \underline{\vec{E}} + j\omega \mu \underline{\vec{J}} = 0 \quad (2.9)$$

The time domain quantities result from their respective complex amplitudes by:

$$\vec{E} = \Re \{ \underline{\vec{E}} e^{j\omega t} \} \quad (2.10)$$

2.2. Finite Integration Technique

The formulations derived in Section 2.1.4, despite being more problem-specific than the general form of Maxwell's equations, still are of very limited use in real-world applications. The governing partial differential equations (PDE) usually allow for closed form solutions only if vast approximations and simplifications of the underlying problem are made.

For that reason, we are interested in ways of systematically approximating electromagnetic problems and their solutions in order to make them machine processable. Driven by the invention and ambitious advancement of computer architectures, this gives rise to the emergence of the branch of *computational engineering*. The basic idea is to no longer try to solve PDEs directly, but instead convert them to algebraic (systems of) equations that can be solved by means of a computer and whose solution converges to the differential equation's solution in some sense.

The simulation method of choice in this thesis is the Finite Integration Technique (FIT) [Wei77]. It is introduced by Thomas Weiland in 1977. Compared to other popular methods, like for example Finite Elements, its most notable feature is the fact that it does not originate from a problem-specific derived formulation (e.g. the wave equation). Instead, it provides a matrix-vector formulation of Maxwell's equations themselves that contains only a finite number of spatial state variables. This discrete set of equations is called Maxwell's grid equations. They share a significant amount of properties with their space-continuous counterpart, which makes the Finite Integration Technique a comprehensible and straightforward method. Moreover, it can be considered as a generalization of existing simulation techniques (e.g. FDTD¹).

The following introduction to the Finite Integration Technique is supposed to give a basic understanding and only becomes more elaborate if the respective subject is particularly important in the course of this thesis. For more comprehensive literature on this topic the reader is referred to [Wei96; CW01; SW01].

2.2.1. Maxwell's Grid Equations

Like the majority of simulation techniques, the FIT relies on a computational mesh whose elements (nodes, edges, facets, volumes) are assigned a certain physical quantity. In its original formulation, the mesh edges are assumed to be aligned with a Cartesian coordinate system, although the extension to other curvilinear (but still orthogonal) coordinate systems follows straightforwardly. More effort has to be put into extending the method to triangular [RW85], tetrahedral [Büs11] or, more general, nonorthogonal [Sch99] meshes. Because both Cartesian, as well as cylindrical meshes are used in the course of this thesis, the deduction of Maxwell's grid equations is preliminarily carried out in general (u, v, w) coordinates with metric coefficients h_u , h_v and h_w . We address each node by a triplet of integer index values (ξ, η, ζ) and also assign this index triplet to the node's adjacent cell

¹Finite Difference Time Domain [Yee66].

in ascending coordinate direction. The distinctive properties of a particular mesh coordinate system are then accounted for in sections 2.2.4 and 2.2.5, respectively.

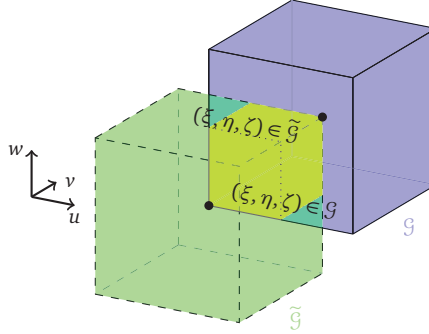


Figure 2.1.: A primary and its corresponding dual cell. Note that primary nodes are centered in dual cells addressed by the same index triplet (ξ, η, ζ) and vice versa.

In addition to an orthogonal mesh \mathcal{G} , a necessary prerequisite for the Finite Integration Technique's deduction is a second, staggered mesh $\tilde{\mathcal{G}}$. This so-called dual mesh is constructed by translating every node (ξ, η, ζ) from the primary mesh \mathcal{G} by $(\frac{h_u \Delta u_\xi}{2}, \frac{h_v \Delta v_\eta}{2}, \frac{h_w \Delta w_\zeta}{2})$ and attaching the corresponding dual cell in descending coordinate direction, as depicted in Fig. 2.1. Δu_ξ , Δv_η and Δw_ζ are the mesh step sizes in terms of the respective coordinate system. The mesh's edge lengths $h_u \Delta u_\xi$, $h_v \Delta v_\eta$ and $h_w \Delta w_\zeta$ need not necessarily be equal for each mesh cell. If they are anyhow, their index is omitted. By design, all primary edges intersect dual facets orthogonally and vice versa.

For the purpose of a formulation that is well suited for treatment with methods from linear algebra, the index triplet (ξ, η, ζ) needs to be transformed into a one-dimensional index, called the canonical index k . The first index $k = 1$ is assigned to the mesh node that has the lowest coordinate values u , v and w . On a mesh with N_u nodes along u (and so forth for v and w), k is incremented along u for each v -line and, subsequently, for each w -plane:

$$k = 1 + (\xi - 1)M_u + (\eta - 1)M_v + (\zeta - 1)M_w \quad (2.11)$$

For convenience, the offset constants $M_u = 1$, $M_v = N_u$ and $M_w = N_u N_v$ are defined. They indicate by how much a canonical index k has to be raised if the node's neighboring point in the specified direction is considered.

Edges (L) and facets (A) receive canonical indices as well. On the primary mesh, the index results from the smaller index of the two (for edges) or four (for facets) adjoining nodes. Since there are three times as many edges and facets than nodes, a direction-dependent offset τN_p is added for uniqueness: $\tau = 0$ for u -direction, $\tau = 1$ for v -direction and $\tau = 2$ for w -direction. N_p is the total number of nodes, i.e. $N_p = N_u N_v N_w$.

Furthermore, each dual edge is assigned the same index as the primary facet that it intersects. Correspondingly, each dual facet's index is determined by the intersecting primary edge. This also follows directly from the dual mesh construction scheme, which is visualized in Fig. 2.1.

2.2.1.1. Faraday's Law

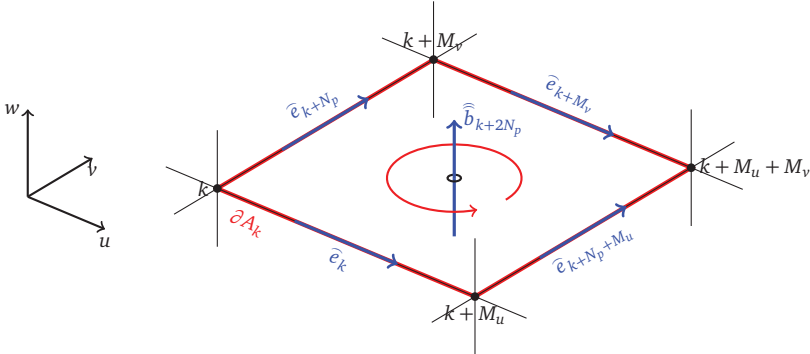


Figure 2.2.: A w -directed primary mesh facet A_k with magnetic grid flux and related electric grid voltages on its edges. All nodes and electromagnetic quantities are indexed according to the canonical indexing scheme.

In order to obtain a matrix-vector formulation of Maxwell's equation (2.1a), a single, w -directed, primary mesh facet A_k is considered exemplarily (see Fig. 2.2). We define the integrations to be carried out over its area or, respectively, its boundary

contour ∂A_k . Then the left hand side's integration path decomposes into four parts:

$$\oint_{\partial A_k} \vec{E} \cdot d\vec{s} = \int_{L_k}^{\vec{e}_k} \vec{E} \cdot d\vec{s} - \int_{L_{k+M_v}}^{\vec{e}_{k+M_v}} \vec{E} \cdot d\vec{s} - \int_{L_{k+N_p}}^{\vec{e}_{k+N_p}} \vec{E} \cdot d\vec{s} + \int_{L_{k+N_p+M_u}}^{\vec{e}_{k+N_p+M_u}} \vec{E} \cdot d\vec{s} = -\frac{d}{dt} \iint_{A_k} \vec{B} \cdot d\vec{A} \quad (2.12)$$

Instead of electromagnetic fields and fluxes, the FIT's state variables are integral quantities. As introduced in (2.12), there are electric grid voltages \vec{e}_k defined as integrals along primary edges, and magnetic grid fluxes \vec{b}_k defined as integrals over primary facets. In a mesh with N_p nodes, there are $3N_p$ state variables of each kind². They are collected in vectors \vec{e} and \vec{b} . We arrange the signs that result from splitting the contour path integral in (2.12) into a $3N_p \times 3N_p$ matrix \mathbf{C} and yield the mesh representation of Faraday's Law:

$$\mathbf{C}\vec{e} = -\frac{d}{dt}\vec{b} \quad (2.13)$$

Its appearance is similar to (2.2a), but, due to the introduction of the computational mesh, it is discrete in a spatial sense. The matrix \mathbf{C} goes by the name *curl matrix* and takes the role of the continuous curl operator. The close relationship becomes even more obvious if it is denoted by its $N_p \times N_p$ submatrices³ \mathbf{P}_u , \mathbf{P}_v and \mathbf{P}_w that can be interpreted as central difference approximations of partial derivatives with respect to u , v or w :

$$\mathbf{C} = \begin{bmatrix} \mathbf{0} & -\mathbf{P}_w & \mathbf{P}_v \\ \mathbf{P}_w & \mathbf{0} & -\mathbf{P}_u \\ -\mathbf{P}_v & \mathbf{P}_u & \mathbf{0} \end{bmatrix} \quad (2.14)$$

The partial derivative matrices' exact definitions depend on the type of mesh system and are given in sections 2.2.4 and 2.2.5 for Cartesian and cylindrical meshes.

2.2.1.2. Ampère's Law

Maxwell's equation (2.1b) is transformed into its grid equation equivalent in exactly the same way demonstrated in (2.12). However, the dual mesh $\tilde{\mathcal{G}}$ is used for reasons explained in Section 2.2.2. Local line integrals over the magnetic field \vec{H} are defined as magnetic grid voltages \vec{h}_k and facet integrals over the electric displacement \vec{D}

²Some of them are virtually nonexistent because they are located outside the computational domain. In order for the canonical indexing scheme to work they are indexed anyway.

³This submatrix notation is only valid if the canonical indexing scheme is obeyed.

are defined as electric grid fluxes $\widehat{\mathbf{d}}_k$. The electric grid current $\widehat{\mathbf{j}}_k$ stands for the facet-based current density \vec{J} . Aggregated to matrices and vectors, this leads to the following formulation:

$$\widetilde{\mathbf{C}}\mathbf{h} = \frac{d}{dt} \widehat{\mathbf{d}} + \widehat{\mathbf{j}} \quad (2.15)$$

Due to the aforementioned way of assigning dual edges \widetilde{L}_k and facets \widetilde{A}_k the same index as their intersecting counterparts on the primary mesh, the dual curl matrix $\widetilde{\mathbf{C}}$ stands in close relationship to the primary one [Wei96]:

$$\widetilde{\mathbf{C}} = \begin{bmatrix} \mathbf{0} & -\widetilde{\mathbf{P}}_w & \widetilde{\mathbf{P}}_v \\ \widetilde{\mathbf{P}}_w & \mathbf{0} & -\widetilde{\mathbf{P}}_u \\ -\widetilde{\mathbf{P}}_v & \widetilde{\mathbf{P}}_u & \mathbf{0} \end{bmatrix} = \begin{bmatrix} \mathbf{0} & \mathbf{P}_w^T & -\mathbf{P}_v^T \\ -\mathbf{P}_w^T & \mathbf{0} & \mathbf{P}_u^T \\ \mathbf{P}_v^T & -\mathbf{P}_u^T & \mathbf{0} \end{bmatrix} = \mathbf{C}^T \quad (2.16)$$

As we will see in Section 2.3.2, this is a very important property of the Finite Integration Technique that essentially needs to be preserved even in nonstandard implementations of the partial derivative operators.

2.2.1.3. Gauss' Laws

The previous laws define the electric (magnetic) grid flux to be assigned to dual (primary) facets. By adding up the six grid fluxes whose corresponding facets constitute the volume of a dual (primary) mesh cell, (2.1c) and (2.1d) are discretized as well:

$$\widetilde{\mathbf{S}}\widehat{\mathbf{d}} = \mathbf{q} \quad (2.17a)$$

$$\mathbf{S}\widehat{\mathbf{b}} = \mathbf{0} \quad (2.17b)$$

Again, the close resemblance to Maxwell's equations (2.2c) and (2.2d) can be noticed. The matrices \mathbf{S} and $\widetilde{\mathbf{S}}$ are called primary and dual source matrices and have the dimension $N_p \times 3N_p$. They are assembled as follows:

$$\widetilde{\mathbf{S}} = [\widetilde{\mathbf{P}}_u \quad \widetilde{\mathbf{P}}_v \quad \widetilde{\mathbf{P}}_w] = [-\mathbf{P}_u^T \quad -\mathbf{P}_v^T \quad -\mathbf{P}_w^T] \quad (2.18a)$$

$$\mathbf{S} = [\mathbf{P}_u \quad \mathbf{P}_v \quad \mathbf{P}_w] \quad (2.18b)$$

The vector \mathbf{q} in (2.17a) contains each dual cell's contained charge as a volume integral over the space charge density ρ_q .

In close correspondence to the continuous vector calculus identity $\nabla \cdot \nabla \times \vec{F} = 0$ (with an arbitrary vector field \vec{F}), the relations $\mathbf{S}\mathbf{C} = \mathbf{0}$ and $\widetilde{\mathbf{S}}\widetilde{\mathbf{C}} = \mathbf{0}$ hold for conventional implementations [Wei96].

2.2.2. Discrete Material Relations

Just like there are direct relations between space-continuous flux and field quantities, namely the material parameters ε , μ and σ (cf. (2.3)), grid voltages and fluxes are transformable into each other as well. However, since geometric integrals are involved in the Finite Integration Technique's state variables, the discrete material parameters' appearance is not immediately comparable to the continuous ones'. In particular, the exact material coefficients for a grid voltage/flux-pair k are defined as:

$$M_{\varepsilon,k} = \frac{\widehat{d}_k}{\widehat{e}_k} = \frac{\iint_{\widetilde{A}_k} \vec{D} \cdot d\vec{A}}{\int_{L_k} \vec{E} \cdot d\vec{s}} \quad (2.19a)$$

$$M_{\mu,k} = \frac{\widehat{b}_k}{\widehat{h}_k} = \frac{\iint_{\widetilde{A}_k} \vec{B} \cdot d\vec{A}}{\int_{L_k} \vec{H} \cdot d\vec{s}} \quad (2.19b)$$

$$M_{\sigma,k} = \frac{\widehat{j}_k}{\widehat{e}_k} = \frac{\iint_{\widetilde{A}_k} \vec{J} \cdot d\vec{A}}{\int_{L_k} \vec{E} \cdot d\vec{s}} \quad (2.19c)$$

Obviously, the integrals avoid the quotients of flux densities and fields to be replaced by the space-continuous parameters ε , μ and σ . The necessity of known fields in order to obtain these ideal material coefficients seems to impose narrow confines to the FIT's practical applicability. Without assumptions and approximations none of the above equations simplifies into a practically feasible formulation. However, since this is the only place in the spatial discretization process of Maxwell's equations where approximations are made, a substantial understanding of the introduced error allows to draw conclusions about the method's overall accuracy. This analysis is thoroughly carried out for different kinds of approximations to (2.19) in Chapter 4.

For the time being, we settle for the simplifying assumption that each primary mesh cell is entirely filled with one material, i.e. the material parameters ε , μ and σ are no longer space-continuous but instead constant inside each cell⁴. In that case, the k th material coefficient in (2.19) depends only on the k th facet area, edge length and a weighted average of the involved materials, but no longer on any field information. It is customary to introduce diagonal matrices that constitute the

⁴After imposing this assumption on curved material boundaries they appear to be shaped like staircases, hence the name *staircase approximation* [Hol93].

space-discrete approximations for each voltage/flux pair at once:

$$\mathbf{M}_\varepsilon = \mathbf{D}_{\tilde{A}} \mathbf{D}_\varepsilon \mathbf{D}_L^{-1} \quad (2.20a)$$

$$\mathbf{M}_\mu = \mathbf{D}_A \mathbf{D}_\mu \mathbf{D}_L^{-1} \quad (2.20b)$$

$$\mathbf{M}_\sigma = \mathbf{D}_{\tilde{A}} \mathbf{D}_\sigma \mathbf{D}_L^{-1} \quad (2.20c)$$

For more details on these approximations' deduction and their accuracy, the reader is referred to Section 4.1.

2.2.3. Boundary Conditions

Primary mesh cells define the computational domain's spatial extent. The staggered fashion of the dual mesh leads to incomplete integration paths at the domain's boundaries. More precisely, tangential electric grid components are not uniquely defined without further measures. Therefore, we impose so-called *boundary conditions* that introduce a specified field behavior on the boundaries into Maxwell's grid equations. This concept is very similar to the introduction of Neumann or Dirichlet boundary conditions [Jac98] in order to solve continuous field problems.

A magnetic boundary condition is implemented by appropriately shortened dual edges and facets so that they no longer intersect the computational domain's boundary but fit exactly into it. This constitutes implicitly closed integration paths that comprise vanishing tangential magnetic field components. This behavior equals that of the transition to a perfect magnetic conductor.

If, on the other hand, the questionable tangential electric field components are assumed to be zero directly, their underlying integration path is irrelevant and, therefore, unproblematic. This is achieved by setting the corresponding edge lengths in \mathbf{D}_L to zero. Vanishing tangential electric fields also occur on interfaces to perfect electric conductors, which explains the name electric boundary condition.

2.2.4. Cartesian Mesh

The Cartesian mesh (cf. Fig. 2.3) is the most elementary one, which is why it is employed by far the most often in practice. It is obtained by substituting $(u, v, w) \rightarrow (x, y, z)$. From a mathematical point of view its simplicity stems from the fact that $h_x = h_y = h_z = 1$, i.e. no metric coefficient needs to be considered effectively. Geometrically speaking this means that all edges are straight lines, all facets are rectangles and all cells are cuboids. Furthermore, if all mesh steps Δx_ξ , Δy_η and Δz_ζ are equal, all edges (facets, cells) have the same length (area, volume). The mesh steps' index can be dropped and the mesh is called equidistant.

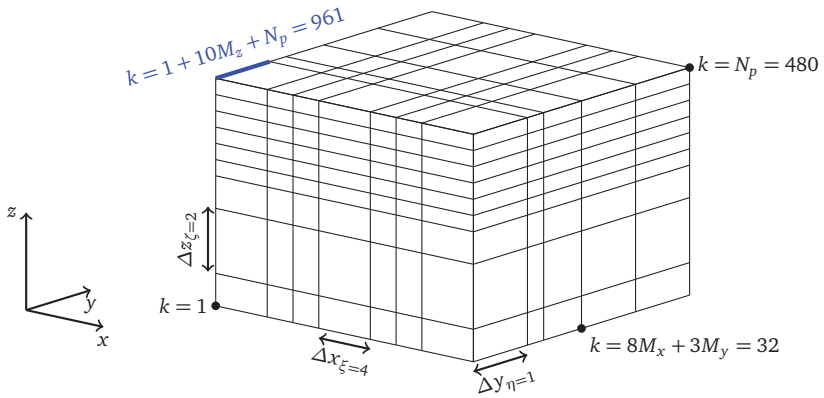


Figure 2.3.: A non-equidistant Cartesian mesh with $N_x = 8$, $N_y = 6$ and $N_z = 10$. Some indices are given for better comprehension of the canonical indexing scheme.

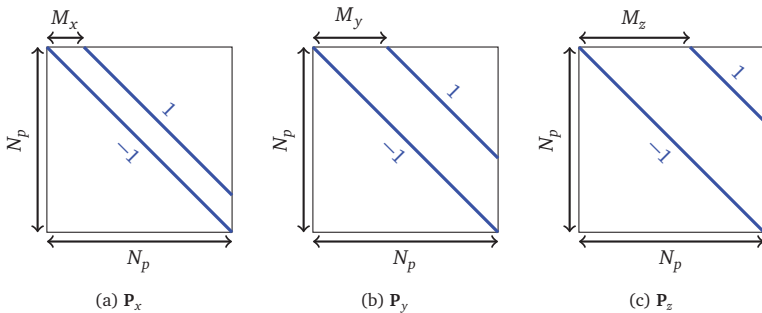


Figure 2.4.: Symbolic representation of the partial derivative matrices for a Cartesian mesh.

Regardless of its size, a Cartesian mesh is always terminated by six planar boundaries. That makes its topology easy to handle because either a node lies on the boundary or it has six directly adjacent nodes whose canonical indices are determined by adding or subtracting M_x , M_y or M_z . As a consequence, this allows for a two-banded structure of the partial derivative matrices \mathbf{P}_x , \mathbf{P}_y and \mathbf{P}_z , as depicted in Fig. 2.4.

2.2.5. Cylindrical Mesh

Literature on electromagnetic field simulation with focus on cylindrical mesh systems is not as common as for Cartesian meshes. Examples include [Mül+82; Wei83; Fus90; Deh93; DW94; Lie+13], on which the following implementation details are based.

A cylindrical mesh is realized by substituting $(u, v, w) \rightarrow (\rho, \varphi, z)$. The metric coefficients are $h_\rho = 1$, $h_\varphi = \rho$ and $h_z = 1$. That implies the mesh is inherently inhomogeneous. Even if $\Delta\varphi_\eta$ is chosen independently of η , the azimuthal step size $\rho\Delta\varphi$ varies with respect to the radius ρ .

Consequently, in contrast to a Cartesian mesh, a cylindrical mesh is not necessarily terminated by six boundaries. Three cases with distinct topological properties have to be distinguished. A special mesh that takes advantage of rotational symmetry can be considered a fourth case.

2.2.5.1. Circular Segment, z -Axis Not Included

A mesh example for this case is depicted in Fig. 2.5. Despite the fact that the cells are no longer cuboidal (but still hexahedral), this case does not differ from the Cartesian case from a topological point of view. Therefore, the operators \mathbf{P}_ρ , \mathbf{P}_φ and \mathbf{P}_z can be directly inferred from Fig. 2.4.

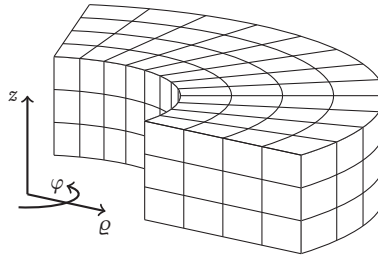
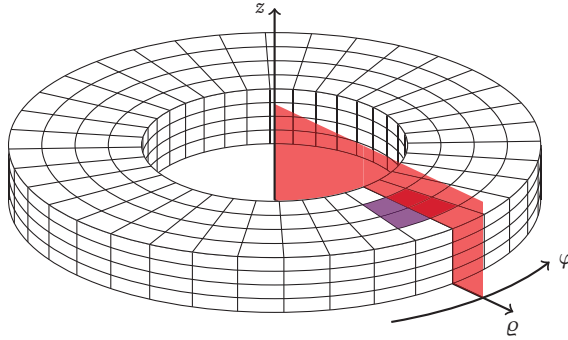


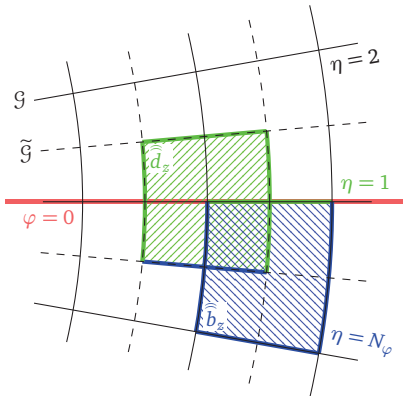
Figure 2.5.: A simple cylindrical mesh.

2.2.5.2. Full Circle, z -Axis Not Included

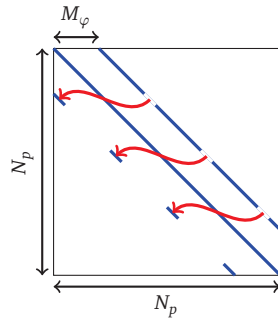
In case the computational domain covers the entire φ -range $[0, 2\pi]$ (cf. 2.6a) some grid components need special treatment. In particular, these are the electric grid



(a) An exemplary cylindrical mesh with $N_\rho = N_z = 5$ and $N_\phi = 35$. The entire azimuthal range is covered by mesh cells.



(b) Detail view of the marked area from Fig. 2.6a. Mesh objects assigned to the first ϕ -plane are highlighted in green, those assigned to the last plane in blue. Note the mutual dependence of quantities from one plane on quantities from the other one.



(c) Schematic visualization of the partial derivative matrix \mathbf{P}_ϕ . The canonical indices' offset across $\phi = 0$ shifts the corresponding matrix entries.

Figure 2.6.: Illustration of an azimuthally closed cylindrical mesh with explanation of its topological properties.

fluxes \widehat{d}_ϱ and \widehat{d}_z in the first φ -plane $\eta = 1$ and, correspondingly, the magnetic grid voltages \widehat{h}_ϱ and \widehat{h}_z in the last φ -plane $\eta = N_\varphi$. Fig. 2.6b shows a highlighted dual facet with its contour path for a \widehat{d}_z -component and a primary facet with its contour path for a \widehat{b}_z -component. Obviously, both contour paths incorporate an edge that initially belongs to the respective other end of the φ -domain.

Clearly, this alters the mesh topology with respect to the previous or the Cartesian case. The planes $\varphi = 0$ and $\varphi = 2\pi$ no longer terminate the computational domain, but instead are mutually coupled. This coupling is accounted for in the partial derivative matrix \mathbf{P}_φ as demonstrated in Fig. 2.6c. Since $\widetilde{\mathbf{P}}_\varphi$ is constructed analogously, the important property of obtaining the dual derivative matrix $\widetilde{\mathbf{P}}_\varphi$ by negative transposition of \mathbf{P}_φ is preserved.

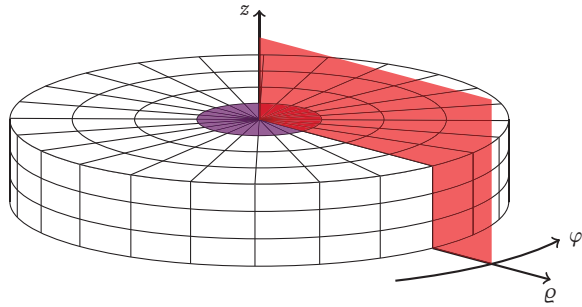
2.2.5.3. z -Axis Included

In a cylindrical mesh, like the one in Fig. 2.7a, the z -axis is characterized by $\varrho = 0$. Since ϱ equals the metric coefficient h_φ , some special properties of mesh objects with $\xi = 1$ arise:

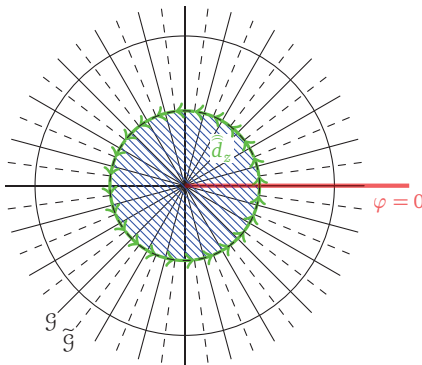
- All primary φ -edges have zero length and are virtually nonexistent. Correspondingly, all azimuthal electric grid voltages \widehat{e}_φ and electric grid fluxes \widehat{d}_φ vanish.
- All primary ϱ -facets have zero area and are virtually nonexistent. Correspondingly, all radial magnetic grid fluxes \widehat{b}_ϱ and magnetic grid voltages \widehat{h}_ϱ vanish.
- For each z -plane all primary z -edges and, correspondingly, all electric grid voltages \widehat{e}_z are located at the same position⁵. Therefore, only one of these edges is maintained per z -plane. All others' lengths are set to zero. For electric grid fluxes \widehat{d}_z this means that they are associated to circular dual facets with the radius of the first dual mesh node (cf. Fig. 2.7b).

While the first two points are implemented straightforwardly by zeroing out the respective entries in the geometry matrices (\mathbf{D}_L , $\mathbf{D}_{\bar{L}}$, \mathbf{D}_A and $\mathbf{D}_{\bar{A}}$), we deal with the third point by adapting the radial partial derivative operator \mathbf{P}_ϱ . The aim is to calculate each of the N_φ magnetic grid fluxes \widehat{b}_φ per z -plane for $\xi = 1$ in a way that employs only the single remaining electric grid voltage along the

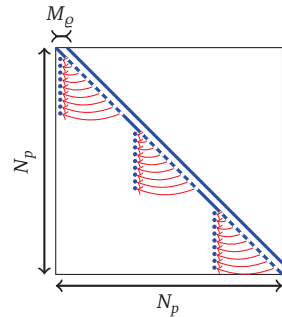
⁵Alternatively, the mesh could be constructed comprising only one z -edge at $\varrho = 0$ per z -plane. This would, however, require sacrificing the simple-bandedness of FIT's operator matrices because the canonical indexing scheme would be no longer applicable.



(a) A cylindrical mesh including the z -axis and being azimuthally closed. Note that in this case only three boundaries of the computational domain exist.



(b) Detail view of the marked area from Fig. 2.7a. The dual z -facet at $\varrho = 0$ is the circle marked in blue. Correspondingly, its boundary contour path is assembled by the φ -directed dual edges (green arrows) adjacent to the z -axis.



(c) The partial derivative matrix \mathbf{P}_ϱ (schematic). The presence of several grid voltages at one location calls for shifting the canonical indices.

Figure 2.7.: Illustration of a cylindrical mesh that includes the z -axis with explanation of its topological properties.

z -axis. Analogously, this also means that the contour path for each \bar{d}_z at $\varrho = 0$ is constituted by the boundary of its related dual facet. As a consequence, the property $\tilde{\mathbf{P}}_\varrho^T = -\mathbf{P}_\varrho$ holds and guarantees the validity of the relation $\tilde{\mathbf{C}}^T = \mathbf{C}$ (cf. Section 2.3.2). A schematic example of an adapted matrix can be found in Fig. 2.7c.

If all field components related to the z -axis are of interest, special measures have to be taken. As described above, vanishing edge lengths and facets also let the associated components' integral state variables equal zero. An approximate means of obtaining them anyhow is described in [DW94].

2.2.5.4. The Body of Revolution Assumption

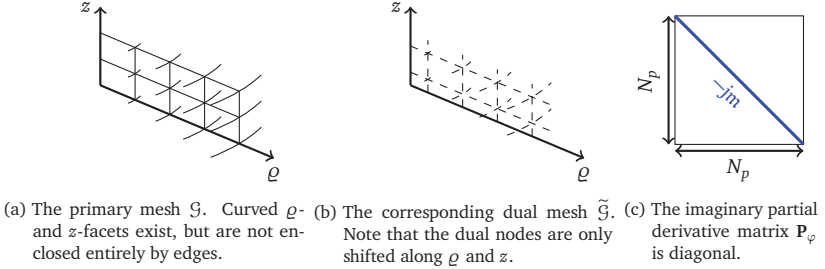
This case is essentially different from the previous cases since it is based on an assumption and, therefore, is not necessarily applicable in all situations. The assumption at hand is the material distribution's independence of φ , thus making the simulated object a rotationally symmetric body of revolution. In that case the fields' φ -dependence becomes separable and is expanded into a complex Fourier series [Wei83; TH05], which is shown exemplary for the electric field \vec{E} , but applies to magnetic fields and all flux densities as well:

$$\vec{E} = \sum_{m=-\infty}^{\infty} \vec{e}_m(\varrho, z) e^{im\varphi} = \Re \sum_{m=0}^{\infty} (2 - \delta_{m,0}) \vec{e}_m(\varrho, z) e^{im\varphi} \quad (2.21)$$

The second identity holds because \vec{E} is real and, hence, its Fourier coefficients obey $\vec{e}_m = \vec{e}_{-m}^*$. We use Kronecker's Delta for taking into account that the azimuthal mode $m = 0$ occurs only once in the spectrum, while all other modes appear twice (as complex conjugates). In this context the Fourier coefficients are called azimuthal modes⁶, which depend only on ϱ and z . Note that the assumption is imposed in the continuous regime of Maxwell's equations.

If the discrete grid equation's deduction is carried out again analogously to Section 2.2.1, but now based on the series expansion (2.21), a very similar set of matrix-vector equations results for each azimuthal mode m . A detailed deduction of the FIT operators' properties explaining the required modifications is carried out in Appendix A. The main difference is that since the azimuthal modes are two-dimensional, a cylindrical ϱ - z -mesh is required (cf. Fig. 2.8a and 2.8b). Moreover, the matrix $\mathbf{P}_\varphi = -jm\mathbf{I}$ becomes imaginary and diagonal, as depicted in Fig. 2.8c. Also, \mathbf{P}_ϱ requires slight adjustments.

⁶Each field and flux density's azimuthal modes, whether space continuous or discrete, are represented by their original symbol in `fraktur` typeface.


 Figure 2.8.: Illustration of a two-dimensional cylindrical mesh in the ρ - z -plane.

For the purpose of visualization or coupling to another cylindrical mesh it is sometimes necessary to construct three-dimensional, canonically indexed grid vectors from a discrete set of azimuthal modes or vice versa. Assuming an azimuthally closed cylindrical mesh with $\Delta\varphi_\eta = \Delta\varphi$ the components are determined by (scaled) Discrete Fourier Transforms (DFT) in two distinct ways:

$$\begin{bmatrix} \bar{\mathbf{e}}_\rho(\xi, \eta, \zeta) \\ \bar{\mathbf{e}}_z(\xi, \eta, \zeta) \\ \bar{\mathbf{h}}_\varphi(\xi, \eta, \zeta) \end{bmatrix} = \Re \sum_{m=0}^{N_\varphi/2} \sqrt{\frac{2 - \delta_{m,0}}{N_\varphi}} \begin{bmatrix} \bar{\mathbf{e}}_{\rho,m}(\xi, \zeta) \\ \bar{\mathbf{e}}_{z,m}(\xi, \zeta) \\ \Delta\varphi \bar{\mathbf{h}}_{\varphi,m}(\xi, \zeta) \end{bmatrix} e^{-jm\varphi_\eta} \quad (2.22a)$$

$$\begin{bmatrix} \bar{\mathbf{e}}_\varphi(\xi, \eta, \zeta) \\ \bar{\mathbf{h}}_\rho(\xi, \eta, \zeta) \\ \bar{\mathbf{h}}_z(\xi, \eta, \zeta) \end{bmatrix} = \Re \sum_{m=0}^{N_\varphi/2} \sqrt{\frac{2 - \delta_{m,0}}{N_\varphi}} \begin{bmatrix} \Delta\varphi \bar{\mathbf{e}}_{\varphi,m}(\xi, \zeta) \\ \bar{\mathbf{h}}_{\rho,m}(\xi, \zeta) \\ \bar{\mathbf{h}}_{z,m}(\xi, \zeta) \end{bmatrix} e^{-jm\tilde{\varphi}_\eta} \quad (2.22b)$$

The components in (2.22a) are those located at full azimuthal mesh steps $\varphi_\eta = (\eta - 1)\Delta\varphi$ and those in (2.22b) at half steps $\tilde{\varphi}_\eta = (\eta - 1/2)\Delta\varphi$, which is why they need to be treated differently. We multiply the φ -components by $\Delta\varphi$ because the φ -integration in the multi-modal field representation is carried out over a normalized integration path length (cf. Appendix A).

The exponential functions and the square root terms are arranged in $N_p \times N_\rho N_z$ -matrices \mathfrak{M}_m (or $\tilde{\mathfrak{M}}_m$ for quantities at $\tilde{\varphi}_\eta$). The transformations can then be carried out conveniently with canonically indexed grid quantities arranged in vectors:

$$\begin{bmatrix} \bar{\mathbf{e}}_\rho \\ \bar{\mathbf{e}}_\varphi \\ \bar{\mathbf{e}}_z \end{bmatrix} = \Re \sum_{m=0}^{N_\varphi/2} \begin{bmatrix} \mathfrak{M}_m \bar{\mathbf{e}}_{\rho,m} \\ \Delta\varphi \tilde{\mathfrak{M}}_m \bar{\mathbf{e}}_{\varphi,m} \\ \mathfrak{M}_m \bar{\mathbf{e}}_{z,m} \end{bmatrix}, \quad \begin{bmatrix} \bar{\mathbf{h}}_\rho \\ \bar{\mathbf{h}}_\varphi \\ \bar{\mathbf{h}}_z \end{bmatrix} = \Re \sum_{m=0}^{N_\varphi/2} \begin{bmatrix} \tilde{\mathfrak{M}}_m \bar{\mathbf{h}}_{\rho,m} \\ \Delta\varphi \mathfrak{M}_m \bar{\mathbf{h}}_{\varphi,m} \\ \tilde{\mathfrak{M}}_m \bar{\mathbf{h}}_{z,m} \end{bmatrix} \quad (2.23)$$

Due to the square root term, the inverse transformation has exactly the same appearance, except for a positive sign in the exponential function. Therefore, the transformation of quantities from a three-dimensional mesh into their azimuthal modes is constituted by Hermitian transposition of the same matrices \mathfrak{M}_m :

$$\begin{bmatrix} \widehat{\mathbf{e}}_{\rho,m} \\ \widehat{\mathbf{e}}_{\varphi,m} \\ \widehat{\mathbf{e}}_{z,m} \end{bmatrix} = \begin{bmatrix} \mathfrak{M}_m^H \widehat{\mathbf{e}}_{\rho} \\ \frac{1}{\Delta\varphi} \widetilde{\mathfrak{M}}_m^H \widehat{\mathbf{e}}_{\varphi} \\ \mathfrak{M}_m^H \widehat{\mathbf{e}}_z \end{bmatrix}, \quad \begin{bmatrix} \widehat{\mathbf{h}}_{\rho,m} \\ \widehat{\mathbf{h}}_{\varphi,m} \\ \widehat{\mathbf{h}}_{z,m} \end{bmatrix} = \begin{bmatrix} \widetilde{\mathfrak{M}}_m^H \widehat{\mathbf{h}}_{\rho} \\ \frac{1}{\Delta\varphi} \mathfrak{M}_m^H \widehat{\mathbf{h}}_{\varphi} \\ \mathfrak{M}_m^H \widehat{\mathbf{h}}_z \end{bmatrix} \quad (2.24)$$

The fact that the partial derivative matrix \mathbf{P}_{φ} becomes diagonal and regular causes azimuthal electric and magnetic grid voltages explicitly to be dependent on ρ - and z -oriented voltages [Wei83]:

$$\begin{aligned} \widetilde{\mathbf{S}} \widehat{\mathbf{d}}_m &= -\mathbf{P}_{\rho}^T \widehat{\mathbf{d}}_{\rho,m} - jm \widehat{\mathbf{d}}_{\varphi,m} - \mathbf{P}_z^T \widehat{\mathbf{d}}_{z,m} = \mathbf{q} \\ \Leftrightarrow \widehat{\mathbf{e}}_{\varphi,m} &= -\frac{1}{jm} \mathbf{M}_{\varepsilon,\varphi}^{-1} \left(\mathbf{q} + \mathbf{P}_{\rho}^T \widehat{\mathbf{d}}_{\rho,m} + \mathbf{P}_z^T \widehat{\mathbf{d}}_{z,m} \right) \end{aligned} \quad (2.25a)$$

$$\begin{aligned} \mathbf{S} \widehat{\mathbf{b}}_m &= \mathbf{P}_{\rho} \widehat{\mathbf{b}}_{\rho,m} - jm \widehat{\mathbf{b}}_{\varphi,m} + \mathbf{P}_z \widehat{\mathbf{b}}_{z,m} = \mathbf{0} \\ \Leftrightarrow \widehat{\mathbf{h}}_{\varphi,m} &= \frac{1}{jm} \mathbf{M}_{\mu,\varphi}^{-1} \left(\mathbf{P}_{\rho} \widehat{\mathbf{b}}_{\rho,m} + \mathbf{P}_z \widehat{\mathbf{b}}_{z,m} \right) \end{aligned} \quad (2.25b)$$

Thus, the azimuthal modes' φ -components need not be computed, but can be inferred from the other components, which reduces the number of unknowns to $2/3$, or even $1/3$ for $m = 0$.

In practice, the degrees of freedom reduce even further because usually only few modes carry a significant amount of energy or are of interest. We select these modes by suitable criteria and restrict the spectrum to them. This makes the transformations in (2.23) lose their exactness in general. Section 3.2.1.3 defines an azimuthal mode's energy and provides means of detecting those modes which are crucial for accuracy.

2.3. Temporal Discretization

So far Maxwell's equations' spatial dependence is eliminated by the introduction of a set of state variables, each of them defined at a fixed location. Their time dependence, however, remains continuous, which makes Maxwell's grid equations a coupled system of differential equations. In order to solve them algebraically without the assumption of special cases⁷, we introduce a uniformly spaced set

⁷For example the static regime ($\frac{d}{dt} \rightarrow 0$) or time harmonic problems ($\frac{d}{dt} \rightarrow j\omega$).

of discrete points in time. Similar to the spatial mesh, electric and magnetic components are allocated in a staggered fashion on the discrete time axis (cf. Fig. 2.9).

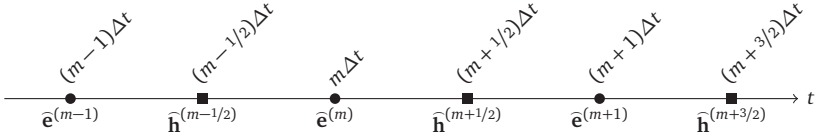


Figure 2.9.: The time axis with staggered allocation of electric and magnetic grid voltages in dependence of the time step $m \in \mathbb{Z}$ and the time step size Δt .

2.3.1. The Leapfrog Algorithm

The starting points of the so-called leapfrog time integration scheme's derivation are Faraday's and Ampère's discrete laws (2.13) and (2.15). The time labels shown in Fig. 2.9 are assigned to the left hand sides' electric and magnetic grid voltage vectors. The right hand sides' time derivatives and the grid current in Ampère's law are assigned time step indices consistently:

$$\mathbf{C}\hat{\mathbf{e}}^{(m)} = -\mathbf{M}_\mu \left\{ \frac{d}{dt} \hat{\mathbf{h}} \right\}^{(m)} \quad (2.26a)$$

$$\mathbf{C}^T \hat{\mathbf{h}}^{(m+1/2)} - \hat{\mathbf{j}}^{(m+1/2)} = \mathbf{M}_\varepsilon \left\{ \frac{d}{dt} \hat{\mathbf{e}} \right\}^{(m+1/2)} \quad (2.26b)$$

We approximate the time derivatives by a central difference quotient, defined as:

$$\left. \frac{df(t)}{dt} \right|_{t=t_0} = \frac{f(t_0 + \Delta t/2) - f(t_0 - \Delta t/2)}{\Delta t} + \mathcal{O}(\Delta t^2) \quad (2.27)$$

This effectively replaces them by two temporally adjacent components and justifies the staggered allocation. We rearrange the equations and yield the leapfrog update scheme:

$$\hat{\mathbf{h}}^{(m+1/2)} = \hat{\mathbf{h}}^{(m-1/2)} - \Delta t \mathbf{M}_\mu^{-1} \mathbf{C} \hat{\mathbf{e}}^{(m)} \quad (2.28a)$$

$$\hat{\mathbf{e}}^{(m+1)} = \hat{\mathbf{e}}^{(m)} + \Delta t \mathbf{M}_\varepsilon^{-1} \left(\mathbf{C}^T \hat{\mathbf{h}}^{(m+1/2)} - \hat{\mathbf{j}}^{(m+1/2)} \right) \quad (2.28b)$$

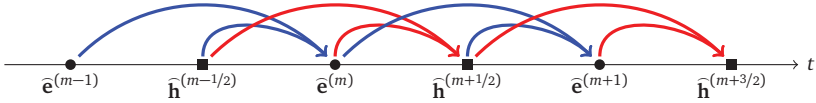


Figure 2.10.: Visualization of \hat{h} -updates (2.28a) in red and \hat{e} -updates (2.28b) in blue.

Its eponymous leapfrog style of temporal updates is visualized in Fig. 2.10. Aside from the use of integral quantities instead of electric and magnetic fields, this algorithm equals the well-known Finite-Difference Time-Domain (FDTD) method [Yee66] from a computational point of view. Since its initial publication in 1966, it has been extensively investigated, modified and compared to other approaches. A good overview of FDTD's properties, extensions and areas of application can be found in [TH05]. Throughout the course of this thesis, the terms *leapfrog update scheme* and *FDTD* are synonymously used.

2.3.2. Convergence

The most important property of a numerical scheme for solving a differential equation is its discrete solution's convergence towards the differential equation's analytical solution in the limit of vanishing mesh step sizes (spatially and temporally). Since this is usually very hard to prove theoretically, the Lax-Richtmyer theorem [LR56] provides alternative means to assure convergence. It states that a finite difference method is convergent if and only if it is consistent and numerically stable. Consistency means that a differential equation's discrete approximation (and not its solution) becomes exact in the limit of vanishing mesh step sizes. This is a much weaker criterion than the solution's convergence. For Maxwell's grid equations it follows directly from Taylor expansions of finite difference approximations. However, an additional criterion, called *numerical stability*, has to be met.

2.3.2.1. Numerical Stability

An iterative algorithm is said to be numerically stable if small perturbations⁸ in its variables do not get amplified from iteration to iteration but instead remain

⁸These include, for instance, round-off or truncation errors, which always occur in practical implementations due to limited precision floating point arithmetic.

bounded in some sense [CN47]. An important prerequisite in order for space- and time-discrete schemes to be numerically stable are some properties that concern only the spatial discretization. They are commonly summarized under the term *spatial stability* and comprise the validity of the matrix relations $\mathbf{S}\mathbf{C} = \mathbf{0}$, $\tilde{\mathbf{S}}\tilde{\mathbf{C}} = \mathbf{0}$ and $\mathbf{C} = \tilde{\mathbf{C}}^T$, as well as the positive definiteness of the material matrices \mathbf{M}_ε , \mathbf{M}_μ and \mathbf{M}_σ [TW98]. These properties can be shown to hold in the scope of the Finite Integration Technique [Wei96]. Therefore, we can turn towards the assessment of numerical stability for the fully discrete leapfrog scheme. Several methods exist for this purpose. The most widely employed one is Von Neumann stability analysis [CN47]. Another technique, the so-called energy method [KCo3; ESWo4], takes a different, more intuitive, approach on finding criteria for numerical stability.

Requirements on parameters of a numerical finite difference scheme in order for it to be numerically stable are called *Courant–Friedrichs–Lewy (CFL)* conditions, named after the authors of an article from 1928 [CFL28]. Although the notion of FDTD does not come up for another 38 years, they already give a criterion for a time step size on equidistant Cartesian meshes that ensures numerical stability:

$$\Delta t \leq \frac{1}{c \sqrt{\frac{1}{\Delta x^2} + \frac{1}{\Delta y^2} + \frac{1}{\Delta z^2}}} \quad (2.29)$$

This condition, amongst others for non-Cartesian meshes, is deducible by means of the energy method as well (cf. Section 3.1).

As demonstrated in Section 3.1 and Appendix B, closed-form CFL criteria only result under consideration of simplifications. Consequently, they can only be taken as an approximation to the largest stable time step size. These approximate limits always lie within the region of numerical stability [THo5], thus leading to a time step size that is smaller than necessary. An alternative, yet more involved and computationally expensive way of calculating the exact limit is the *eigenvalue method* [Doh92]. Due to the CFL criteria's closed-form solution and their obvious dependence on mesh and material parameters, they are preferred over the eigenvalue method in the scope of this thesis.

2.3.3. Newmark-Beta

The algorithm presented in this section is first published in 1959 by Nathan Newmark [New59]. His work deals with time stepping methods in the field of structural dynamics. Since the governing partial differential equation is of elliptic type, the results are straightforwardly transferable to the space discrete electromagnetic

wave equation. The FIT formulation of the electromagnetic wave equation follows directly from (2.13) and (2.15) and reads:

$$\mathbf{M}_\varepsilon \frac{d^2}{dt^2} \bar{\mathbf{e}} + \mathbf{M}_\sigma \frac{d}{dt} \bar{\mathbf{e}} + \mathbf{C}^T \mathbf{M}_\mu^{-1} \mathbf{C} \bar{\mathbf{e}} = -\frac{d}{dt} \hat{\hat{\mathbf{j}}}_s \quad (2.30)$$

Note the close resemblance to its space-continuous counterpart (2.8). Newmark's approach is to replace $\bar{\mathbf{e}}$ and its derivatives by weighted sums of time-discrete values:

$$\left\{ \frac{d^2}{dt^2} \bar{\mathbf{e}} \right\}^{(m)} \rightarrow \frac{\bar{\mathbf{e}}^{(m+1)} - 2\bar{\mathbf{e}}^{(m)} + \bar{\mathbf{e}}^{(m-1)}}{\Delta t^2} \quad (2.31a)$$

$$\left\{ \frac{d}{dt} \bar{\mathbf{e}} \right\}^{(m)} \rightarrow \frac{\gamma \bar{\mathbf{e}}^{(m+1)} + (1-2\gamma) \bar{\mathbf{e}}^{(m)} - (1-\gamma) \bar{\mathbf{e}}^{(m-1)}}{\Delta t} \quad (2.31b)$$

$$\bar{\mathbf{e}}^{(m)} \rightarrow \beta \bar{\mathbf{e}}^{(m+1)} + \left(\frac{1}{2} - 2\beta + \gamma \right) \bar{\mathbf{e}}^{(m)} + \left(\frac{1}{2} + \beta - \gamma \right) \bar{\mathbf{e}}^{(m-1)} \quad (2.31c)$$

The second time derivative's replacement (2.31a) corresponds to a standard central difference approximation. The approximated first time derivative (2.31b) introduces the coefficient γ and also corresponds to a standard central difference approximation if $\gamma = 1/2$. We replace the electric grid voltage $\bar{\mathbf{e}}^{(m)}$ by a weighted sum of itself and its neighbors with weighting factors γ and β . In the special case $\gamma = 1/2$ and $\beta = 0$ the algorithm can be exactly transformed into the leapfrog update scheme (2.28).

The introduced weighting factors have influence on accuracy, numerical stability and energy conservation [KK73]. The choice of $\gamma = 1/2$ guarantees the algorithm to be numerically stable, while at the same time not causing any artificial attenuation [KK73]. Therefore, we opt for this choice throughout this thesis. The coefficient β , on the other hand, changes the restrictiveness of conditions in order to achieve numerical stability. Simultaneously, the resulting quantities' accuracy is altered [GN95].

The dispersion and stability analysis carried out in Appendix B demonstrates that the employable time step size increases monotonically with growing β . Since Newmark's scheme is unconditionally stable for $\beta \geq 1/4$ [New59], the coefficient usually ranges between zero and $1/4$. In that case, the time step size on a Cartesian mesh equates to the following expression, as derived in Appendix B:

$$\Delta t \leq \frac{1}{c \sqrt{1-4\beta} \sqrt{\frac{1}{\Delta x^2} + \frac{1}{\Delta y^2} + \frac{1}{\Delta z^2}}} \quad (2.32)$$

The implications of altering β on the algorithm's accuracy are not predictable with general validity because not only does it depend on the temporal discretization, but also on spatial mesh properties and, of course, the structure to be simulated [THo5]. For a simplified case, results shown in Appendix B indicate that the simulation's error increases the larger β is chosen.

Furthermore, incorporating β causes the update scheme to be more involved. Resulting from (2.30) and (2.31), it is given under neglect of conductivities and currents:

$$(\Delta t^2 \beta \overbrace{\mathbf{M}_e^{-1} \mathbf{C}^T \mathbf{M}_\mu^{-1} \mathbf{C}}^{\mathbf{A}_{cc}} + \mathbf{I}) \bar{\mathbf{e}}^{(m+1)} = \begin{cases} -(\Delta t^2 (1 - 2\beta) \mathbf{A}_{cc} - 2\mathbf{I}) \bar{\mathbf{e}}^{(m)} \\ -(\Delta t^2 \beta \mathbf{A}_{cc} + \mathbf{I}) \bar{\mathbf{e}}^{(m-1)} \end{cases} \quad (2.33)$$

Compared to the leapfrog update scheme (2.28), the Newmark-Beta scheme in its pristine formulation consists of only one equation and only electric grid voltages occur. However, in order to calculate the most recent voltage we need to consider two past values instead of one. It is no longer an explicit scheme because a linear system of equations has to be solved in each update cycle. A visualization of the algorithm is shown in Fig. 2.11.

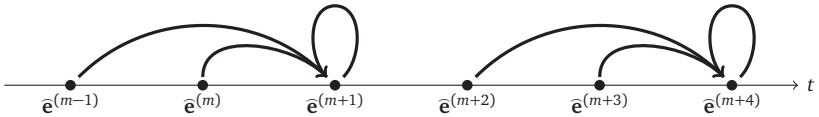


Figure 2.11.: Two (nonconsecutive) implicit Newmark-Beta update steps for the calculation of $\bar{\mathbf{e}}^{(m+1)}$ and $\bar{\mathbf{e}}^{(m+4)}$.

We can rewrite it in terms of a scheme consisting of separate update equations for electric and magnetic grid voltages:

$$\hat{\mathbf{h}}^{(m+1/2)} = \hat{\mathbf{h}}^{(m-1/2)} - \Delta t \mathbf{M}_\mu^{-1} \mathbf{C} (\beta \bar{\mathbf{e}}^{(m+1)} + (1 - 2\beta) \bar{\mathbf{e}}^{(m)} + \beta \bar{\mathbf{e}}^{(m-1)}) \quad (2.34a)$$

$$\bar{\mathbf{e}}^{(m+1)} = \bar{\mathbf{e}}^{(m)} + \Delta t \mathbf{M}_e^{-1} (\mathbf{C}^T \hat{\mathbf{h}}^{(m+1/2)} - \hat{\mathbf{j}}^{(m+1/2)}) \quad (2.34b)$$

Note the close resemblance to the conventional leapfrog scheme (2.28), from which the Newmark-Beta method results by replacing the electric grid voltage inside the $\hat{\mathbf{h}}$ -update by (2.31c).

Time Domain Methods on Cylindrical Meshes

The local material coefficients M_ϵ , M_μ and M_σ transform edge-allocated grid voltages into facet-based grid fluxes. In Section 2.2.2 we briefly introduce the concept of staircase approximations in order to obtain expressions for the material coefficients that are implementable without a priori knowledge about the electromagnetic fields. Chapter 4 assesses possibilities to effectively incorporate field information in order to circumvent staircase approximations. A theoretical investigation of the staircase approximation's drawbacks can also be found there in Section 4.2.1.

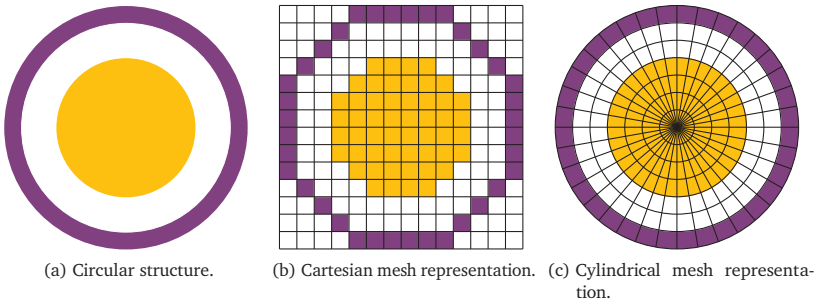


Figure 3.1.: A circularly shaped material distribution and its mapping to computational meshes. Note that the structure effectively changes its shape in its Cartesian mesh representation using the staircase assumption. It remains completely unaltered on the cylindrical mesh.

This chapter, on the other hand, deals with the abandonment of Cartesian meshes in favor of cylindrical mesh systems that meet the prerequisite of entirely filled mesh cells inherently for certain material distributions. As depicted in Fig. 3.1c, a cylindrical mesh conforms with a circularly shaped object's boundaries in a very

favorable way, thus rendering the alteration¹ of the structure in order to fit the Cartesian mesh (cf. Fig. 3.1b) dispensable.

From a practical point of view, cylindrical meshes are more elaborate to implement (cf. Section 2.2.5) than Cartesian meshes. Therefore, if the staircase approximation can not be prevented by either mesh type to a certain extent, the Cartesian mesh is likely to offer a better tradeoff between speed and accuracy. Nevertheless, a broad range of practical examples (cf. Chapter 5) exhibit a material distribution that is well suited for discretization by a cylindrical mesh, which is why its properties and suitability for incorporation in the Finite Integration Technique are investigated in the course of this chapter.

As long as cell shape and characteristic topology are properly accounted for, any numerical simulation method based on the FIT is completely independent of the underlying mesh system from an algorithmic point of view. Publications on these details for cylindrical meshes are available for a long time [Wei83; Fus90; DW94; Deh93]. Their mere implementation is, therefore, manageable straightforwardly. The actual problem with cylindrical meshes and the justification for dedicating them an entire chapter, is their dependence on the nonuniform metric coefficient $h_\varphi = \varrho$. As shown in detail in the following section, the resulting small azimuthal mesh step sizes $\varrho \Delta\varphi$ for ϱ near zero (visible in Fig. 3.1c) impose severe practical restrictions, particularly to FDTD-related time domain simulations. Throughout this chapter we provide methods to address this issue and to compensate the inherent drawbacks of cylindrical meshes.

3.1. Criteria for Numerical Stability

Section 2.3.2.1 introduces the concept of CFL conditions on the time step size of a time integration scheme for ensuring numerical stability. In the following, the energy method [KCo3; ESW04] is employed to derive adapted stability criteria for FDTD-like algorithms on cylindrical meshes. The method is based on the assumption that the discrete electromagnetic energy [SW01],

$$\mathcal{E}^{(m)} = \frac{1}{2} \left(\hat{\mathbf{e}}^{(m)T} \mathbf{M}_\epsilon \hat{\mathbf{e}}^{(m)} + \hat{\mathbf{b}}^{\widehat{(m-1/2)T}} \mathbf{M}_\mu^{-1} \hat{\mathbf{b}}^{\widehat{(m+1/2)}} \right) \quad (3.1)$$

stays constant in the absence of sources and losses:

$$\mathcal{E}^{(m+1)} = \mathcal{E}^{(m)} \quad \forall m \in \mathbb{Z} \quad (3.2)$$

¹The effect of the staircase approximation in Fig. 3.1b is visualized more drastic than it would be in practice. Instead of entirely filled cells the FIT also enables triangular (2D) or pyramidal (3D) fillings [Wei79].

We use the leapfrog scheme's $\widehat{\mathbf{h}}$ -update (2.28a) to express (3.1) in terms of only two instead of three different time instances:

$$\mathcal{E}^{(m)} = \frac{1}{2} \left(\widehat{\mathbf{e}}^{(m)T} \mathbf{M}_\varepsilon \widehat{\mathbf{e}}^{(m)} + \widehat{\mathbf{b}}^{\widehat{(m-1/2)T}} \mathbf{M}_\mu^{-1} \widehat{\mathbf{b}}^{\widehat{(m+1/2)}} \right) \quad (3.3a)$$

$$= \frac{1}{2} \left(\widehat{\mathbf{e}}^{(m)T} \mathbf{M}_\varepsilon \widehat{\mathbf{e}}^{(m)} + \widehat{\mathbf{b}}^{\widehat{(m-1/2)T}} \mathbf{M}_\mu^{-1} \widehat{\mathbf{b}}^{\widehat{(m-1/2)}} - \Delta t \widehat{\mathbf{b}}^{\widehat{(m-1/2)T}} \mathbf{M}_\mu^{-1} \mathbf{C} \widehat{\mathbf{e}}^{(m)} \right) \quad (3.3b)$$

$$= \frac{1}{2} \begin{bmatrix} \widehat{\mathbf{e}}^{(m)} \\ \widehat{\mathbf{b}}^{\widehat{(m-1/2)}} \end{bmatrix}^T \underbrace{\begin{bmatrix} \mathbf{M}_\varepsilon & -\frac{\Delta t}{2} \mathbf{C}^T \mathbf{M}_\mu^{-1} \\ -\frac{\Delta t}{2} \mathbf{M}_\mu^{-1} \mathbf{C} & \mathbf{M}_\mu^{-1} \end{bmatrix}}_{\mathcal{M}} \begin{bmatrix} \widehat{\mathbf{e}}^{(m)} \\ \widehat{\mathbf{b}}^{\widehat{(m-1/2)}} \end{bmatrix} \quad (3.3c)$$

For clear disambiguation in the following, we name and color the contributing terms in (3.3b) as follows: **electric energy**, **magnetic energy** and **mixed energy**. Note that the mixed energy does not emanate from a physically tangible background, but instead accounts for the temporal misalignment between the electric and magnetic energy. The definition (3.1) satisfies (3.2) formally based on the leapfrog method (2.28), which is demonstrated in [ESWo4]. However, it remains to be shown that (3.1) defines a quantity that represents a physically meaningful energy in the context of the given mesh system. Specifically, $\mathcal{E}^{(m)}$ needs to be a non-negative quantity, regardless of $\widehat{\mathbf{e}}^{(m)}$ and $\widehat{\mathbf{b}}^{\widehat{(m-1/2)}}$ [KCo3]. From (3.3c), we can deduce that this is always the case if the symmetric matrix \mathcal{M} is positive-semidefinite. Instead of verifying this for \mathcal{M} directly, which is infeasible in practice due to its large size $6N_p \times 6N_p$, positive-semidefiniteness is assessed for each mesh cell k separately. Therefore, (3.3c) is evaluated in a cell-wise fashion under consideration of the local energy $\mathcal{E}_k^{(m)}$ and the matrix \mathcal{M}_k , which incorporate only those electric grid voltages and magnetic grid fluxes that are assigned to edges and facets enclosing cell k (for instance cf. Fig. 3.2). Only the cell k that imposes the most severe restrictions in order to achieve positive-semidefiniteness locally determines under which circumstances numerical stability is achievable in a global sense [KCo3]. For a Cartesian mesh system, this leads to the well-known CFL criterion (2.29) [KCo3; ESWo4].

In order to enable a cell based examination, the material coefficients in (3.3b) are disassembled into their facets' areas, their edges' lengths and their averaged permittivities and permeabilities according to (2.20a). Only those parts which are contained by the respective cell are taken into account. As an example for one coefficient k of \mathbf{M}_ε , i.e. $\widetilde{A}_k \langle \varepsilon \rangle_{\widetilde{A}_k} L_k^{-1}$, where $\langle \varepsilon \rangle_{\widetilde{A}_k}$ stands for the averaged permittivity across the dual facet, the implications are as follows. Both \widetilde{A}_k and L_k have to be evaluated with respect to the actual cell's geometry, i.e. in cylindrical

coordinates. \tilde{A}_k intersects a total of four cells, so only its respective subarea inside cell k is taken. L_k is not intersected, so it is taken entirely. Instead of $\langle \varepsilon \rangle_{\tilde{A}_k}$, we use the cell k 's permittivity ε . Note that for M_μ 's contribution the dual edge is intersected and the primary facet is taken as a whole.

Due to basically three different cell shapes in cylindrical meshes this procedure is performed separately for each unique cell geometry in the following sections. For the sake of brevity, we omit the time step indices.

3.1.1. Standard 3D Mesh Cell

A cylindrical mesh excluding the z -axis (cf. sections 2.2.5.1 and 2.2.5.2) consists only of hexahedral cells shaped like the one depicted in Fig. 3.2 and contributes the energy given in Fig. 3.2c. Following the procedure outlined in [KC03], this expression is transformed into a matrix notation of the form $\mathcal{E}_k = \mathbf{x}^T \mathcal{M}_k \mathbf{x}$, where \mathcal{M}_k is a symmetric 18×18 -matrix. The vector \mathbf{x} contains only those electric grid voltages and magnetic grid fluxes that belong to the cell k ($\mathbf{x}^T = [\hat{e}_1, \dots, \hat{e}_{12}, \hat{b}_1, \dots, \hat{b}_6]$). Its coefficients are the fraction terms in Fig. 3.2c.

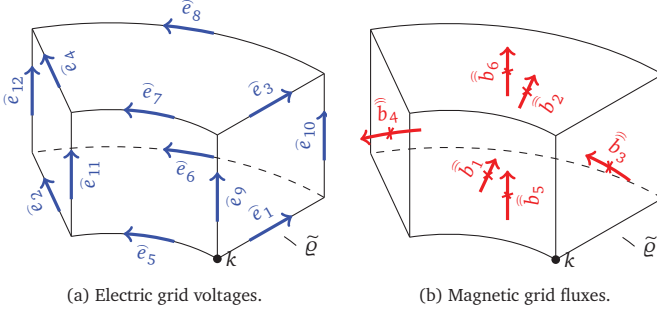
In order to determine under which circumstances \mathcal{M}_k is positive-semidefinite, Sylvester's criterion [HJ12] is evaluated. It states that a Hermitian matrix is positive-semidefinite if and only if all its leading principal minors² are non-negative, i.e. greater or equal to zero. This leads to 18 relations which need to be solved for the time step size Δt . The most restrictive criterion, which in turn satisfies all other relations, is the sought for CFL limit.

Unfortunately, due to a cylindrical cell's irregular shape, these equations are much harder to derive and to solve symbolically than in the Cartesian case. We make use of computer algebra software (e.g. Maxima [Max15] or Mathematica [Wol10]) to carry out the above mentioned tasks and, ultimately, yield the desired stability criterion:

$$\Delta t \leq \frac{1}{c \sqrt{\frac{1}{\Delta \varrho^2} + \frac{1}{\tilde{\varrho}_{\min}^2 \Delta \varphi^2} + \frac{1}{\Delta z^2}}} \quad (3.4)$$

It is very similar to the Cartesian CFL condition (2.29) in its appearance. If $\Delta \varrho$, $\Delta \varphi$ and Δz or the speed of light c are not equal for each cell, that cell's values leading to the smallest time step size have to be considered. Correspondingly, $\tilde{\varrho}_{\min}$ is the dual radius at the innermost cell's center, as depicted in Fig. 3.2.

²A *minor* is the determinant of an $N \times N$ matrix's submatrix that results from removing several rows and columns. It is called *principal minor* if the removed rows have the same index as the removed columns. Finally, it is called *leading principal minor* if the removed rows and columns are furthermore adjacent and contain the N th row and column.



$$\mathcal{E}_k = \left\{ \begin{array}{l}
 \frac{\varepsilon \Delta z \tilde{\rho} \Delta \varphi}{8 \Delta \rho} (\bar{e}_1^2 + \bar{e}_2^2 + \bar{e}_3^2 + \bar{e}_4^2) + \frac{\varepsilon \Delta \rho \Delta z}{8 (\tilde{\rho} - \frac{1}{2} \Delta \rho) \Delta \varphi} (\bar{e}_5^2 + \bar{e}_7^2) \\
 + \frac{\varepsilon \Delta \rho \Delta z}{8 (\tilde{\rho} + \frac{1}{2} \Delta \rho) \Delta \varphi} (\bar{e}_6^2 + \bar{e}_8^2) + \frac{\varepsilon \Delta \varphi (\tilde{\rho} \Delta \rho - \frac{1}{2} \Delta \rho^2)}{8 \Delta z} (\bar{e}_9^2 + \bar{e}_{11}^2) \\
 + \frac{\varepsilon \Delta \varphi (\tilde{\rho} \Delta \rho + \frac{1}{2} \Delta \rho^2)}{8 \Delta z} (\bar{e}_{10}^2 + \bar{e}_{12}^2) + \frac{\Delta \rho}{4 \mu (\tilde{\rho} - \frac{1}{2} \Delta \rho) \Delta \varphi \Delta z} \bar{b}_1^2 \\
 + \frac{\Delta \rho}{4 \mu (\tilde{\rho} + \frac{1}{2} \Delta \rho) \Delta \varphi \Delta z} \bar{b}_2^2 + \frac{\tilde{\rho} \Delta \varphi}{4 \mu \Delta \rho \Delta z} (\bar{b}_3^2 + \bar{b}_4^2) + \frac{\Delta z}{4 \mu \Delta \varphi \tilde{\rho} \Delta \rho} (\bar{b}_5^2 + \bar{b}_6^2) \\
 - \frac{\Delta t \Delta \rho}{4 \mu (\tilde{\rho} - \frac{1}{2} \Delta \rho) \Delta \varphi \Delta z} \bar{b}_1 (\bar{e}_5 - \bar{e}_7 - \bar{e}_9 + \bar{e}_{11}) \\
 - \frac{\Delta t \Delta \rho}{4 \mu (\tilde{\rho} + \frac{1}{2} \Delta \rho) \Delta \varphi \Delta z} \bar{b}_2 (\bar{e}_6 - \bar{e}_8 - \bar{e}_{10} + \bar{e}_{12}) \\
 - \frac{\Delta t \tilde{\rho} \Delta \varphi}{4 \mu \Delta \rho \Delta z} [\bar{b}_3 (-\bar{e}_1 + \bar{e}_3 + \bar{e}_9 - \bar{e}_{10}) + \bar{b}_4 (-\bar{e}_2 + \bar{e}_4 + \bar{e}_{11} - \bar{e}_{12})] \\
 - \frac{\Delta t \Delta z}{4 \mu \Delta \varphi \tilde{\rho} \Delta \rho} [\bar{b}_5 (\bar{e}_1 - \bar{e}_2 - \bar{e}_5 + \bar{e}_6) + \bar{b}_6 (\bar{e}_3 - \bar{e}_4 - \bar{e}_7 + \bar{e}_8)]
 \end{array} \right.$$

(c) Contribution to total energy.

Figure 3.2.: The k th cell of a cylindrical mesh apart from the z -axis with arbitrary indexing of grid quantities.

A similar criterion is found in the literature [CF94], only instead of the dual radius $\tilde{\varrho}$ the (smaller) primary radius ϱ is used. This has two disadvantages. First, the determined time step size is smaller than it would have to be according to (3.4). Second, the case of a mesh including the z -axis ($\varrho = 0$) is not included as a special case, but instead leads to division by zero. By means of (3.4), however, that special case follows for $\tilde{\varrho}_{\min} = \Delta\varrho/2$:

$$\Delta t \leq \frac{1}{c \sqrt{\frac{1}{\Delta\varrho^2} + \frac{4}{\Delta\varrho^2 \Delta\varphi^2} + \frac{1}{\Delta z^2}}} \quad (3.5)$$

It is also directly deducible by means of the energy method using a cell geometry and cell-wise energy definition as shown in Fig. 3.3. Furthermore, it is given in [Dib+99] in the same way.

3.1.2. Body of Revolution Mesh Cell

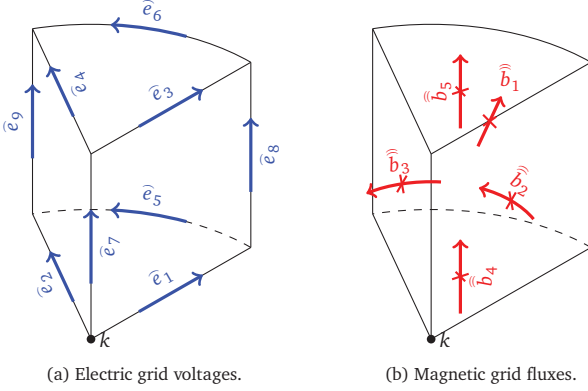
A CFL criterion for quasi-2D modal cylindrical meshes that rely on the body of revolution assumption (cf. Section 2.2.5.4) is given in [Deh93; CW07]:

$$\Delta t \leq \frac{1}{c \sqrt{\frac{1}{\Delta\varrho^2} + \frac{m_{\max}^2}{\Delta\varrho^2} + \frac{1}{\Delta z^2}}} \quad (3.6)$$

As expected, it depends on the highest azimuthal mode order m_{\max} instead of the azimuthal step size $\Delta\varphi$. The formula's lack of radial dependence indicates that it is intended for a mesh including the z -axis, similar to (3.5) in the 3D case. Body of revolution meshes leaving out a certain domain around the z -axis are useful for instance for discretizing coaxial cables. In order to obtain a more general CFL criterion for that case, the energy method is employed once more. The cell geometry is schematically visualized in Fig. 3.4a and 3.4b. Note that even though the mesh is two-dimensional, ϱ - and z -directed facets have finite area, implemented by $\Delta\varphi = 1$. The energy per cell and azimuthal mode m is then accounted for by the formula given in Fig. 3.4c. We use computer algebra software for assessing the positive-semidefiniteness of the resulting matrix $\mathcal{M}_{k,m}$ by means of Sylvester's criterion and obtain the following CFL criterion:

$$\Delta t \leq \frac{1}{c \sqrt{\frac{1}{\Delta\varrho^2} + \frac{m_{\max}^2}{4\tilde{\varrho}_{\min}^2} + \frac{1}{\Delta z^2}}} \quad (3.7)$$

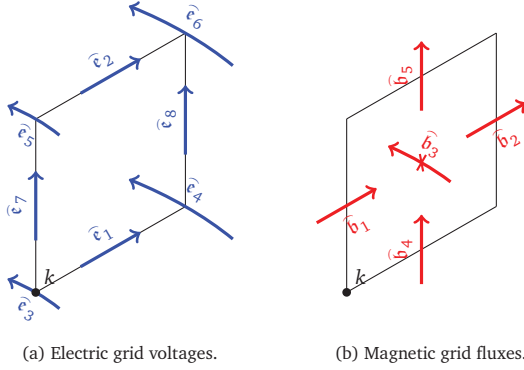
Again, the special case of $\tilde{\varrho}_{\min} = \Delta\varrho/2$ leads directly to (3.6). This generalized formula is not to be found published elsewhere to the best of the author's knowledge.



$$\mathcal{E}_k = \left\{ \begin{array}{l} \frac{\varepsilon \Delta z \Delta \varphi}{16} (\widehat{e}_1^2 + \widehat{e}_2^2 + \widehat{e}_3^2 + \widehat{e}_4^2) + \frac{\varepsilon \Delta z}{8 \Delta \varphi} (\widehat{e}_5^2 + \widehat{e}_6^2) \\ + \frac{\varepsilon \Delta \varphi \Delta \rho^2}{8 \Delta z} (\widehat{e}_7^2 + \widehat{e}_8^2 + \widehat{e}_9^2) + \frac{1}{4 \mu \Delta \varphi \Delta z} \widehat{b}_1^2 + \frac{\Delta \varphi}{8 \mu \Delta z} (\widehat{b}_2^2 + \widehat{b}_3^2) \\ + \frac{\Delta z}{2 \mu \Delta \varphi \Delta \rho^2} (\widehat{b}_4^2 + \widehat{b}_5^2) - \frac{\Delta t}{4 \mu \Delta \varphi \Delta z} \widehat{b}_1 (\widehat{e}_5 - \widehat{e}_6 - \widehat{e}_8 + \widehat{e}_9) \\ - \frac{\Delta t \Delta \varphi}{8 \mu \Delta z} [\widehat{b}_2 (-\widehat{e}_1 + \widehat{e}_3 + \widehat{e}_7 - \widehat{e}_8) + \widehat{b}_3 (-\widehat{e}_2 + \widehat{e}_4 + \widehat{e}_7 - \widehat{e}_9)] \\ - \frac{\Delta t \Delta z}{2 \mu \Delta \varphi \Delta \rho^2} [\widehat{b}_4 (\widehat{e}_1 - \widehat{e}_2 + \widehat{e}_5) + \widehat{b}_5 (\widehat{e}_3 - \widehat{e}_4 + \widehat{e}_6)] \end{array} \right.$$

(c) Contribution to total energy.

Figure 3.3.: The k th cell of a cylindrical mesh adjacent to the z -axis with arbitrary indexing of grid quantities.



$$\mathcal{E}_{k,m} = \left\{ \begin{array}{l}
 \frac{\varepsilon \Delta z \tilde{\rho}}{4 \Delta \rho} (|\tilde{\mathbf{e}}_1|^2 + |\tilde{\mathbf{e}}_2|^2) + \frac{\varepsilon \Delta \rho \Delta z}{8(\tilde{\rho} - \frac{1}{2} \Delta \rho)} (|\tilde{\mathbf{e}}_3|^2 + |\tilde{\mathbf{e}}_5|^2) \\
 + \frac{\varepsilon \Delta \rho \Delta z}{8(\tilde{\rho} + \frac{1}{2} \Delta \rho)} (|\tilde{\mathbf{e}}_4|^2 + |\tilde{\mathbf{e}}_6|^2) + \frac{\varepsilon (\tilde{\rho} \Delta \rho - \frac{1}{2} \Delta \rho^2) \Delta \rho}{4 \Delta z} |\tilde{\mathbf{e}}_7|^2 \\
 + \frac{\varepsilon (\tilde{\rho} \Delta \rho + \frac{1}{2} \Delta \rho^2)}{4 \Delta z} |\tilde{\mathbf{e}}_8|^2 + \frac{\Delta \rho}{4 \mu (\tilde{\rho} - \frac{1}{2} \Delta \rho) \Delta z} |\tilde{\mathbf{b}}_1|^2 \\
 + \frac{\Delta \rho}{4 \mu (\tilde{\rho} + \frac{1}{2} \Delta \rho) \Delta z} |\tilde{\mathbf{b}}_2|^2 + \frac{\tilde{\rho}}{2 \mu \Delta \rho \Delta z} |\tilde{\mathbf{b}}_3|^2 + \frac{\Delta z}{4 \mu \tilde{\rho} \Delta \rho} (|\tilde{\mathbf{b}}_4|^2 + |\tilde{\mathbf{b}}_5|^2) \\
 - \frac{\Delta t \Delta \rho}{4 \mu (\tilde{\rho} - \frac{1}{2} \Delta \rho) \Delta z} \tilde{\mathbf{b}}_1' (\tilde{\mathbf{e}}_3 - \tilde{\mathbf{e}}_5 - j m \tilde{\mathbf{e}}_7) \\
 - \frac{\Delta t \Delta \rho}{4 \mu (\tilde{\rho} + \frac{1}{2} \Delta \rho) \Delta z} \tilde{\mathbf{b}}_2' (\tilde{\mathbf{e}}_4 - \tilde{\mathbf{e}}_6 - j m \tilde{\mathbf{e}}_8) - \frac{\Delta t \tilde{\rho}}{2 \mu \Delta \rho \Delta z} \tilde{\mathbf{b}}_3' (-\tilde{\mathbf{e}}_1 + \tilde{\mathbf{e}}_2 + \tilde{\mathbf{e}}_7 - \tilde{\mathbf{e}}_8) \\
 - \frac{\Delta t \Delta z}{4 \mu \tilde{\rho} \Delta \rho} [\tilde{\mathbf{b}}_4' (-\tilde{\mathbf{e}}_3 + \tilde{\mathbf{e}}_4 + j m \tilde{\mathbf{e}}_1) + \tilde{\mathbf{b}}_5' (-\tilde{\mathbf{e}}_5 + \tilde{\mathbf{e}}_6 + j m \tilde{\mathbf{e}}_2)]
 \end{array} \right.$$

(c) Contribution to total energy.

Figure 3.4.: The k th cell of a body of revolution mesh with arbitrary indexing of grid quantities. We omit the mode index m of field quantities for the sake of brevity. The prime stands for complex conjugation.

3.1.3. Practical Implications

If a simulation's frequency range is given, a typical measure for the quality of a mesh (regardless if Cartesian or cylindrical) is the number of mesh lines that lie within the lowest expected wavelength. This measure is often called lines per wavelength, or the spatial sampling rate S_s . If we assume a homogeneous computational domain, a Cartesian mesh generator is able to choose all three mesh step sizes Δx , Δy and Δz similarly large. A cylindrical mesh generator, on the other hand, has to consider the metric factor ρ in the azimuthal mesh step size $\rho \Delta \varphi$, while $\Delta \rho$ and Δz are radially independent. In order to satisfy the wavelength criterion anywhere in the computational domain, an azimuthally oversampled mesh near the z -axis has to be accepted.

Besides the fact that this increases the degrees of freedom involuntarily, it also causes the previously derived CFL conditions to yield much smaller time steps because only the smallest step sizes in each direction are taken into account. Disregarding their more elaborate implementation, this is the main reason why cylindrical meshes are less frequently used than their Cartesian counterparts since a smaller time step size requires higher computational effort due to an increased number of update cycles required to cover a given time interval. This effect also arises in Cartesian meshes when local geometric details along one coordinate direction find consideration.

Furthermore, the above mentioned inherent inhomogeneity of a cylindrical mesh is also disadvantageous in terms of numerical accuracy. In order to quantitatively assess the spatial discretization error, a mesh representation of the continuous dispersion relation in cylindrical coordinates [Jac98] needs to be investigated. Such a discrete dispersion relation is given in [Petoo]. However, due to its explicit dependence on the radius it only permits to draw conclusions for individual cells and not for the entire computational domain, as desired. The discrete dispersion relation for Cartesian meshes, on the other hand, allows for such an analysis because the mesh can be constructed homogeneously. Therefore, the origin of the discussed inaccuracy is reasoned for heuristically by means of the dispersion analysis carried out in Appendix B for equidistant Cartesian meshes.

We can infer from Figure B.1 and (B.8) that a Cartesian FDTD method's error increases the more its time step size deviates from the largest stable step size the CFL criterion permits. More precisely, the ratio of temporal to spatial sampling rate should be as close to one as possible.

Cylindrical meshes, as stated above, are inherently not equidistant. Their CFL criterion is usually limited by the innermost cells (cf. (3.4)). Conversely, this means

all other cells, especially those at the outer perimeter, would permit a larger time step size than the one they are subjected to. The local ratio of temporal to spatial sampling rate is clearly higher than that of cells near the z -axis. If we assume that the outcome of the Cartesian dispersion analysis is qualitatively transferable to cylindrical meshes, it stands to reason that the outermost cells introduce a significant amount of error. This assumption is justifiable because with growing radius ϱ a cylindrical mesh cell's shape more and more equals that of a Cartesian cell. It is, furthermore, verified in Section 3.2.4 by means of a numerical example.

In conjunction with the previously described increase in computational effort, it becomes obvious that cylindrical meshes are not unconditionally suited as the foundation for conventional FDTD methods. In order to address this issue, the following section introduces and discusses means that allow FDTD simulations on cylindrical meshes to drastically increase the employable time step size.

3.2. Compensation of Degraded Time Step Size

According to the previous section's findings, we need to circumvent the short azimuthal edges of a cylindrical mesh to degrade the time step size in order to make time domain simulations on cylindrical meshes practically feasible and reasonably accurate. There are two basic approaches in order to achieve this.

First, the spatial mesh can be altered in a way that keeps all azimuthal edges approximately at the same length, for example by using a subgridding technique (cf. [ZYM91] for general FDTD subgridding and [Lie+13] for its application to cylindrical meshes). An exemplary mesh constructed by means of this technique is depicted in Fig. 3.5. The need for spatial field interpolation at the interfaces between differently coarse domains introduces unwanted numerical reflections that usually deteriorate accuracy [TW96]. Furthermore, numerical stability can become an issue since the necessary interpolations might violate the conditions given in Section 2.3.2 for spatial stability [TW96]. Standard CFL criteria are also no longer valid [TW96].

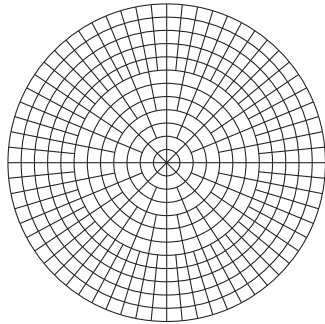


Figure 3.5.: Cylindrical mesh with spatial subgridding.

Second, if the spatial mesh is left unaltered, we can modify the time integration scheme. A technique published in 1990 suggests temporal subgrids [Fus90]. That means the global time step size is chosen according to the coarsest mesh cells. In order to avoid this large time step size to cause instability when being applied to finer mesh cells, these cells are treated in a subcycle consisting of two or more field updates with appropriately diminished time step size. However, due to temporal interpolation at interfaces between regions of different time step sizes, the same disadvantages that occur with spatial subgridding exist here, too.

In the following, two distinct methods to overcome severe time step limitations without subgrids are presented. A third method emerges from combining the two initial ones appropriately. Initially, their increase in computational effectivity and accuracy is theoretically motivated. By means of a common numerical example (cf. Section 3.2.4) all three approaches are compared against each other and shown to comprise specific advantages and disadvantages in terms of applicability, accuracy, speedup, and memory requirements. Simulation results of practically more relevant structures can be found in Chapter 5.

3.2.1. The Coupled Multi-Mode Method

The so-called *Multi-Mode method* is initially introduced in [Deh93; DW94] to improve the accuracy, speed and memory requirements of solving electromagnetic problems on cylindrical meshes in the frequency domain. The system matrix's condition number is typically very large [Deh93; DW94]. A method to overcome the occurrence of a large condition number in the frequency domain also qualifies for time step enhancements in the time domain. The reason is the system matrix's largest eigenvalue, which stands in a direct relationship to its condition number. It behaves inversely proportional to the largest stable time step size for an FDTD simulation [Doh92]. Reducing the condition number is thus equivalent to increasing the time step size. Therefore, a time domain method based on the Multi-Mode approach is introduced in this section.

In terms of numerical stability, the worst case, i.e. the smallest time step size, usually occurs when a cylindrical mesh includes the z -axis (cf. (3.4)). Since this is also the most relevant case from a practical point of view, the method is derived with respect for this special case. Preliminary, we assume a rotationally symmetric structure. The spatial discretization can be carried out either on a fully three-dimensional mesh (Section 2.2.5.3) or on a multi-modal two-dimensional body of revolution mesh (Section 2.2.5.4). Their respective maximum time step sizes Δt_{3D} and Δt_{BOR} are determined by (3.5) and (3.6). We stipulate that the

time step size for the BOR approach shall be larger than that of the 3D method and yield a criterion for the highest azimuthal mode order:

$$\Delta t_{\text{BOR}} > \Delta t_{\text{3D}} \iff m_{\text{max}} < \frac{N_\varphi}{\pi} \quad (3.8)$$

Hence, in order for the body of revolution mesh to impose a weaker stability criterion than the three-dimensional mesh, the highest azimuthal mode order needs to be smaller than the number of nodes in φ -direction divided by π . The smaller it is, the larger the time step gets.

This result has to be interpreted in the context of practical applications. Usually, the field distribution of rotationally symmetric real-world problems is smooth³. Concerning its expansion into azimuthal modes (2.21), high order modes are likely to contribute only insignificantly to the field's 3D representation. Therefore, the maximum mode order m_{max} can often be chosen reasonably small, without introducing substantial error⁴. Influenced by a given spatial sampling rate S_s , the number of φ -nodes N_φ is usually so high that (3.8) is easily fulfilled.

Section 3.2.1.3 provides a technique to automatically detect reasonably negligible azimuthal modes in the course of a time domain simulation.

3.2.1.1. Radial Domain Decomposition

Recall that up to this point the assumption of rotationally symmetric objects has to be valid. This is a very severe restriction because in practice only few objects are bodies of revolution or strong simplifications would have to be applied. For that reason, [DW94] proposes splitting the computational domain radially in two parts: the Multi-Mode domain ranging from $\varrho = 0$ up to a certain radius ϱ_{BOR} and the three-dimensional domain from ϱ_{BOR} to ϱ_{max} . This allows for an advantageous compromise between the requirement of rotational symmetry, which now only needs to hold for $\varrho < \varrho_{\text{BOR}}$, and the employable time step size. Even though deviations from the body of revolution assumption are only permissible in the outer domain ($\varrho \geq \varrho_{\text{BOR}}$), the scope of applications is broadly extended with regard to spatial discretization. Fig. 3.6 demonstrates the decomposition of the computational domain and the different mesh types by means of a practical example that is treated more detailed in Section 5.1.1.

³In this context, we refer to a field distribution as *smooth* if it is sampled by the spatial mesh significantly more often than the Nyquist-Shannon sampling theorem [Kot33; Sha49] demands.

⁴As a side-effect, the number of unknowns is reduced compared to a fully three-dimensional mesh. It can be reduced even further by treating the components $\tilde{e}_{\varphi,m}$ and $\tilde{h}_{\varphi,m}$ only implicitly (cf. Section 2.2.5.4).

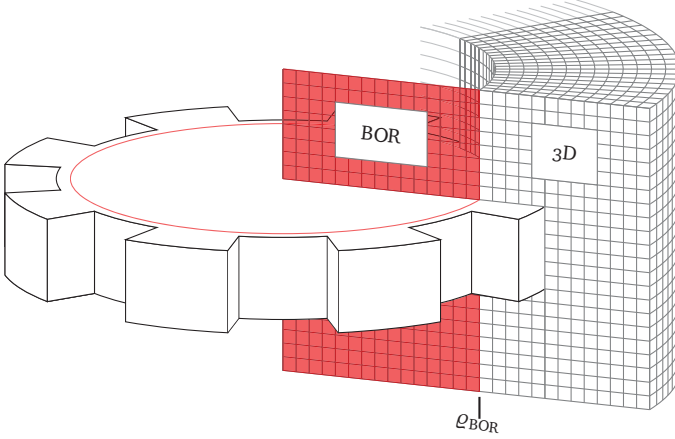


Figure 3.6.: Illustration of radial domain decomposition for Coupled Multi-Mode simulations at the example of a microgear resonator. Detailed information on this structure and its numerical treatment are given in Section 5.1.1.

Section 2.2.5.4 provides means to transform a discrete field representation on a three-dimensional cylindrical mesh into a set of discrete azimuthal modes and vice versa. Those ambiguous field components that lie exactly on the interface $\varrho = \varrho_{BOR}$ are arbitrarily assigned to belong to the Multi-Mode domain. The electric interface components $\widehat{\mathbf{e}}_{\varphi,m}$ and $\widehat{\mathbf{e}}_{z,m}$ serve as auxiliary electric grid voltages \mathbf{e}_{aux} for the three-dimensional domain after transformation. Conversely, the magnetic components at $\widetilde{\varrho}_{BOR}$ ($\widehat{\mathbf{h}}_{\varphi}$ and $\widehat{\mathbf{h}}_z$) act as auxiliary magnetic grid voltages $\widehat{\mathbf{h}}_{aux,m}$ for the quasi two-dimensional region after transformation. $\widetilde{\varrho}_{BOR}$ stands for the dual interface radius, i.e. $\widetilde{\varrho}_{BOR} = \varrho_{BOR} + \Delta\varrho/2$. Fig. 3.7 visualizes the assignment and required field exchange. We implement the chosen assignment by an electric boundary condition in the three-dimensional domain at $\varrho = \varrho_{BOR}$. No boundary condition is imposed to the body of revolution mesh⁵.

In case the simulated object offers rotational symmetry across its entire radial extent, the domain interface can be set to $\varrho_{BOR} = \varrho_{max}$ and a conventional BOR method without domain coupling results. Analogously, we obtain a purely three-dimensional method for $\varrho_{BOR} = 0$.

⁵Dual edges and facets are not shortened but instead virtually reach into the 3D domain.

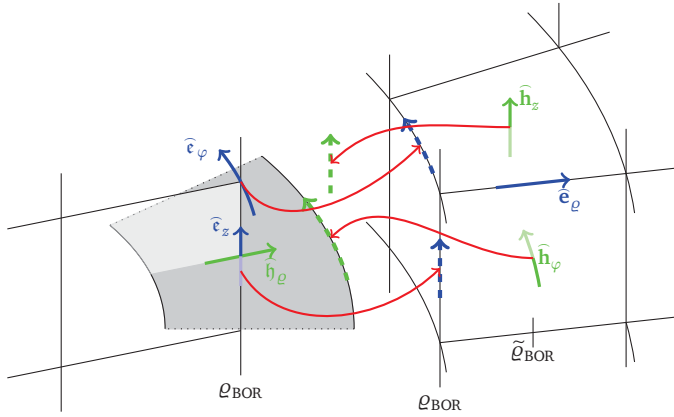


Figure 3.7.: The (expanded) interface between the Multi-Mode domain and the 3D region with highlighted field assignment. The red arrows represent the transfer of electric and magnetic grid voltages from one mesh to the other in order to obtain auxiliary quantities (dashed arrows) for coupling.

3.2.1.2. Coupled Update Scheme

Time domain simulations of the entire computational domain decompose into separate time stepping schemes for each subdomain that are mutually coupled by auxiliary grid voltages at the domain interface. A possible implementation is given in Algorithm 1.

The fact that the Multi-Mode transformation matrix' inverse results by Hermitian transposition (cf. (2.23) and (2.24)) preserves the required duality properties for spatial stability (cf. Section 2.3.2). Since each domain implies its own CFL condition, the largest common time step size is chosen for both schemes:

$$\Delta t \leq \min(\max(\Delta t_{\text{BOR}}), \max(\Delta t_{\text{3D}})) \quad (3.9)$$

Note that the 3D-region is now located at the outer perimeter starting at $\rho = \rho_{\text{BOR}}$, which weakens its implication on the time step size to:

$$\Delta t_{\text{3D}} \leq \frac{1}{c \sqrt{\frac{1}{\Delta \rho^2} + \frac{1}{\rho_{\text{BOR}}^2 \Delta \varphi^2} + \frac{1}{\Delta z^2}}} \quad (3.10)$$

Given fixed spatial mesh step sizes $\Delta \rho$, $\Delta \varphi$ and Δz , the objective of maximizing the time step size Δt is realized by choosing ρ_{BOR} as large as possible in (3.10),

Algorithm 1 Field update cycle for coupled BOR/3D simulations.

 Calculate $\widehat{\mathbf{e}}_{\text{aux}}^{(m)}$ from $\widehat{\mathbf{e}}_{\text{m}}^{(m)}$ according to (2.23)

$$\widehat{\mathbf{h}}^{(m+1/2)} = \widehat{\mathbf{h}}^{(m-1/2)} - \Delta t \mathbf{M}_{\mu,3\text{D}}^{-1} \mathbf{C}_{3\text{D}} \left(\widehat{\mathbf{e}}^{(m)} + \widehat{\mathbf{e}}_{\text{aux}}^{(m)} \right)$$

$$\widehat{\mathbf{e}}^{(m+1)} = \widehat{\mathbf{e}}^{(m)} + \Delta t \mathbf{M}_{\varepsilon,3\text{D}}^{-1} \left(\mathbf{C}_{3\text{D}}^T \widehat{\mathbf{h}}^{(m+1/2)} - \widehat{\mathbf{j}}^{(m+1/2)} \right)$$

for $m = 0 \rightarrow m_{\text{max}}$ **do**

$$\widehat{\mathbf{h}}_{\text{m}}^{(m+1/2)} = \widehat{\mathbf{h}}_{\text{m}}^{(m-1/2)} - \Delta t \mathbf{M}_{\mu,\text{BOR}}^{-1} \mathbf{C}_{\text{BOR},\text{m}} \widehat{\mathbf{e}}_{\text{m}}^{(m)}$$

 Calculate $\widehat{\mathbf{h}}_{\text{aux},\text{m}}^{(m+1/2)}$ from $\widehat{\mathbf{h}}_{\text{m}}^{(m+1/2)}$ according to (2.24)

$$\widehat{\mathbf{e}}_{\text{m}}^{(m+1)} = \widehat{\mathbf{e}}_{\text{m}}^{(m)} + \Delta t \mathbf{M}_{\varepsilon,\text{BOR}}^{-1} \left(\mathbf{C}_{\text{BOR},\text{m}}^H \left(\widehat{\mathbf{h}}_{\text{m}}^{(m+1/2)} + \widehat{\mathbf{h}}_{\text{aux},\text{m}}^{(m+1/2)} \right) - \widehat{\mathbf{j}}_{\text{m}}^{(m+1/2)} \right)$$

end for

while at the same time selecting the highest azimuthal mode order m as low as justifiable in (3.6). However, if one of these optimization parameters reaches a practical limit, further tuning the other parameter does not increase the global time step size. For example if ϱ_{BOR} has reached its upper limit, the choice of a mode order m smaller than $\frac{\Delta\varrho}{\varrho_{\text{BOR}}\Delta\varphi}$ has no influence on numerical stability, which follows directly from (3.8) and (3.9). Nevertheless, we may want to let one domain's CFL limit exceed that of the respective other one to reduce the total degrees of freedom and the computational effort.

3.2.1.3. Automated Mode Selection

As pointed out in (3.8), the Multi-Mode method can only improve the time step size if not every single mode up to the theoretical limit $m_{\text{max}} = N_{\varphi}/2$ (cf. Section 2.2.5.4) is required to obtain accurate results. Unfortunately, the a priori estimation of the highest necessary azimuthal mode order requires extensive knowledge of the simulated object and experience. In order to accomplish this task without user interaction, an automated approach is described in the following.

For that purpose, a modal energy definition, similar to the one introduced in (3.1) and Fig. 3.4c, is introduced:

$$\mathcal{E}_{\text{m}}^{(m)} = \frac{1}{2} \left(\widehat{\mathbf{e}}_{\text{m}}^{(m)H} \widehat{\mathbf{d}}_{\text{m}}^{(m)} + \widehat{\mathbf{h}}_{\text{m}}^{(m+1/2)H} \widehat{\mathbf{b}}_{\text{m}}^{(m+1/2)} \right) \quad (3.11)$$

Note that opposed to the typical staggered allocation according to (3.1), both magnetic values are situated at time step $(m + 1/2)$ by this definition. Besides being derived only on a per cell basis, the formula given in Fig. 3.4c leads to the conclusion that the staggered allocation would otherwise cause the energy to be complex, which would complicate further considerations⁶. The total approximate energy in the rotationally symmetric domain is:

$$\mathcal{E}_{\text{BOR}}^{(m)} = \sum_{m=0}^{m_{\text{max}}} \mathcal{E}_m^{(m)} \quad (3.12)$$

Since every confined object has a discrete set of resonance frequencies, it is reasonable to assume that after a certain period of time the field pattern is dominated by a superposition of resonant modes. In practical applications that are well suited for simulation on a cylindrical mesh, these so-called eigenmodes usually decompose into a small set of low order azimuthal modes without significant loss of accuracy. By that reasoning, the energy of some azimuthal modes (especially those with high mode order), which has become quantifiable by (3.11), is expected to contribute only insignificantly to an eigenmode's total energy.

The tradeoff for detecting each azimuthal mode's energy is that initially each theoretically existing azimuthal mode has to be taken into consideration, which lets the employable time step size get much smaller than necessary⁷. As soon as the excitation signal's continuous energy spectrum is focused at the structure's eigenfrequencies, those azimuthal modes, which are not essentially contributing to resonant fields in terms of energy can be detected and taken out of the update scheme. Subsequently, we enable the time step size to be increased. For this purpose, a threshold ratio is defined, below which an azimuthal mode's energy contribution to the total energy (3.12) is considered negligible.

3.2.2. The Hybrid Newmark-Beta Method

The previously introduced Coupled Multi-Mode algorithm requires some prerequisites to be met, which limit its general applicability. In this section, a different time domain algorithm that circumvents the time step size on cylindrical meshes from being unfeasibly small is introduced.

⁶Nevertheless, the notion of complex modal energy is permissible, because it is an abstract, auxiliary quantity rather than a physically meaningful energy. The sum of all mode energy terms always yields a real value, which can be shown by inserting (2.24) into (3.11).

⁷As predicted by (3.8), the time step size might become even smaller than it would be for an equivalent three-dimensional mesh.

It is related to the Newmark-Beta time stepping scheme described in detail in Section 2.3.3. Newmark-Beta's main advantage is its numerical stability's manipulability by the parameter β . The higher it is chosen, the lower restrictions on the time step size follow (cf. (2.32)). Ultimately, a value of $\beta = 1/4$ makes the resulting algorithm unconditionally stable. At the same time, the results' deviation from those obtained by conventional FDTD (which results for $\beta = 0$) increases (cf. Appendix B). The obvious approach of using a Newmark-Beta scheme with $\beta = 1/4$ on a cylindrical mesh is possible in principle and indeed solves the time step size problem. But it would most likely deteriorate accuracy beyond acceptable levels. Additionally, the computational effort per update cycle would be much higher than for a standard leapfrog scheme because of Newmark-Beta's implicitly formulated update equations (2.34).

A very reasonable compromise between employable time step size, simulation error and computational effort can be achieved by using the Newmark-Beta concept only for those mesh elements which are restrictive in terms of numerical stability and to no longer aim for unconditional stability. Instead, the scheme about to be derived is supposed to obey a CFL limit that is comparable to that of Cartesian FDTD under the assumption of a common spatial sampling rate S_s .

3.2.2.1. Derivation by Curl Operator Splitting

We choose the radial and longitudinal spatial mesh step sizes $\Delta\varrho$ and Δz to directly satisfy the lines per wavelength criterion. However, the term that describes the influence of φ -directed dual edge lengths ($\tilde{\varrho}\Delta\varphi$) varies with the radius and can satisfy the criterion only at the outer perimeter without violating it elsewhere. Inspired by a procedure described in [ZWo2], we decompose the curl matrix \mathbf{C} to deal with spatial derivatives separately along specific directions:

$$\mathbf{C} = \begin{bmatrix} \mathbf{0} & -\mathbf{P}_z & \mathbf{P}_\varphi \\ \mathbf{P}_z & \mathbf{0} & -\mathbf{P}_\varrho \\ -\mathbf{P}_\varphi & \mathbf{P}_\varrho & \mathbf{0} \end{bmatrix} = \underbrace{\begin{bmatrix} \mathbf{0} & -\mathbf{P}_z & \mathbf{0} \\ \mathbf{P}_z & \mathbf{0} & -\mathbf{P}_\varrho \\ \mathbf{0} & \mathbf{P}_\varrho & \mathbf{0} \end{bmatrix}}_{\mathbf{C}_{\varrho z}} + \underbrace{\begin{bmatrix} \mathbf{0} & \mathbf{0} & \mathbf{P}_\varphi \\ \mathbf{0} & \mathbf{0} & \mathbf{0} \\ -\mathbf{P}_\varphi & \mathbf{0} & \mathbf{0} \end{bmatrix}}_{\mathbf{C}_\varphi} \quad (3.13)$$

By that measure the Newmark-Beta method can be applied selectively to those components that are actually responsible for the time step degradation, i.e. those subjected to finite differentiation by \mathbf{C}_φ . Starting from the conventional leapfrog

update scheme (2.28), the curl operator splitting is incorporated:

$$\widehat{\mathbf{h}}^{(m+1/2)} = \widehat{\mathbf{h}}^{(m-1/2)} - \Delta t \mathbf{M}_\mu^{-1} \left(\mathbf{C}_{\varrho z} \widehat{\mathbf{e}}^{(m)} + \mathbf{C}_\varphi \widehat{\mathbf{e}}^{(m)} \right) \quad (3.14a)$$

$$\widehat{\mathbf{e}}^{(m+1)} = \widehat{\mathbf{e}}^{(m)} + \Delta t \mathbf{M}_\varepsilon^{-1} \left(\mathbf{C}^T \widehat{\mathbf{h}}^{(m+1/2)} - \widehat{\mathbf{j}}^{(m+1/2)} \right) \quad (3.14b)$$

In close analogy to (2.34), we apply the Newmark-Beta extension (2.31c), but this time only to the electric grid voltage vector that is subjected to \mathbf{C}_φ . The following modified $\widehat{\mathbf{h}}$ -update results from (3.14a):

$$\widehat{\mathbf{h}}^{(m+1/2)} = \widehat{\mathbf{h}}^{(m-1/2)} - \Delta t \mathbf{M}_\mu^{-1} \left(\mathbf{C}_{\varrho z} \widehat{\mathbf{e}}^{(m)} + \mathbf{C}_\varphi \left(\beta \widehat{\mathbf{e}}^{(m+1)} + (1 - 2\beta) \widehat{\mathbf{e}}^{(m)} + \beta \widehat{\mathbf{e}}^{(m-1)} \right) \right) \quad (3.15)$$

In combination with (3.14b) it is henceforth referred to as the *Hybrid Newmark-Beta* scheme. Note the dependence of $\widehat{\mathbf{h}}^{(m+1/2)}$ on the grid voltage vector $\widehat{\mathbf{e}}^{(m+1)}$, which is not yet available by the time it is needed. Therefore, just like conventional Newmark-Beta, the resulting scheme is implicit. Its numerical treatment involves the solution of linear systems of equations and is further described in Section 3.2.2.4.

3.2.2.2. Comparison with Existing Approach

An article published by Chen and Wang [CW11] in 2011 comprises a so-called *Hybrid Implicit-Explicit FDTD* algorithm, which, albeit being derived for Cartesian meshes, facilitates a very similar task. Like the Hybrid Newmark-Beta method, their scheme's purpose is to prevent one spatial mesh direction from taking influence on the CFL limit. In fact, we can formally prove both algorithms' equivalence to a certain extent [KS13d]. Chen and Wang do not make use of Newmark's approach and rely on a component-wise temporal allocation⁸. However, the Hybrid Implicit-Explicit method yields the exact same results, as far as the unusual temporal allocation permits direct comparison.

While the algorithm might not be slower than the one proposed in this thesis, it complicates the application of well-known concepts related to FDTD simulations, like for instance absorbing boundary conditions (cf. Appendix D). Furthermore, knowledge about general properties of Newmark-Beta, like accuracy and numerical stability, is hard to take advantage of. An important modification of the algorithm that arises specifically from its Newmark-Beta background is provided in the following section.

⁸Applied to the problem at hand, the φ -components $\widehat{\mathbf{e}}_\varphi$ and $\widehat{\mathbf{h}}_\varphi$ are allocated at half time steps ($m + 1/2$), while all other components are assigned to full steps (m).

3.2.2.3. Stability Limit and Radially Adjusted β

As described in [CW11] and adapted to the Hybrid Newmark-Beta algorithm, the time step size obeys the following CFL criterion⁹:

$$\Delta t \leq \frac{1}{c \sqrt{\frac{1}{\Delta \varrho^2} + \frac{1-4\beta}{\tilde{\varrho}_{\min}^2 \Delta \varphi^2} + \frac{1}{\Delta z^2}}} \quad (3.16)$$

It is in close correspondence to (2.32). Only the factor $\sqrt{1-4\beta}$ is now selectively applied to the azimuthal term, instead of to the entire square root. The choice of $\beta = 1/4$ would immediately remove the problematic restriction on the employable time step size for cylindrical meshes. But, as reasoned for in Appendix B, this choice is likely to be undesirable in terms of accuracy. As a remedy, it is no longer opted for eliminating the azimuthal term's influence entirely. Instead, we permit it to be as large as the radial term's. According to (3.16), this is achieved by the following choice:

$$\beta = \frac{1}{4} - \frac{\tilde{\varrho}_{\min}^2 \Delta \varphi^2}{4 \Delta \varrho^2} \quad (3.17)$$

In practice, this leads to values that are only very slightly smaller than $1/4$. In the next step, the fact that this still undesirably large choice of β is only required locally by the innermost cells of a cylindrical mesh is accounted for. Therefore, we evaluate the parameter β in dependence of the radial mesh index ξ , i.e. for each radial mesh layer separately:

$$\beta_{\xi} = \frac{1}{4} - \frac{\tilde{\varrho}_{\xi}^2 \Delta \varphi^2}{4 \Delta \varrho^2} \quad (3.18)$$

Since β_{ξ} is no longer valid globally for the entire mesh, it is arranged in a diagonal matrix \mathbf{M}_{β} according to the canonical indexing scheme (2.11). This matrix replaces the scalar value β in (3.15). If the φ -edges at the outer perimeter are chosen to have the same length as the radial mesh step size, i.e. $\varrho_{\max} \Delta \varphi = \Delta \varrho$, β ranges approximately between $1/4$ and 0. Informally speaking, it facilitates a tradeoff between complete neglect of the azimuthal term in the CFL condition (3.16) and full consideration like in conventional FDTD. The numerical example in Section 3.2.4 shows that this method's results are generally more accurate.

The notion of a spatially adjusted β straightforwardly extends to all other Newmark-Beta applications, including Cartesian meshes. It has also been used for a unified mathematical description of coupled FEM-FDTD algorithm in [RBo2], where

⁹For a conversion between β and the parameter used in Chen and Wang's publication, see [KS13d].

the Finite Element part of the computational domain is subject to an unconditionally stable update scheme with $\beta \geq 1/4$ and the FDTD part results for $\beta = 0$. However, using it in an edge-based fashion with larger β for shorter edges has not been reported before to the best of the author's knowledge.

3.2.2.4. Semi-Implicit Update Scheme

Because the curl operator splitting subjects only certain field components to the Newmark-Beta extension, it is advisable to consider (3.15) and (3.14b) decomposed into the three coordinate directions:

$$\widehat{\mathbf{e}}_{\varrho}^{(m+1)} = \widehat{\mathbf{e}}_{\varrho}^{(m)} + \Delta t \mathbf{M}_{\varepsilon, \varrho}^{-1} \left(\mathbf{P}_z^T \widehat{\mathbf{h}}_{\varphi}^{(m+1/2)} - \mathbf{P}_{\varphi}^T \widehat{\mathbf{h}}_z^{(m+1/2)} - \widehat{\mathbf{j}}_{\varrho}^{(m+1/2)} \right) \quad (3.19a)$$

$$\widehat{\mathbf{e}}_{\varphi}^{(m+1)} = \widehat{\mathbf{e}}_{\varphi}^{(m)} + \Delta t \mathbf{M}_{\varepsilon, \varphi}^{-1} \left(\mathbf{P}_{\varrho}^T \widehat{\mathbf{h}}_z^{(m+1/2)} - \mathbf{P}_z^T \widehat{\mathbf{h}}_{\varrho}^{(m+1/2)} - \widehat{\mathbf{j}}_{\varphi}^{(m+1/2)} \right) \quad (3.19b)$$

$$\widehat{\mathbf{e}}_z^{(m+1)} = \widehat{\mathbf{e}}_z^{(m)} + \Delta t \mathbf{M}_{\varepsilon, z}^{-1} \left(\mathbf{P}_{\varphi}^T \widehat{\mathbf{h}}_{\varrho}^{(m+1/2)} - \mathbf{P}_{\varrho}^T \widehat{\mathbf{h}}_{\varphi}^{(m+1/2)} - \widehat{\mathbf{j}}_z^{(m+1/2)} \right) \quad (3.19c)$$

$$\widehat{\mathbf{h}}_{\varrho}^{(m+1/2)} = \widehat{\mathbf{h}}_{\varrho}^{(m-1/2)} - \Delta t \mathbf{M}_{\mu, \varrho}^{-1} \left(\begin{array}{l} \mathbf{P}_{\varphi} \widehat{\mathbf{e}}_z^{(m)} - \mathbf{P}_z \widehat{\mathbf{e}}_{\varphi}^{(m)} \dots \\ + \mathbf{P}_{\varphi} \mathbf{M}_{\beta, z} (\widehat{\mathbf{e}}_z^{(m+1)} - 2\widehat{\mathbf{e}}_z^{(m)} + \widehat{\mathbf{e}}_z^{(m-1)}) \end{array} \right) \quad (3.19d)$$

$$\widehat{\mathbf{h}}_{\varphi}^{(m+1/2)} = \widehat{\mathbf{h}}_{\varphi}^{(m-1/2)} - \Delta t \mathbf{M}_{\mu, \varphi}^{-1} \left(\mathbf{P}_z \widehat{\mathbf{e}}_{\varrho}^{(m)} - \mathbf{P}_{\varrho} \widehat{\mathbf{e}}_z^{(m)} \right) \quad (3.19e)$$

$$\widehat{\mathbf{h}}_z^{(m+1/2)} = \widehat{\mathbf{h}}_z^{(m-1/2)} - \Delta t \mathbf{M}_{\mu, z}^{-1} \left(\begin{array}{l} \mathbf{P}_{\varrho} \widehat{\mathbf{e}}_{\varphi}^{(m)} - \mathbf{P}_{\varphi} \widehat{\mathbf{e}}_{\varrho}^{(m)} \dots \\ - \mathbf{P}_{\varphi} \mathbf{M}_{\beta, \varrho} (\widehat{\mathbf{e}}_{\varrho}^{(m+1)} - 2\widehat{\mathbf{e}}_{\varrho}^{(m)} + \widehat{\mathbf{e}}_{\varrho}^{(m-1)}) \end{array} \right) \quad (3.19f)$$

Only two ((3.19a) and (3.19c)) of six component updates rely on grid voltages that are not computed yet in the respective update cycle. At first glance this also seems to be the case for the update equation (3.19b). However, we can postpone its execution until the updates of $\widehat{\mathbf{h}}_{\varrho}$ and $\widehat{\mathbf{h}}_z$ are completed. The dependence on unavailable components is resolved by inserting (3.19f) into (3.19a) and (3.19d) into (3.19c), which results in updates for $\widehat{\mathbf{e}}_{\varrho}$ and $\widehat{\mathbf{e}}_z$ that involve the solution of

linear systems of equations:

$$\mathbf{A}_\rho \widehat{\mathbf{e}}_\rho^{(m+1)} = \begin{cases} \left(\mathbf{I} - \Delta t^2 \mathbf{M}_{\varepsilon,\rho}^{-1} \mathbf{P}_\varphi^T \mathbf{M}_{\mu,z}^{-1} \mathbf{P}_\varphi (\mathbf{I} - 2\mathbf{M}_{\beta,\rho}) \right) \widehat{\mathbf{e}}_\rho^{(m)} \\ -\Delta t^2 \mathbf{M}_{\varepsilon,\rho}^{-1} \mathbf{P}_\varphi^T \mathbf{M}_{\mu,z}^{-1} \mathbf{P}_\varphi \mathbf{M}_{\beta,\rho} \widehat{\mathbf{e}}_\rho^{(m-1)} + \Delta t^2 \mathbf{M}_{\varepsilon,\rho}^{-1} \mathbf{P}_\varphi^T \mathbf{M}_{\mu,z}^{-1} \mathbf{P}_\rho \widehat{\mathbf{e}}_\varphi^{(m)} \\ + \Delta t \mathbf{M}_{\varepsilon,\rho}^{-1} \mathbf{P}_z^T \widehat{\mathbf{h}}_\varphi^{(m+1/2)} - \Delta t \mathbf{M}_{\varepsilon,\rho}^{-1} \mathbf{P}_\varphi^T \widehat{\mathbf{h}}_z^{(m-1/2)} - \Delta t \mathbf{M}_{\varepsilon,\rho}^{-1} \widehat{\mathbf{j}}_\rho^{(m+1/2)} \end{cases} \quad (3.20a)$$

$$\mathbf{A}_z \widehat{\mathbf{e}}_z^{(m+1)} = \begin{cases} \left(\mathbf{I} - \Delta t^2 \mathbf{M}_{\varepsilon,z}^{-1} \mathbf{P}_\varphi^T \mathbf{M}_{\mu,\rho}^{-1} \mathbf{P}_\varphi (\mathbf{I} - 2\mathbf{M}_{\beta,z}) \right) \widehat{\mathbf{e}}_z^{(m)} \\ -\Delta t^2 \mathbf{M}_{\varepsilon,z}^{-1} \mathbf{P}_\varphi^T \mathbf{M}_{\mu,\rho}^{-1} \mathbf{P}_\varphi \mathbf{M}_{\beta,z} \widehat{\mathbf{e}}_z^{(m-1)} + \Delta t^2 \mathbf{M}_{\varepsilon,z}^{-1} \mathbf{P}_\varphi^T \mathbf{M}_{\mu,\rho}^{-1} \mathbf{P}_z \widehat{\mathbf{e}}_\varphi^{(m)} \\ -\Delta t \mathbf{M}_{\varepsilon,z}^{-1} \mathbf{P}_\rho^T \widehat{\mathbf{h}}_\varphi^{(m+1/2)} + \Delta t \mathbf{M}_{\varepsilon,z}^{-1} \mathbf{P}_\varphi^T \widehat{\mathbf{h}}_\rho^{(m-1/2)} - \Delta t \mathbf{M}_{\varepsilon,z}^{-1} \widehat{\mathbf{j}}_z^{(m+1/2)} \end{cases} \quad (3.20b)$$

The system matrices are:

$$\mathbf{A}_\rho = \mathbf{I} + \Delta t^2 \mathbf{M}_{\varepsilon,\rho}^{-1} \mathbf{P}_\varphi^T \mathbf{M}_{\mu,z}^{-1} \mathbf{P}_\varphi \mathbf{M}_{\beta,\rho} \quad (3.21a)$$

$$\mathbf{A}_z = \mathbf{I} + \Delta t^2 \mathbf{M}_{\varepsilon,z}^{-1} \mathbf{P}_\varphi^T \mathbf{M}_{\mu,\rho}^{-1} \mathbf{P}_\varphi \mathbf{M}_{\beta,z} \quad (3.21b)$$

Opposed to a conventional Newmark-Beta approach where all six field components rely on computationally expensive linear systems of equations, the hybrid approach with only two implicit component updates is generally much more efficient in terms of execution time per update cycle. Whether it is even more efficient than an entirely explicit standard leapfrog scheme depends on several factors. Generally speaking, the following circumstances positively influence the outcome of a comparison in favor for the Hybrid Newmark-Beta method:

- A very dense mesh around the z -axis which would deteriorate a standard FDTD method's time step size but leaves the hybrid algorithm's step size unaffected.
- Simulations that cover long time intervals. They can be realized by significantly less time samples.
- The existence of efficient matrix factorizations that permit the vast amount of linear systems of equations to be solved fast by means of direct methods.

3.2.2.5. Performance Enhancement of Implicit Component Updates

The last point in the previous itemization is specifically addressed and investigated in this section. The ability to speed up the solution of linear systems of equations

for implicit component updates is crucial for the overall algorithm's performance because a the solution of a linear system of equations consumes much more time than an explicit component update.

Direct solvers, like for example those based on Gaussian elimination, usually attempt to factorize the system matrix into a lower and an upper triangular matrix before actually solving them. Such a matrix decomposition is called LU factorization [Dem97]. It is the time and memory consuming part of the solution process. Based on the triangular LU decomposition, the final result is obtained by computationally efficient forward and back substitutions [Dem97].

The $N_p \times N_p$ system matrices \mathbf{A}_ϱ and \mathbf{A}_z (from (3.21)) remain unchanged in each update cycle. This allows us to factorize them before we start the time loop so that only forward and back substitutions have to be performed in order to accomplish the implicit component updates.

However, the LU decomposition of a sparse matrices, like \mathbf{A}_ϱ and \mathbf{A}_z , is not sparse in general. Especially for large numbers of unknowns, this would lead to factorizations that exceed the available computer memory. The systems would become practically unsolvable by direct methods like Gaussian elimination and iterative methods like conjugate gradients or generalized minimal residuals [Dem97] would be preferred. Fortunately, the following closer investigation of Hybrid Newmark-Beta's system matrices reveals that they have very beneficial properties with regard to their LU factorizations.

Their definition 3.21 and the Finite Integration Technique's tendency to create simply-structured, banded operators, allows for investigating the matrices' sparsity pattern¹⁰. Based on a given mesh comprising the full azimuthal range of 2π (\mathbf{P}_φ takes the shape shown in Fig. 2.6c), this pattern is visualized in Fig. 3.8a. It is independent of whether \mathbf{A}_ϱ or \mathbf{A}_z is considered.

Due to the partial derivative operator \mathbf{P}_φ 's banded pattern, we can infer that the system matrix \mathbf{A}_ϱ consists of only five bands. Besides the principal diagonal, there are two bands on the M_φ th upper and lower diagonal and two bands on the $M_\varphi(N_\varphi - 1)$ th upper and lower diagonal. In case the computational domain does not cover a full circle, \mathbf{P}_φ is chosen according to Fig. 2.4b and the outer bands of \mathbf{A}_ϱ vanish.

The lower and upper bandwidth of a matrix directly determines the respective bandwidth of its lower and upper triangular factor [Dem97]. This can be clearly seen in Fig. 3.8b and Fig. 3.8c and has a very fortunate outcome for the factorization's memory requirement, which turns out to be only slightly higher than the original matrix one's. This enables us to compute the LU decompositions before the time

¹⁰A sparsity pattern is a qualitative visualization of the nonzero entries of a matrix.

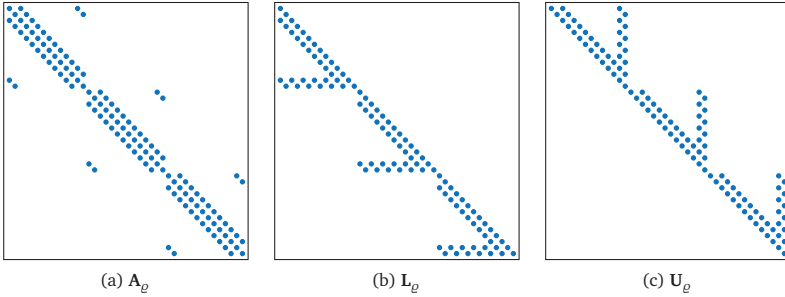


Figure 3.8.: Exemplary sparsity patterns of \mathbf{A}_ℓ and its triangular factors \mathbf{L}_ℓ and \mathbf{U}_ℓ ($\mathbf{A}_\ell = \mathbf{L}_\ell \mathbf{U}_\ell$) evaluated for an azimuthally closed mesh with $N_\ell = 2$, $N_\varphi = 7$ and $N_z = 3$.

loop is started and thereby greatly enhance the algorithm's performance, as will be demonstrated in Section 3.2.4.

3.2.3. Combination of Coupled Multi-Mode with Hybrid Newmark-Beta

After the introduction of the Coupled Multi-Mode approach (Section 3.2.1) and the Hybrid Newmark-Beta method (Section 3.2.2), the question at hand is whether both algorithms can be combined in a way that circumvents each particular method's disadvantages. In fact, this is possible based on the domain decomposition as performed in the context of the Coupled Multi-Mode method. The Hybrid Newmark-Beta approach is then applied only to the rotationally symmetric inner domain with very beneficial outcome.

As reported in [CW08], the combination of BOR FDTD with the hybrid approach enables the otherwise (semi-)implicit scheme to be carried out without the need to solve any linear system of equations. We insert the Multi-Mode method's partial derivative operator \mathbf{P}_φ , which is a diagonal matrix (cf. Fig. 2.8c), into the Hybrid Newmark-Beta method's system matrices (3.21), which makes them diagonal as well and easily and explicitly invertible. The absence of implicit equations promises an increased processing speed of each update cycle. Especially for simulations consisting of large amounts of time samples, a faster overall simulation time can be expected.

Furthermore, the stability limit in the Multi-Mode domain (3.7) loses its dependence on the mode order m because the azimuthal term $\frac{m^2_{\max}}{4\varrho^2_{\min}}$ is eliminated if we subject the φ -derivatives to Newmark's approach. Consequently, the restriction of the simulation to azimuthal modes of low order for the sake of an increased time step size is no longer necessary. Especially the elaborate and possibly error prone automatic mode detection introduced in Section 3.2.1.3 can be circumvented by taking into account each azimuthal mode $0 \leq m \leq N_\varphi/2$. On the other hand, the number of degrees of freedom would remain the same, which is why we still might want to take advantage of the automatic mode detection, particularly if only few significant azimuthal modes are anticipated.

Even though the domain that incorporates the Newmark-Beta time integration scheme is now smaller than in case of the previously described algorithm, it is still advisable to adjust its parameter β 's value dependent on the radius, just like suggested in Section 3.2.2.3.

3.2.4. Validation and Comparison by Numerical Example

In the following, the previously introduced time domain simulation approaches are utilized to determine the resonance frequencies of an ideal pillbox resonator, shown in Fig. 3.9a. This allows for the predictions made in the previous sections to be validated. We compare them mutually and to results obtained by analytical formulas and conventional FDTD simulations. By that approach, each method's particular strengths and weaknesses are pointed out.

There exist very well-approved methods to handle curved interfaces to perfect electric conductor on Cartesian meshes [Rie89; Kri+98; DM98]. However, interfaces between nonconformal materials with finite material parameters are much harder to handle in an accurate fashion (this will be the main topic of the following Chapter 4). Since this simple example does not comprise such interfaces, we postpone the comparison to FDTD on a Cartesian mesh to Chapter 5.

For those algorithms that rely on radial domain decomposition into a rotationally symmetric inner part and an outer part that does not have to be symmetric, the domain interface is introduced at $\varrho = \varrho_{\text{BOR}}^{\text{11}}$. In this case, the coupled mesh configuration can be seen in Fig. 3.9b. For approaches that operate on an entirely three-dimensional mesh, the parameter ϱ_{BOR} is obsolete and the green mesh in Fig. 3.9b is extended to $\varrho = 0$ with otherwise identical parameters.

¹¹This example exhibits rotational symmetry and, therefore, does not necessitate a 3D mesh. For the sake of demonstration, it is introduced nevertheless.

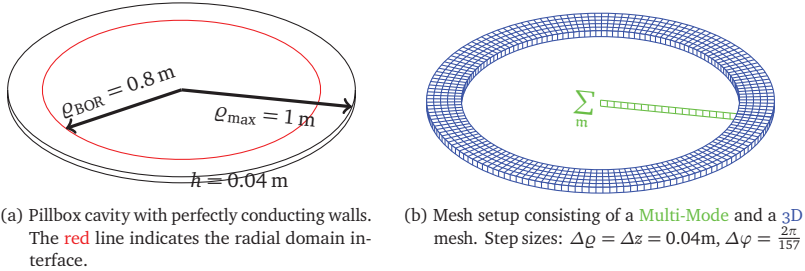


Figure 3.9.: Geometry and computational setup of a pillbox resonator serving as numerical example.

This example's aim is to compute a subset of the resonator's eigenfrequencies. Specifically, all transversally magnetic (TM) modes¹² in the range of 0 – 1 GHz are sought. For that purpose, the excitation current's temporal dependence is chosen as the inverse Fourier transform of a Gauss function¹³ that is shifted and stretched to cover the desired frequency range. The time span in which the exciting current is discernibly different from zero is called t_{exc} . From a spatial point of view, we want to excite all azimuthal modes with $0 \leq m \leq m_{max}$. In order to achieve this, the current's amplitude along φ at a fixed radius is set as a superposition of sines and cosines up to the order of $m_{max} = N_\varphi/2$. If applicable, the automated mode detection (cf. Section 3.2.1.3) is used to detect and disable those azimuthal modes that do not contribute to eigenmodes in the excited frequency spectrum.

The mesh is configured to exhibit approximately $S_s = 10$ lines per minimum wavelength at worst, i.e. at the outer perimeter. The simulation is stopped at $t = 200t_{exc}$. Shortly after the excitation is decayed, i.e. in the steady state $t > t_{exc}$, a temporal probe signal of the electric grid voltage's z -component is recorded during the entire simulation at a fixed location. Afterwards, the probe signal is subjected to a Discrete Fourier Transform to obtain its frequency spectrum, which, in turn, resembles the spectrum of the simulated pillbox resonator.

For the sake of concision, abbreviations for the different algorithms, including their variants, are introduced and used throughout the rest of this section:

¹²These are modes consisting only of the components \hat{e}_z , \hat{h}_ϱ and \hat{h}_φ . In order for them to exist in the context of the FIT, a mesh consisting of only two points longitudinally is sufficient.

¹³The more obvious choice of a rectangular function in the frequency domain would lead to an infinitely long time domain signal. The Gaussian envelope translates into the time domain and can be reasonably truncated due to its exponential decay.

FDTD _{cy1}	The conventional FDTD method applied to cylindrical meshes without further adaption.
MM3D	The Multi-Mode algorithm coupled to a 3D mesh as in Section 3.2.1 including automated mode detection.
HNB	The Hybrid Newmark-Beta method from Section 3.2.2 with radially adapted β (Section 3.2.2.3) and precomputed LU factorization (Section 3.2.2.5).
HNB _c	Same as HNB, but with constant $\beta = 1/4$.
HNB _{noLU}	Same as HNB, but without precomputed LU factorization.
HNB3D	The combined approach (Section 3.2.3), i.e. MM3D with HNB in the inner domain (without automated mode detection).

The main objective of the introduced time domain methods for cylindrical meshes is to prevent the time step size from being diminished by short azimuthal edges. Each method's stability limit is calculable by its individually derived CFL criterion. The results from Table 3.1 show that each method successfully accomplishes this task.

	FDTD _{cy1}	MM3D	HNB	HNB _c	HNB _{noLU}	HNB3D
Δt in ps	1.86	7.38	64.19	78.62	64.19	59.50

Table 3.1.: Largest numerically stable time step size Δt . The value for MM3D is taken after the automated mode detection has eliminated all negligible azimuthal modes.

For comparison, an equidistant Cartesian mesh would, just like HNB, yield a time step size of 64.19 ps, if we assume the same number of lines per wavelength S_s . Therefore, the increase in employable time step size of the proposed methods compared to FDTD_{cy1} seems to be drastic, but in fact barely compensates the previous degradation due to the introduction of the cylindrical mesh. These methods are therefore unlikely to outperform a comparable time domain simulation on a Cartesian mesh in terms of speed, but, in turn, offer the possibility to capture a circular structure's details in a much more accurate and simple fashion. In order to achieve similar levels of accuracy on Cartesian meshes, we would either have to employ a higher spatial sampling rate S_s , or more elaborate methods for material discretization (cf. Chapter 4).

Having noted that each introduced approach fulfills the basic requirement of an increased time step size, it remains to see how they turn out with respect to speedup of the entire simulation and, furthermore, accuracy.

3.2.4.1. Impact on Simulation Speed

The speed question is addressed by implementing each algorithm on the same machine¹⁴, the same programming environment¹⁵ and a comparable level of optimization. The time for performing the actual update schemes is then measured, with results given in the first row of Table 3.2. The second row indicates how fast (in average) a single update cycle is completed.

Time for	FDTD _{cy1}	MM3D	HNB	HNB _c	HNB _{noLU}	HNB3D
all cycles in s	930	227	54	45	201	47
one cycle in μ s	1.02	0.99	2.05	2.08	7.61	1.65

Table 3.2.: Overall execution time for all necessary field update cycles and the average time required for each individual update cycle.

The execution time compared to conventional FDTD is significantly shortened in all cases. But there are mentionable differences, whose origins are discussed in the following.

MM3D's speedup is relatively low in this example, mainly because its time step size is smaller than that of the other specialized approaches (cf. Table 3.1). And it is even smaller initially (1.18 ps), i.e. before the automated mode detection has successfully recognized that only few azimuthal modes are of interest. The detection works by monitoring each azimuthal mode's energy and rejecting those modes, whose energy drops below 10^{-5} times the total energy. As expected, this comprises all azimuthal modes whose order m is higher than that of any eigenmode in the excited frequency spectrum. In this example, all azimuthal modes whose order ranges from $m = 16$ up to $m = \frac{N_\varphi - 1}{2} = 94$ are omitted, which reduces the degrees of freedom by a factor of 3.45.

The outcome of MM3D obviously depends on the underlying problem. The simulated structure needs to be rotationally symmetric up to a reasonably high radius ϱ_{BOR} . Additionally, if many especially high order azimuthal modes are required to accurately describe the present fields, or if the automated mode detection does not eliminate the others reliably, then other methods are probably better suited. If, on the other hand, the simulation covers a very long range of time (and therefore lots of update cycles) MM3D becomes competitive again because a single update cycle consumes less time (cf. Table 3.2).

¹⁴Intel Core i7-4770K, 16 GB RAM.

¹⁵Mathworks MATLAB R2014b [Mat14].

A fundamentally different approach is Hybrid Newmark-Beta, whose results are shown in Table 3.2 for three variations, each of them being significantly faster than FDTD_{cy1} . From an algebraic point of view, HNB and HNB_{noLU} are identical. We only optimize the solution of linear systems of equations in HNB by precomputing their LU decompositions. Because HNB_{noLU} is drastically slower it is no longer considered from now on. Due to the complete elimination of the azimuthal term in the CFL criterion (3.16), HNB_c 's time step size is even larger than HNB's. Subsequently, an even higher speedup compared to HNB is achievable. The distinctly increased time step size of all Hybrid Newmark-Beta variants comes at the expense of higher computational effort per time step due to semi-implicit update schemes.

The combined approach, HNB3D, just like MM3D, has a domain discretized by a conventional three-dimensional mesh at its outer perimeter. Therefore, even though its rotationally symmetric inner part is treated with the Hybrid Newmark-Beta method, its global time step size is slightly smaller than HNB's. But the entirely explicit update scheme consumes less time per cycle than the partially implicit scheme of HNB. This explains the additional speedup, which would turn out to be even higher with longer simulation time spans. Also, we can take all azimuthal modes into account without time step size degradation like in MM3D. Because of that, the automated mode detection is no longer required.

3.2.4.2. Impact on Accuracy

Predictions about each method's outcome on its simulation results' accuracy are made in their respective section. We extract the probe signals' resonance frequencies and compare them to analytical reference solutions¹⁶ in order to validate these predictions.

Figure 3.10 shows the magnitude of the probe signals' Discrete Fourier Transforms over a subrange of the frequency spectrum of interest for each method separately.

Not only do all graphs appear to be very similar, their peaks also correspond closely to the analytically calculated resonance frequencies. Accordingly, each method can be considered as a reasonable numerical simulation technique, at least qualitatively.

In order to retrieve the resonance frequencies accurately from the probe signals and assess them quantitatively, the concept of *Harmonic Inversion* [MT98] is used. It is implemented by the open source software package *Harminv* [Joh06] and, amongst other information, returns a list of all detected resonance frequencies.

¹⁶For the exact formula of a pillbox resonator's resonance frequencies and its deduction, the reader is referred to [Jac98].

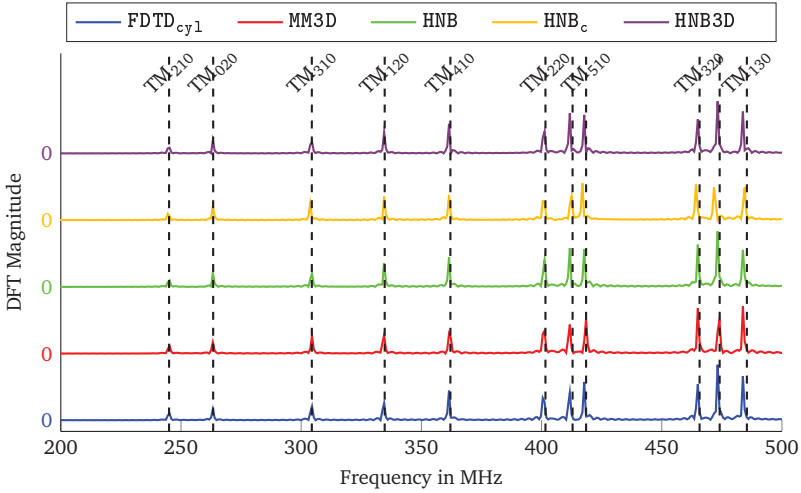


Figure 3.10.: Excerpt from frequency spectra of temporal probe signals. Analytical reference solutions are given by dashed lines.

Each mode's deviation from the respective analytical solution is then computed and visualized in Fig 3.11.

It shows that resonances at high frequencies tend to exhibit larger simulation error than those at lower frequencies, independent of the employed simulation method. This is due to the fact that the spatial sampling rate S_s is specified for the lowest wavelength (i.e. highest frequency) and gradually increases the lower the frequency gets. Either the azimuthal order or the radial order can change from mode to mode¹⁷. Typically, an increase of the latter has a higher impact on the resulting field's variation. In this case, the spatial discretization accuracy becomes worse compared to an increase of the azimuthal mode order. This explains the error's non-uniform increase with the frequency.

More importantly, the previously made predictions about each method's impact on accuracy reflect in the results shown in Fig. 3.11. Compared to FDTD_{cyl} , the average resonance error is obviously lower in case of the newly introduced methods. Only HNB_c performs worse, which emphasizes the importance of choosing β as small as possible or, as in HNB 's case, even radially adjusted.

¹⁷The longitudinal mode order does not vary for the present set of parameters and equals zero for each mode.

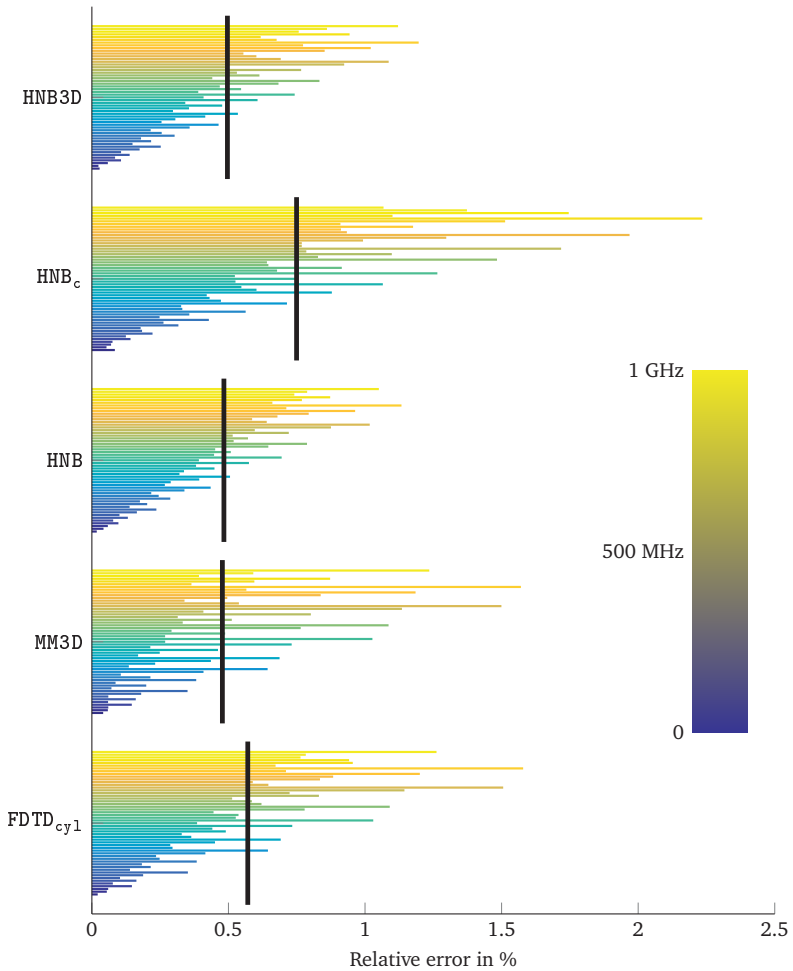


Figure 3.11.: Relative error of the pillbox cavity's resonance frequencies for TM modes between 0 and 1 GHz. The mean error of each particular method is represented by black lines.

The results presented above originate from only one particular numerical example and by no means raise any claim for universal validity. They are rather supposed to validate the theoretically motivated predictions and to provide better comprehension for reasoning about the effects on real world applications.

3.3. Summary

As explained in detail in Section 3.1.3, FDTD in its pristine formulation is not well suited for being applied to cylindrical mesh systems. Both the simulation speed and accuracy suffer from the severe degradation of the highest stable time step size. By means of the energy method, we derive these limits for various kinds of meshes in Section 3.1.

Approaches that compensate the time step size issues are presented in Section 3.2. Basically, they rely either on domain decomposition with more elaborate treatment of the inner domain, or on a special incorporation of the Newmark-Beta extension.

The Multi-Mode approach (cf. Section 3.2.1, abbr. MM3D), which belongs to the former category, requires the simulated object to be rotationally symmetric up to a reasonably large radius and can only work efficiently if the simulated fields are smooth in a specific way. Compared to conventional FDTD (FDTD_{cy1}), it is likely to offer improved speed and accuracy, but, in turn, lacks universal applicability. However, if a priori knowledge of the field's behavior, especially about its azimuthal modes, is available, this technique offers otherwise unachievable potential.

The second category comprises the Hybrid Newmark-Beta method (HNB) and relies on an entirely three-dimensional mesh, just like FDTD_{cy1} does. Likewise, there are no further limitations concerning the object's spatial properties. By means of its alternative time integration scheme, we are able to significantly speed up the simulation and improve accuracy. For that purpose, it is important to incorporate the proposed enhancements of a radially adjusted parameter β (cf. Section 3.2.2.3) and the precomputed LU factorizations (cf. Section 3.2.2.5). The enhancements' omission results in strongly deteriorated accuracy or a very slow update scheme, respectively. It is advisable to use this technique especially if rotational symmetry is not exploitable by means of MM3D.

Another simulation method is obtained by combining both approaches (cf. Section 3.2.3, abbr. HNB3D). From a spatial point of view it is not as flexible as FDTD_{cy1} or HNB because, like MM3D, it requires a certain extent of rotational symmetry. However, the incorporation of the Hybrid Newmark-Beta scheme to the Multi-Mode domain enables each azimuthal mode to be included in the simulation without any influence on the time step size. Opposed to HNB, the update scheme

remains completely explicit, which, in combination with a large time step size, makes this method very fast, especially for long time spans to be simulated.

Table 3.3 highlights each method's strengths and weaknesses and allows for direct comparison.

Rating	FDTD _{cy1}	MM3D	HNB	HNB _c	HNB _{noLU}	HNB3D
Universality	++	-	++	++	++	+
Speed	--	-	+	+	-	++
Accuracy	-	++	++	--	++	++

Table 3.3.: Each method ranked in categories of universal applicability, speed and accuracy.

Nonconformal Material Interfaces

Cylindrical meshes, like those that are subjected to a detailed treatment in the previous chapter, can unfold their full potential if the simulated structure is circularly shaped. The key concept is to choose the FIT's underlying mesh system so that its facets directly match the material interfaces. However, if said material interfaces are no longer shaped in alignment with an orthogonal coordinate system's axes, it is impossible to find an orthogonal mesh that fulfills this property in general. One way to alleviate this problem, whose consequences are described in detail in the course of this chapter, is to employ an unstructured (most commonly tetrahedral) mesh that adapts well to arbitrarily shaped material discontinuities. Regardless of the simulation method¹, unstructured meshes are likely to imply nondiagonal material matrices, which are costly to invert and, therefore, limit the number of employable mesh cells.

Opposed to the previous chapter, we dismiss the endeavor of material-conforming meshes from now on and resort to efficiently implementable Cartesian meshes, regardless of a possible misalignment between material interfaces and mesh facets. In order to compensate the expectable loss of accuracy, we investigate possibilities to deal with such material interfaces, which we henceforth refer to as *nonconformal*, in an improved way. Practical ways of approximating and implementing the ideal material coefficients (2.19) are the key spot for such measures.

This chapter is structured as follows. We assess conventional methods of material averaging and highlight their restrictive conditions on the conformity between mesh and material. An extended formula is then examined with regard to its potential benefit and ways in order to achieve it. Within its scope, the loss of accuracy of conventional methods is characterized. A numerical example with known reference solution is consulted several times in order to validate the formal predictions. The chapter concludes with some important remarks about employed simplifications that mainly serve the purpose of better comprehension and how to extend the discussed methods to more complex cases.

In a condensed and with regard to some points tentative fashion, the methods and findings presented in this chapter are published by the author in [KCS14a; KKS16].

¹The Finite Element Method [Mono3] is usually preferred over the Finite Integration Technique on tetrahedral meshes [Büs11], because of its more convenient extensibility to higher order basis functions.

4.1. The Conformal Case

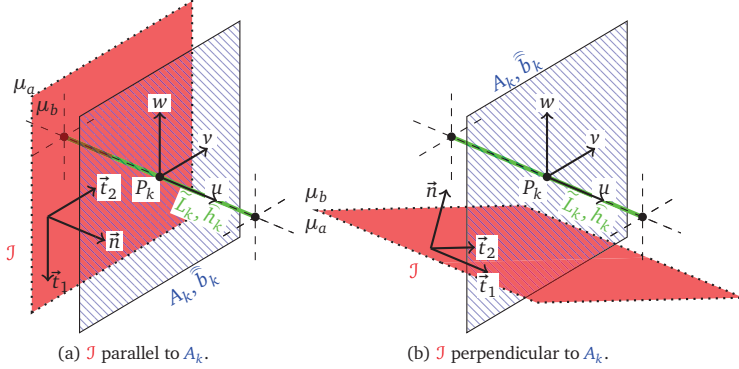


Figure 4.1.: A primary mesh facet A_k and its corresponding dual edge \tilde{L}_k intersect each other in P_k . The material interface \mathcal{J} separates the computational domain in two parts with different permeabilities (μ_a and μ_b).

As depicted in Fig. 4.1, we assume the local material interface \mathcal{J} to be parallel (Fig. 4.1a) or perpendicular (Fig. 4.1b) to an u -directed primary facet A_k ². More precisely, the interface's local normal vector \vec{n} either satisfies $\vec{n} \cdot \vec{e}_u = 1$ or $\vec{n} \cdot \vec{e}_u = 0$. In the scope of this thesis, this is referred to as the *conformal case*³. Consequently, the dot products in (2.19b) lead to scalar integrands that comprise either strictly normal or tangential field components with respect to the interface \mathcal{J} :

$$M_{\mu,k} = \frac{\int_{A_k} \vec{B} \cdot d\vec{A}}{\int_{\tilde{L}_k} \vec{H} \cdot d\vec{s}} = \begin{cases} \frac{\int_{A_k} B_n dA}{\int_{\tilde{L}_k} H_n ds} = \frac{\int_{A_k} B_n dA}{\int_{\tilde{L}_k} \mu^{-1} B_n ds}, & \text{if } \mathcal{J} \parallel A_k & (4.1a) \\ \frac{\int_{A_k} B_t dA}{\int_{\tilde{L}_k} H_t ds} = \frac{\int_{A_k} \mu H_t dA}{\int_{\tilde{L}_k} H_t ds}, & \text{if } \mathcal{J} \perp A_k & (4.1b) \end{cases}$$

²For the sake of simplicity we consider only planar interfaces. Furthermore, we preliminarily restrict ourselves to interfaces between magnetic materials with different permeabilities. Remarks on alleviating these restrictions can be found in Section 4.5.1.

³Note that this definition is weaker than what is commonly understood as a conformal mesh, i.e. a mesh with entirely filled primary cells. Even tilted interfaces in the perpendicular case, like in Fig. 4.1b, are permitted, as long as $\vec{n} \cdot \vec{e}_u = 0$.

In the last steps, the piecewise constant permeability μ is used to obtain only those field components that are continuous across the interface, i.e. H_t and B_n , where H_t stands for the u -directed tangential component (cf. Fig. 4.1b). We expand each of them into Taylor series around the intersection point P_k of primary facet and dual edge. Without loss of generality, this point is assumed to coincide with the local (u, v, w) coordinate system's origin:

$$\Psi = \Psi|_{P_k} + \begin{cases} \left. \frac{\partial \Psi}{\partial u} \right|_{P_k} u + \left. \frac{\partial^2 \Psi}{\partial u^2} \right|_{P_k} \frac{u^2}{2} + \mathcal{O}(u^3), & \text{on } \tilde{L}_k \\ \left. \frac{\partial \Psi}{\partial v} \right|_{P_k} v + \left. \frac{\partial \Psi}{\partial w} \right|_{P_k} w + \mathcal{O}(v^2, w^2), & \text{on } A_k \end{cases} \quad (4.2a)$$

The placeholder Ψ stands for H_t or B_n . Inserting (4.2) into (4.1) enables the integrations to be carried out analytically if the integrals are split across the two domains with constant permeability μ_a and μ_b . We introduce operators that represent a weighted averaging of the (inverse) permeability:

$$\langle \mu^{-1} \rangle_{\tilde{L}_k} = \frac{\tilde{l}_k^a / \mu_a + \tilde{l}_k^b / \mu_b}{\tilde{L}_k} \quad (4.3a)$$

$$\langle \mu \rangle_{A_k} = \frac{A_k^a \mu_a + A_k^b \mu_b}{A_k} \quad (4.3b)$$

Therein, A_k^a stands for the part of A_k that lies inside domain a (and so forth). We obtain⁴:

$$M_{\mu,k} = \begin{cases} \frac{A_k + \mathcal{O}(\Delta^4)}{\tilde{L}_k \langle \mu^{-1} \rangle_{\tilde{L}_k} + \mathcal{O}(\Delta^2)} = \underbrace{\frac{A_k}{\tilde{L}_k \langle \mu^{-1} \rangle_{\tilde{L}_k}}}_{M_{\mu,k}^{\parallel}} + \mathcal{O}(\Delta^2), & \text{if } \mathcal{J} \parallel A_k \\ \frac{A_k \langle \mu \rangle_{A_k} + \mathcal{O}(\Delta^3)}{\tilde{L}_k + \mathcal{O}(\Delta^3)} = \underbrace{\frac{A_k \langle \mu \rangle_{A_k}}{\tilde{L}_k}}_{M_{\mu,k}^{\perp}} + \mathcal{O}(\Delta^2), & \text{if } \mathcal{J} \perp A_k \end{cases} \quad (4.4a)$$

In order to simplify the handling of higher order terms, expressed by the Landau operator \mathcal{O} , the primary facet's area and the dual edge's length are considered

⁴For a detailed deduction of the resulting convergence rate from those of numerator and denominator, the reader is referred to Appendix C.1

asymptotically in terms of the largest mesh step size $\Delta = \max\{\Delta x, \Delta y, \Delta z\}$. Thus, the expressions $A_k \in \mathcal{O}(\Delta^2)$ and $\tilde{L}_k \in \mathcal{O}(\Delta)$ hold and are employed to deduce the given absolute error terms in (4.4). For (4.4a), it is also given in [Rie89].

It is important to stress that the entire deduction so far strongly depends on conformal, i.e. strictly parallel or perpendicular interfaces with respect to the mesh, which is a severe restriction for practical applications. As already briefly discussed in the opening of Chapter 3, these conditions can be easily enforced by altering the investigated object. Most commonly, this is achieved through the staircase approximation (cf. Fig. 3.1b). We address the implications of such a material modification in Section 4.2.1.

Note that if the interface does not run exactly through the intersection point P_k , refining the mesh may cause the pair of voltage and flux k to be no longer cut by the interface. Therefore, all mentioned convergence rates have to be understood in the context of a mesh refinement that leaves the intersection point's relative position to the interface unaltered.

4.2. The Nonconformal Case

In the following, we derive an approximation to the ideal material coefficient $M_{\mu,k}$ without requiring the interface to be parallel or perpendicular to the mesh. We only suppose it to be reasonably smooth in the mesh cell limit so that no mesh edge or facet is multiply cut. For the sake of brevity, we assume the entire computational domain to be homogeneous along z , which allows us to restrict all considerations to the x - y -plane and leaves us with only one tangential vector \vec{t} with respect to the interface. In terms of the angle θ , as shown in Fig. 4.2, we obtain $\vec{t} = [\cos \theta, \sin \theta]^T$ and $\vec{n} = [-\sin \theta, \cos \theta]^T$.

In analogy to Section 4.1, we originate from (2.19b), split the integrals at the interface and evaluate the occurring dot products, now in dependence of the interface angle θ . The primary facet A_k and dual edge \tilde{L}_k are thereby split into parts that lie completely inside the domain a or b and are indexed accordingly:

$$M_{\mu,k} = \frac{\widehat{b}_k}{\widehat{h}_k} = \frac{\int_{A_k} \vec{B} \cdot d\vec{A}}{\int_{\tilde{L}_k} \vec{H} \cdot d\vec{s}} \quad (4.5a)$$

$$= \frac{\int_{A_k^a} (B_t^a \cos \theta - B_n^a \sin \theta) dA + \int_{A_k^b} (B_t^b \cos \theta - B_n^b \sin \theta) dA}{\int_{\tilde{L}_k^a} (H_t^a \cos \theta - H_n^a \sin \theta) ds + \int_{\tilde{L}_k^b} (H_t^b \cos \theta - H_n^b \sin \theta) ds} \quad (4.5b)$$

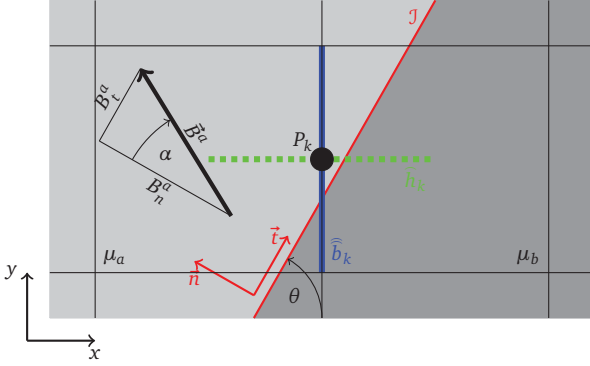


Figure 4.2.: A material interface \mathcal{J} that encloses the angle θ with the mesh. The field \vec{B}^a is decomposed into tangential and normal components with respect to \mathcal{J} .

By means of the continuity conditions (2.4) and the permeabilities μ_a and μ_b , the material coefficient (4.5b) transforms to the following expression, which only contains interface-continuous field components from domain a :

$$M_{\mu,k} = \frac{\int_{A_k^a} (\mu_a H_t^a \cos \theta - B_n^a \sin \theta) dA + \int_{A_k^b} (\mu_b H_t^a \cos \theta - B_n^a \sin \theta) dA}{\int_{\tilde{L}_k^a} (H_t^a \cos \theta - \frac{1}{\mu_a} B_n^a \sin \theta) ds + \int_{\tilde{L}_k^b} (H_t^a \cos \theta - \frac{1}{\mu_b} B_n^a \sin \theta) ds} \quad (4.6)$$

The Taylor series expansions (4.2) are now substituted for the integrands. After we carry out the integrations for low order terms and conceal the remaining terms behind the Landau operator, we obtain:

$$M_{\mu,k} = \frac{[H_t^a \cos \theta]_{P_k} (A_k^a \mu_a + A_k^b \mu_b) - [B_n^a \sin \theta]_{P_k} A_k + \mathcal{O}(\Delta^3)}{[H_t^a \cos \theta]_{P_k} \tilde{L}_k - [B_n^a \sin \theta]_{P_k} (\tilde{L}_k^a \frac{1}{\mu_a} + \tilde{L}_k^b \frac{1}{\mu_b}) + \mathcal{O}(\Delta^2)} \quad (4.7a)$$

$$= \frac{A_k [H_t^a \cos \theta]_{P_k} \langle \mu \rangle_{A_k} - [B_n^a \sin \theta]_{P_k}}{\tilde{L}_k [H_t^a \cos \theta]_{P_k} - [B_n^a \sin \theta]_{P_k} \langle \mu^{-1} \rangle_{\tilde{L}_k}} + \mathcal{O}(\Delta^2) \quad (4.7b)$$

$$= \underbrace{\frac{A_k}{\tilde{L}_k} \frac{\langle \mu \rangle_{A_k} \tan \alpha_k - \mu_a \tan \theta_k}{\tan \alpha_k - \mu_a \langle \mu^{-1} \rangle_{\tilde{L}_k} \tan \theta_k}}_{M_{\mu,k}'} + \mathcal{O}(\Delta^2) \quad (4.7c)$$

Appendix C.1 gives more detailed insight into the deduction. The last reformulation (4.7c) makes use of the fact that all field components can be expressed in terms of the field's Euclidean norm $|\vec{B}^a|$ (which subsequently cancels out) and the sine or the cosine of the field angle α . Instead of the square bracket notation $[\cdot]_{p_k}$, we indicate that the angles θ and α need to be evaluated for each k individually by indexing them accordingly.

The second order converging approximation $M_{\mu,k}^{\angle}$ is the so called *generalized material coefficient*. It is also introduced in similar form in [Scho5], but without consideration of its convergence rate. It should be noted that the derivation so far only considers x -directed edges and facets. For y -coefficients the angle θ_k has to be substituted by $\theta_k \rightarrow \theta_k \pm \pi/2$. In the course of this chapter, we investigate $M_{\mu,k}^{\angle}$ only for angles in the range of $-\pi/2 < \alpha_k \leq \pi/2$ and $-\pi/2 < \theta_k \leq \pi/2$, which is sufficient because of its π -periodicity both in α_k and θ_k .

It becomes clear that this coefficient contains the conventional approaches $M_{\mu,k}^{\parallel}$ and $M_{\mu,k}^{\perp}$ as special cases by examining (4.7c). They emerge under the following circumstances:

$$M_{\mu,k}^{\angle} = \begin{cases} M_{\mu,k}^{\parallel}, & \text{if } (\theta_k = \pi/2 \iff \mathcal{J} \parallel A_k) \text{ or } (\alpha_k = 0) & (4.8a) \\ M_{\mu,k}^{\perp}, & \text{if } (\theta_k = 0 \iff \mathcal{J} \perp A_k) \text{ or } (\alpha_k = \pi/2) & (4.8b) \end{cases}$$

Apparently, they do not only occur if the interface is indeed parallel or perpendicular to the primary facet, as shown in Section 4.1. Second order accurate approximations to the continuous material coefficient $M_{\mu,k}$ are obviously also achievable by means of $M_{\mu,k}^{\parallel}$ and $M_{\mu,k}^{\perp}$ if the magnetic field stands normally ($\alpha_k = 0$) or tangentially ($\alpha_k = \pi/2$) to the interface \mathcal{J} . This behavior is also reported in [Scho5] and can be utilized to estimate which approximation is better suited in the nonconformal case based on a priori knowledge about the fields [CBS12].

4.2.1. Artificially Induced Application of Conventional Coefficients

We make use of the generalized coefficient's explicitly outlined deduction to derive statements about the convergence rates of the conventional approximation $M_{\mu,k}^{\perp}$ (or $M_{\mu,k}^{\parallel}$) in case of a foregoing modification of the investigated object, so that it locally fulfills $\mathcal{J} \perp A_k$ (or $\mathcal{J} \parallel A_k$). The desired neglect of H_t^a (or B_n^a) can be achieved by substitution of the associated terms in (4.6) for $\mathcal{O}(1)$. Consequently, the resulting

approximations are the same as if the interface fulfilled the conformity conditions:

$$M_{\mu,k} = \begin{cases} \frac{A_k \langle \mu \rangle_{A_k} + \mathcal{O}(\Delta^2)}{\tilde{L}_k + \mathcal{O}(\Delta)} = M_{\mu,k}^\perp + \mathcal{O}(\Delta), & \text{if } \mathcal{J} \not\llcorner A_k & (4.9a) \\ \frac{A_k + \mathcal{O}(\Delta^2)}{\tilde{L}_k \langle \mu^{-1} \rangle_{\tilde{L}_k} + \mathcal{O}(\Delta)} = M_{\mu,k}^\parallel + \mathcal{O}(\Delta), & \text{if } \mathcal{J} \llcorner A_k & (4.9b) \end{cases}$$

However, the coefficients' convergence rates turn out to be linear, which we formally prove in the framework of the generalized material coefficient. A statement of this proof in a more elaborate fashion can be found in Appendix C.2.

This approach can be interpreted as a generalization of the staircase approximation. Since we lower our requirements on the definition of conformity (cf. Footnote 3 on page 62), (4.9) is valid even for interfaces like those shown in Fig. 4.1. The standard staircase approximation, on the other hand, typically demands entirely filled primary mesh cells [Hol93], possibly in combination with triangularly (in 3D: pyramiddally or prismatically) filled mesh cells [Wei79]. We can exploit this fact in two ways. Either the material interfaces are a priori conformal according to the weakened definition used herein and we can directly subject them to a second order accurate discretization by means of (4.4), or we can slightly modify their shape and obtain a first order converging, yet more accurate than standard staircase, discretization by means of (4.9). Therefore, we point out that it is misleading to judge mesh quality in terms of the exact congruency between mesh facets and material interfaces. Accordingly, the occurrence of partially filled mesh cells does not necessarily imply a degradation of the convergence rate, because all material coefficients are based on edge/facet-pairs and not on mesh cells. From a practical perspective, however, this makes higher demands on a mesh generator. Instead of only deciding which cell gets assigned which set of material parameters, it has to evaluate cut ratios based on the object's CAD⁵ representation.

4.2.2. Bulk Material

So far we assume that for each canonical index k the respective primary facet or dual edge are actually cut by the material interface. If this is not the case, like for instance in bulk material apart from material interfaces, all three approximations equal each other. They converge quadratically or even cubically, depending on whether or not the Taylor series' expansion point P_k divides the dual edge \tilde{L}_k into

⁵Computer aided design.

equal parts⁶, which also follows from Taylor series expansions inserted in (4.6):

$$M_{\mu,k} = \begin{cases} M_{\mu,k}^{\perp} \\ M_{\mu,k}^{\parallel} \\ M_{\mu,k}^{\angle} \end{cases} + \begin{cases} \mathcal{O}(\Delta^3), & \text{for central expansion point} \\ \mathcal{O}(\Delta^2), & \text{else} \end{cases} \quad (4.10)$$

The convergence rates of $M_{\mu,k}^{\parallel}$ are also given in [CW01; Scho5] for entirely filled mesh cells and for bulk material.

4.2.3. Implications of the Generalized Material Coefficient

In the following, we investigate the implications that the generalized coefficient entails in comparison to the conventional ones. Table 4.1 summarizes at which rate each approximation converges under given circumstances for a pair of voltage and flux k that is cut by a material interface.

	$\theta_k = 0$	$\theta_k = \pi/2$	$\alpha_k = 0$	$\alpha_k = \pi/2$	else
$M_{\mu,k}^{\parallel}$	$\mathcal{O}(\Delta)$	$\mathcal{O}(\Delta^2)$	$\mathcal{O}(\Delta^2)$	$\mathcal{O}(\Delta)$	$\mathcal{O}(\Delta)$
$M_{\mu,k}^{\perp}$	$\mathcal{O}(\Delta^2)$	$\mathcal{O}(\Delta)$	$\mathcal{O}(\Delta)$	$\mathcal{O}(\Delta^2)$	$\mathcal{O}(\Delta)$
$M_{\mu,k}^{\angle}$	$\mathcal{O}(\Delta^2)$	$\mathcal{O}(\Delta^2)$	$\mathcal{O}(\Delta^2)$	$\mathcal{O}(\Delta^2)$	$\mathcal{O}(\Delta^2)$

Table 4.1.: Convergence rates of the absolute error of approximations of the ideal material coefficient $M_{\mu,k}$.

4.2.3.1. Convergence Rate of Simulation Results

It is important to stress that all convergence rates given so far only describe how fast the approximations $M_{\mu,k}^{\parallel}$, $M_{\mu,k}^{\perp}$ and $M_{\mu,k}^{\angle}$ converge against the exact material coefficient $M_{\mu,k}$. What this implies for the convergence rate of results obtained by means of the Finite Integration Technique is the subject of the following discussion. For clear distinction, we use the term *local convergence* for the approximated material coefficients' asymptotic behavior, while the FIT's convergence is referred to as *global*.

The literature commonly refers to the FIT and related schemes like FDTD as second order accurate methods [TH05]. However, in the context of conventional material modeling this implies that all interfaces conform with the mesh in a way that lets the local material coefficient converge at least quadratically, as shown in

⁶Equidistant, orthogonal meshes ensure this property.

[Gus75]⁷. Conversely, if we need to modify the material in order to apply one of the approximations $M_{\mu,k}^{\parallel}$ or $M_{\mu,k}^{\perp}$ (cf. (4.9)), only linear global convergence can be expected [DDH01]. In common practical applications, only a small fraction of mesh cells are cut by the material interface. The majority of material coefficients converge at least quadratically (cf. (4.10)). As a result, the effectively measurable global convergence rate usually lies between first and second order [WBC13].

Nevertheless, these findings make it highly desirable to give up the treatment of nonconformal materials by conventional coefficients in favor of the generalized material coefficient $M_{\mu,k}^{\angle}$, which is shown to converge quadratically in any event (cf. last row of Table 4.1). Without the abandonment of conventional material coefficients, the Finite Integration Technique can not be guaranteed to yield second order accurate results for nonconformal materials.

4.2.3.2. Numerical Properties

An introductory discussion on the generalized coefficient's numerical properties can be found in [Scho5]. The results presented therein are suggested to be of general validity, even though only a limited domain of values for θ_k and α_k is investigated. Transferred to this thesis' definitions, the key result is that the generalized coefficient $M_{\mu,k}^{\angle}$ is bounded by $M_{\mu,k}^{\parallel}$ and $M_{\mu,k}^{\perp}$. While this is unquestionably true in the assessed domain $(\theta_k, \alpha_k) \in [-\pi/2, 0] \times [0, \pi/2]$ and, by symmetry, also in $(\theta_k, \alpha_k) \in [0, \pi/2] \times [-\pi/2, 0]$, it cannot hold in any other case.

Fig. 4.3 clearly shows the predicted boundedness in the second and fourth quadrant. However, in the first and third quadrant, the coefficient takes up values outside of this range and even exhibits poles and zeros. We can analytically deduce this behavior from its definition (4.7c) by calculating zeros of the numerator and denominator:

$$M_{\mu,k}^{\angle} = 0 \iff \frac{\tan \alpha_k}{\tan \theta_k} = \frac{\mu_a}{\langle \mu \rangle_{A_k}} \quad (4.11a)$$

$$M_{\mu,k}^{\angle} \rightarrow \pm \infty \iff \frac{\tan \alpha_k}{\tan \theta_k} = \mu_a \langle \mu^{-1} \rangle_{\bar{L}_k} \quad (4.11b)$$

Due to the right hand sides' unconditional positivity, the effect of unbounded values occurs regardless of a specific example every time θ_k and α_k have the same sign. As we will see in the following section, this case is by no means irrelevant in

⁷Especially in the FDTD related literature, the material coefficient is usually defined in terms of fields and flux densities themselves, instead of spatial integrals thereof. This results in local convergence rates that are one order smaller than those given here.

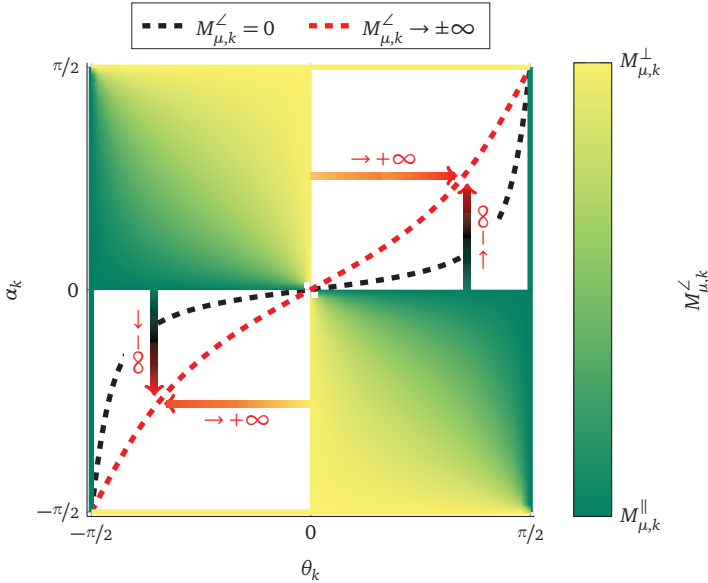


Figure 4.3.: The generalized coefficient $M_{\mu,k}^{\angle}$ in dependence of field angle α_k and interface angle θ_k for $\mu_a = \mu_0$ and $\mu_b = 15\mu_0$.

practice and leads to various consequences that need to be accounted for. These consequences are discussed more closely and in a broader context in Section 4.5.1.4.

4.3. Validation

The so far only theoretically predicted results regarding accuracy and convergence rate are now demonstrated practically. Therefore, the following magnetostatic example with analytically known reference solution is employed.

As depicted in Fig. 4.4, a z -directed line current I_0 inside a medium with permeability μ_a is placed in front of a half-space with permeability μ_b . The domain is homogeneous along \tilde{z} , which reduces the problem's spatial dependence to \tilde{x} and \tilde{y} . Moreover, the vector potential \vec{A} reduces to its \tilde{z} -component $\vec{A} = A_{\tilde{z}}\vec{e}_{\tilde{z}}$. By further assuming a homogeneous domain $\mu_a = \mu_b = \mu$ and by Coulomb gauging [Jac98],

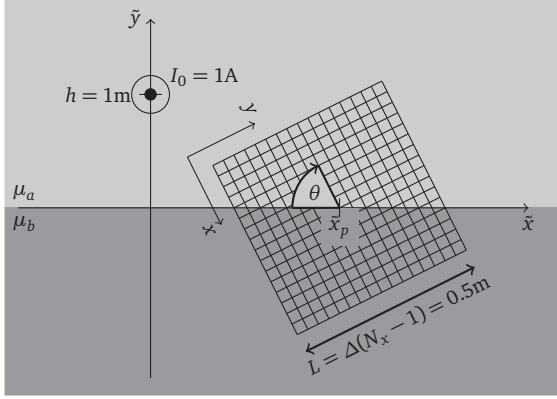


Figure 4.4.: An infinitely long line current I_0 in front of a magnetic material interface. The square region of interest is centered at $\tilde{x} = \tilde{x}_p$, tilted by θ and covered by a Cartesian mesh.

Maxwell's equation (2.2b) decomposes into a Poisson equation:

$$\nabla \times \vec{B} = \mu \vec{J} \quad \begin{matrix} \vec{B} = \nabla \times \vec{A} \\ \iff \end{matrix} \quad \nabla \times \nabla \times \vec{A} = \mu \vec{J} \quad (4.12a)$$

$$\begin{matrix} \nabla \cdot \vec{A} = 0 \\ \implies \end{matrix} \quad \nabla^2 \vec{A} = -\mu \vec{J} \quad \begin{matrix} \vec{A} = A_{\tilde{z}} \vec{e}_{\tilde{z}} \\ \implies \end{matrix} \quad \nabla^2 A_{\tilde{z}} = -\mu J_{\tilde{z}} \quad (4.12b)$$

In close analogy to the electrostatic case⁸ we can solve the inhomogeneous problem $\mu_a \neq \mu_b$ by means of the method of images [Jac98] and obtain:

$$A_{\tilde{z}} = \begin{cases} \frac{I_0 \mu_a}{2\pi} \left(\frac{\mu_a - \mu_b}{\mu_a + \mu_b} \ln \frac{\sqrt{\tilde{x}^2 + (h + \tilde{y})^2}}{|h|} \right. \\ \quad \left. \dots - \ln \frac{\sqrt{\tilde{x}^2 + (h - \tilde{y})^2}}{|h|} \right), & \text{if } \tilde{y} \geq 0 \\ -\frac{I_0 \mu_a \mu_b}{\pi(\mu_a + \mu_b)} \ln \frac{\sqrt{\tilde{x}^2 + (h - \tilde{y})^2}}{|h|}, & \text{if } \tilde{y} \leq 0 \end{cases} \quad (4.13a)$$

A square Cartesian mesh, as shown in Fig. 4.4, is introduced. Its center is located at $\tilde{x} = \tilde{x}_p$ and it is tilted by the angle θ . By that measure we yield a mesh with

⁸This analogy is applicable because the vector potential's \tilde{z} -component obeys the same kind of differential equation like the scalar potential Φ (cf. (2.6)).

partially filled cells in the familiar x - y -coordinate frame and can refer to the analytical solution (4.13) for the sake of comparison by means of a coordinate transformation.

4.3.1. Angle Dependence and Introduced Error

Preliminarily, not the entire mesh but only one voltage/flux-pair centered at $\tilde{x}_p = 0.5$ m is considered (cf. Fig. 4.5a). This enables approximations of the ideal material coefficient $M_\mu = \tilde{b}/\tilde{h}$ to be investigated in dependence of several parameters with regard to accuracy. The permeabilities are $\mu_a = \mu_0$ and $\mu_b = 15\mu_0$. Based on the magnetic flux density $\vec{B} = \nabla \times \vec{A}$, this leads to the field angle $\alpha = 7.60^\circ$. Furthermore, we analytically evaluate the integral quantities \tilde{h} and \tilde{b} and, thereby, obtain the ideal value M_μ as reference in dependence of θ and Δ .

For a fixed mesh step size Δ , the reference value and the discussed approximations are shown in Fig. 4.5b in dependence of the interface angle $\theta \in [-\pi/2, \pi/2]$. Since the conventional coefficients M_μ^\parallel and M_μ^\perp are constant regardless of θ , they approximate M_μ only reasonably well in the special cases they are derived for. The generalized coefficient M_μ^\angle , on the other hand, provides a much more accurate representation over the entire domain. Due to α 's positivity, the singularity and zero-crossing occurs for positive values of θ and, furthermore, coincide very well with those of M_μ .

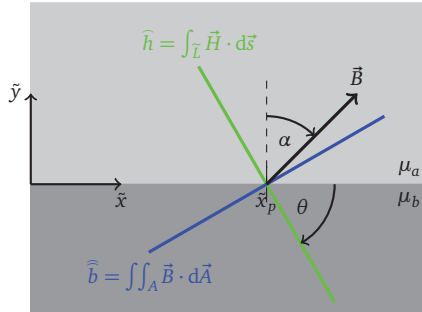
With regard to the confirmation of the convergence rates that are given in Table 4.1, we now choose the interface angle arbitrarily to $\theta = -\pi/3$, vary the mesh step size Δ and display the absolute error of the approximations. Fig. 4.5c shows that only the generalized coefficient M_μ^\angle achieves second order convergence, as expected from (4.7). The standard coefficients converge linearly due to the nonconformal mesh in agreement with the predictions made in (4.9).

4.3.2. Impact on Simulation Results

In the following, a complete two-dimensional mesh, as shown in Fig. 4.4, with a given number of points $N_p = N_x^2$ is used to investigate the convergence rate of discrete solutions of Maxwell's equations in the magnetostatic case.

If the mesh's extent and position are chosen so that it does not cover the position of the excitation current I_0 , (4.12b) simplifies to a Laplace equation for the vector potential's \tilde{z} -component:

$$\nabla^2 A_{\tilde{z}} = 0 \tag{4.14}$$



(a) Excerpt from Fig. 4.4 with a tilted pair of grid voltage \widehat{h} and flux \widehat{b} , defined on an edge \widetilde{L} (length Δ) and a facet A (area Δ^2).

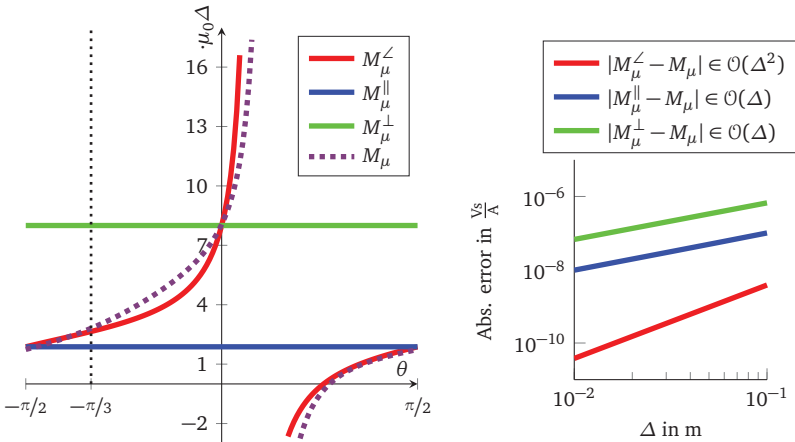


Figure 4.5.: Numerical setup and comparison of the exact matrix coefficient $M_\mu = \widehat{b}/\widehat{h}$ with its approximations.

In the scope of the Finite Integration Technique and based on (2.15), a similar deduction like in (4.12) for the meshed domain leads to a discrete Laplace equation⁹:

$$\mathbf{C}^T \mathbf{M}_{\mu^{-1}} \mathbf{C} \hat{\mathbf{a}}_z = \mathbf{0} \quad (4.15)$$

We now consider (4.15) as a Dirichlet boundary value problem [Hen15], for which we take the edge-integrated vector potentials $\hat{\mathbf{a}}_z$ on the mesh's outer boundary from the analytical solution (4.13) and incorporate them into (4.15). Opposed to the vector of reference values $\hat{\mathbf{a}}_{z,\text{ref}}$, the solution $\hat{\mathbf{a}}_z$ of the modified system of equations is influenced by the way the coefficients of the matrix¹⁰ $\mathbf{M}_{\mu^{-1}}$ are approximated. A suitable measure for accuracy and, through a variation of the mesh resolution, the global convergence rate is the solution vector's relative error norm:

$$\mathbb{E} = \frac{\|\hat{\mathbf{a}}_z - \hat{\mathbf{a}}_{z,\text{ref}}\|_2}{\|\hat{\mathbf{a}}_{z,\text{ref}}\|_2} \quad (4.16)$$

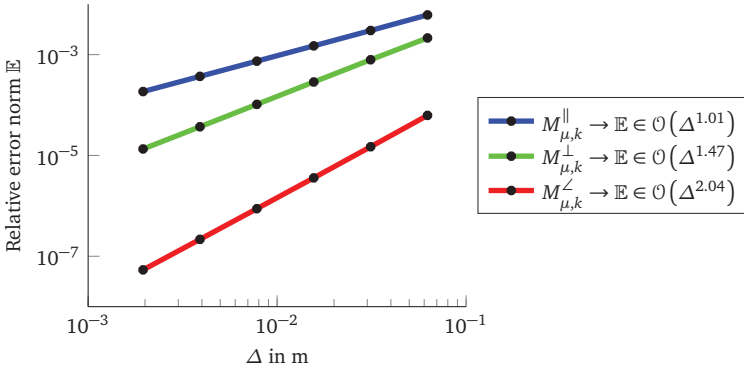


Figure 4.6.: Relative error norm of the discrete vector potential for different approximations of the ideal material coefficient M_{μ} in dependence of Δ .

The results, shown in Fig. 4.6, support the theoretical predictions made in Section 4.2.3.1. The relative error that is caused by the conventional approximations

⁹The N_p -vector $\hat{\mathbf{a}}_z$ incorporates line integrals of A_z over z -directed primary edges. The curl matrix in this case reduces to $\mathbf{C} = \begin{bmatrix} \mathbf{p}_y \\ -\mathbf{p}_x \end{bmatrix}$.

¹⁰In contrast to Chapter 3, we resort to the formulation $\mathbf{M}_{\mu^{-1}}$, by which we mean the material matrix based on the reluctivity μ^{-1} instead of the inverse permeability matrix \mathbf{M}_{μ}^{-1} . In this context, these matrices have to be strictly distinguished, as discussed in Section 4.4.2.

$M_{\mu,k}^{\parallel}$ and $M_{\mu,k}^{\perp}$ converges linearly (or slightly faster, but not quadratically) against zero, whereas the generalized material coefficient leads to distinguishable global second order convergence.

4.3.3. Sensitivity Analysis

Up to this point we assume that the field incidence angles α_k are exactly known. As discussed more closely in the following section, this cannot be taken for granted in practical applications without analytically given solutions. Before we introduce methods of estimating the required field information by other means, we utilize the present example to predict the outcome of deviations from the exact angle α_k on the solution's error.

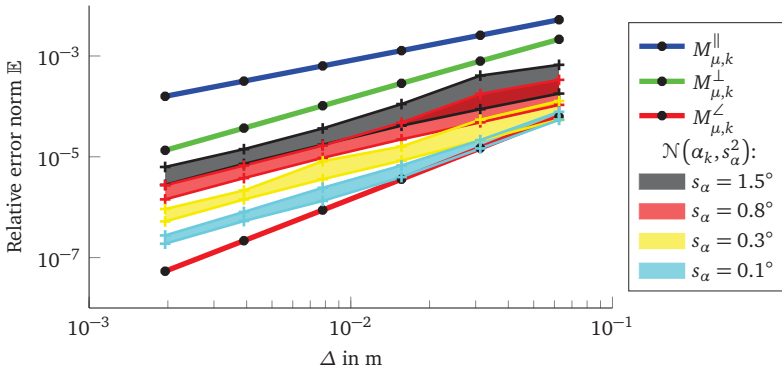


Figure 4.7.: Relative error norm of the discrete vector potential (cf. Fig. 4.6). The colored regions indicate the range of the relative error if the field angles are variates from a normal distribution with given standard deviation s_α .

The uncertainty in the practical determination of the field angles α_k is modeled by taking each of them as samples from a normal distribution $\mathcal{N}(\alpha_k, s_\alpha^2)$. Its arithmetic mean is the respective analytical solution α_k itself. For given standard deviations s_α , the convergence analysis from Section 4.3.2 is performed for 50 random samples per mesh step size taken from the assumed probability distribution.

All of the 50 convergence curves that result per given standard deviation come to lie inside the colored bands in Fig. 4.7. Even though an increasing amount of material coefficients are subjected to uncertainty while refining the mesh, the convergence rate is deteriorated only slightly. This suggests that an approximate

method of obtaining field information can still lead to considerably improved accuracy compared to the conventional approximations. Yet, in order to reliably achieve global second order convergence, the field angles need to be known exactly.

The example is deliberately constructed in a way that causes some occurring field angles α_k to result in material coefficients near the singularity in Fig. 4.3. Due to the large slope in its vicinity, the introduced uncertainty for these specific angles has a disproportionately large, yet still moderate, influence on accuracy. If the example is constructed in a way that excludes the singularity from taking influence, the standard deviations can be chosen larger for comparable results.

It should be noted that the above results apply only for the given example and set of parameters in a quantitative sense. However, further experiments turn out to support the hypothesis that the general predication also applies in other cases, at least qualitatively. Therefore, we now leave the theoretical framework that so far provided us with exactly known field angles and turn towards more practically oriented applications where these angles need to be obtained by other means.

4.4. Estimation of Field Information

Typically, the material matrix \mathbf{M}_μ (or $\mathbf{M}_{\mu^{-1}}$) is set up prior to the solution process. The conventional approximations (4.4) facilitate this strategy by providing formulas that depend only on the computational domain's geometry and material distribution, which are known after the mesh is generated and, most importantly, before the actual solution takes place. If the matrix is supposed to be built in the same way based upon the generalized material coefficient $M_{\mu,k}^\angle$, we would depend on information about the field before we obtain any simulation results. In some sense, this contradicts the principle of electromagnetic field simulation, whose objective it is to determine the field in the first place. In order to apply the concept of generalized material averaging in practical simulations anyhow, we need to take further measures.

The generalized coefficient $M_{\mu,k}^\angle$ is defined in (4.7b) in terms of the interface-continuous field components and, equivalently, in terms of the field incidence angle α_k in (4.7c). Henceforth, we rely on the former definition, which approximates the exact coefficient as follows:

$$M_{\mu,k} = \frac{\widehat{b}_k}{\widehat{h}_k} \approx \frac{A_k}{\widetilde{L}_k} \frac{H_t^a|_{P_k} \cos \theta_k \langle \mu \rangle_{A_k} - B_n^a|_{P_k} \sin \theta_k}{H_t^a|_{P_k} \cos \theta_k - B_n^a|_{P_k} \sin \theta_k \langle \mu^{-1} \rangle_{\widetilde{L}_k}} = M_{\mu,k}^\angle \quad (4.17)$$

As shown in Fig. 4.8, we no longer consider only the flux/voltage-pair k itself, but also the four directly adjacent grid fluxes. They are indexed consecutively by a

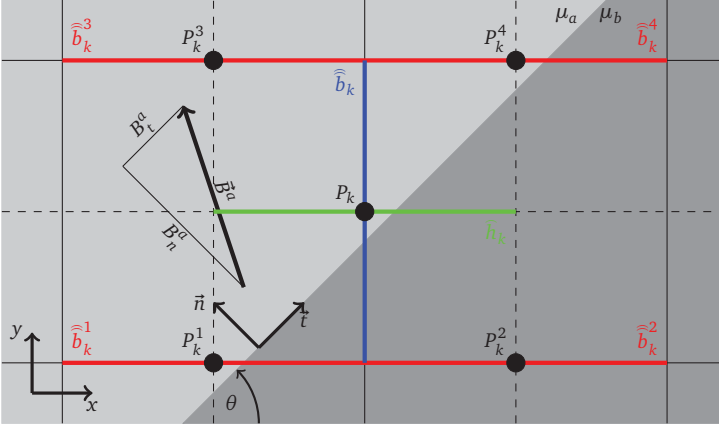


Figure 4.8.: An x -directed pair of grid flux and voltage and its directly adjacent fluxes. The global canonical index is k , while the numeral superscripts are assigned locally.

numeral superscript. For the time being, let us treat all integral state variables as given. Motivated by (4.17), we identify each grid flux with the numerator of the generalized material coefficient they are involved in:

$$\widehat{b}_k = A_k \left(H_t^a \Big|_{P_k} \cos \theta_k \langle \mu \rangle_{A_k} - B_n^a \Big|_{P_k} \sin \theta_k \right) \quad (4.18a)$$

$$\widehat{b}_k^i = A_k^i \left(H_t^a \Big|_{P_k^i} \sin \theta_k^i + B_n^a \Big|_{P_k^i} \cos \theta_k^i \langle \mu^{-1} \rangle_{L_k^i} \right), \quad \forall i \in [1, 4] \quad (4.18b)$$

Since the neighboring facets are all y -directed (cf. Fig. 4.8), they contribute the interface angle's sine instead of its cosine and vice versa. The field components $H_t^a \Big|_{P_k}$ and $B_n^a \Big|_{P_k}$, which are those of interest, occur only in (4.18a). This single equation, however, does not define them uniquely. As a remedy, we assume that their value does not change significantly across the area covered by the five introduced intersection points. This assumption is legitimate because of the involved components' continuity. Furthermore, the local interface angles are considered as equal ($\theta_k^i \approx \theta_k$), which implies a smooth interface contour. Based on these assumptions, we obtain four further equations that contain the sought for quantities from (4.18b):

$$\widehat{b}_k^i = A_k^i \left(H_t^a \Big|_{P_k} \sin \theta_k + B_n^a \Big|_{P_k} \cos \theta_k \langle \mu^{-1} \rangle_{L_k^i} \right), \quad \forall i \in [1, 4] \quad (4.19)$$

Each possible combination of (4.18a) with any equation from (4.19) leads to a regular¹¹ 2×2 system of equations:

$$\begin{bmatrix} \widehat{b}_k/A_k \\ \widehat{b}_k^i/A_k^i \end{bmatrix} = \underbrace{\begin{bmatrix} \cos \theta_k \langle \mu \rangle_{A_k} & -\sin \theta_k \\ \sin \theta_k \langle \mu \rangle_{A_k^i} & \cos \theta_k \end{bmatrix}}_{\Theta_{k,i}} \begin{bmatrix} H_t^a|_{P_k} \\ B_n^a|_{P_k} \end{bmatrix}, \quad \forall i \in [1, 4] \quad (4.20)$$

With regard to an efficient practical implementation at a later point, it is advisable to explicitly invert the system matrices $\Theta_{k,i}$. Which system yields the most accurate results is hard to predict in general. It turns out to be a good compromise to take all of them into account and effectively use their arithmetic mean.

So far we are able to estimate the field information that is required to evaluate the generalized material coefficients $M_{\mu,k}^\angle$ from a given set of adjacent grid fluxes. Note that several assumptions and simplifications have taken place in order to obtain this information. In particular, both the field across the interface, as well as the interface itself have to be reasonably smooth in the mesh cell limit in order to achieve accurate results.

A vital point that has remained unaddressed so far is how to obtain the grid fluxes \widehat{b}_k^i in the first place. For that purpose we suggest two different approaches that are outlined in the following sections and compared against each other by means of the previously used numerical example with given reference solution.

4.4.1. Iterative Approach

If no simulation result or a priori knowledge of the fields is available, we initially make a guess or, preferably, a justified choice that directly leads to one of the conventional coefficients. Whether the formula for the perpendicular case (4.4b) or the parallel case (4.4a) is expected to yield more accurate results can be estimated based on considerations that are outlined in [Sch05; CBS12]. Briefly summarized, if the field is expected to be predominantly normal with respect to the interface, $M_{\mu,k}^\parallel$ is likely to offer better accuracy. In case of a higher amplitude of tangential components, $M_{\mu,k}^\perp$ should be chosen. This can also be inferred from (4.8), according to which the following sets of initial values lead to the desired coefficients:

$$\left\{ B_n^a|_{P_k} = 0, \quad H_t^a|_{P_k} \text{ arbitrary} \right\} \implies M_{\mu,k}^\angle = M_{\mu,k}^\parallel \quad (4.21a)$$

$$\left\{ H_t^a|_{P_k} = 0, \quad B_n^a|_{P_k} \text{ arbitrary} \right\} \implies M_{\mu,k}^\angle = M_{\mu,k}^\perp \quad (4.21b)$$

¹¹Except for very rare special cases.

After solving the problem at hand based on initial choices for $H_t^a|_{P_k}$ and $B_n^a|_{P_k}$, we extract more reliable values for any affected index k from the solution by means of the estimation method from Section 4.4. As visualized in Fig. 4.9, the process is repeated until the variation of the solution's vector norm drops below an adequately defined threshold.

From a mathematical point of view, this corresponds to a fixed-point iteration¹² $\hat{\mathbf{a}}_{z, v+1} = f(\hat{\mathbf{a}}_{z, v})$, where f is a chain of generally nonlinear functions that comprises

- solving for $\hat{\mathbf{a}}_z$,
- obtaining $\hat{\mathbf{b}}$ from $\hat{\mathbf{a}}_z$,
- extracting the required fields $H_t^a|_{P_k}$ and $B_n^a|_{P_k}$ from $\hat{\mathbf{b}}$,
- setting up the material matrix \mathbf{M}_μ^{-1} based on $M_{\mu, k}^\angle$.

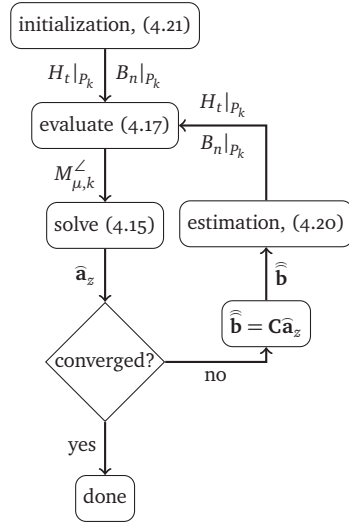


Figure 4.9.: Flow chart of the iterative approach.

Due to the complex and not closed-form structure of f , the guaranteed existence of fixed points and the fixed-point iteration's convergence towards one of them can not be formally ensured. Nevertheless, various numerical experiments suggest that high accuracy and up to second order convergence is reliably achievable for start values, which result from one of the conventional material coefficients.

Fig. 4.10 shows the results of the numerical example from Section 4.3 in the context of the iterative fixed-point approach. Starting from the conventional coefficient in the parallel case¹³, each iteration gradually improves the results. Ultimately, the accuracy and convergence rate are only slightly worse than in case of exactly known field information. This behavior directly corresponds to the results of the sensitivity analysis in Section 4.3.3 and can be explained by the fact that

¹²A thorough introduction to the solution of nonlinear, multi-dimensional problems by means of fixed-point iterations can be found in [RT06].

¹³According to Fig. 4.6 and in correspondence to the reasoning of [Scho5; CBS12], the perpendicular case would have been suited even better. To stress the iterative scheme's robustness, the worse of both alternatives is chosen.

a small degree of uncertainty is introduced by the suggested estimation method. Otherwise, we would expect the iterative approach to converge against the method which is based on exact values (red line in Fig. 4.10). The final result is the same as if the conventional coefficient in the perpendicular case were used initially.

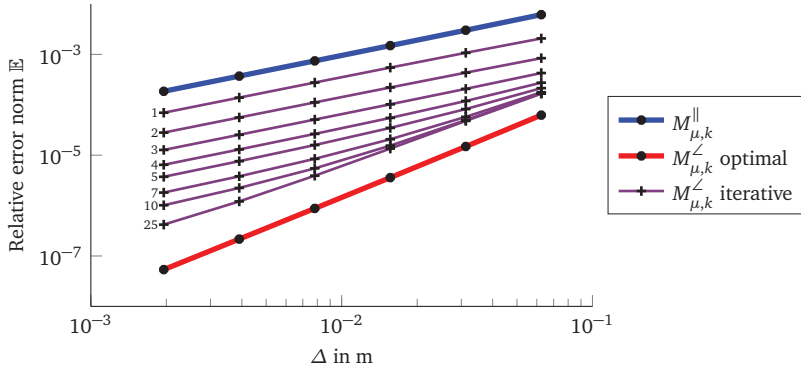


Figure 4.10.: Relative error norm of the discrete vector potential (cf. Fig. 4.6). The respective iteration number ν is given at the left of each graph. Notice the omission of some iterations' visualization for better visibility.

Since fixed-point iterations are known to converge only linearly with the number of iterations [RT06] and, therefore, require numerous iteration in order to reach a certain residual, other means of solving this nonlinear system of equations deserve to find consideration. *Newton's method* offers faster convergence up to second order [RT06]. However, it usually requires a closed form representation of the system function in order to obtain the Jacobian matrix. If the Jacobian is approximated by means of finite differences, the method is called a *Quasi-Newton method*. Even though it thereby becomes evaluable in the present case, the associated computational effort, especially for large problems, is very high. Nevertheless, we manage to achieve comparably accurate results like after 25 fixed-point iterations in only four iterations of a Quasi-Newton method¹⁴, but the fixed-point iteration approach is still significantly faster. *Broyden's method* [Bro65] is supposed to overcome the disadvantage of a Jacobian that is expensive to compute in every iteration by updating it along with the solution vector. However, it did not converge towards the desired solution in our experience.

¹⁴Specifically, we use the MINPACK [MGH80] routine `hybrd` in a MATLAB [Mat14] implementation provided by the free optimization toolbox OPTI [CW12; Cur15].

In order to speed up the solution by means of the described fixed-point iteration, it is advisable to take the previous iteration's solution vector as initial guess for the next pass in case an iterative solver is used. Under this circumstance, it is also advantageous to use a preconditioning matrix. Since the system matrix changes only slightly during the iteration process, it suffices to compute it only once and use it in each pass.

Fig. 4.10 suggests that there are two possibilities to increase the simulation's accuracy. The classical method is the mesh refinement approach. By means of the presented scheme based on the generalized material coefficient, we are able to keep the mesh resolution constant and still yield higher accuracy at the expense of some fixed-point iterations. The question at hand is, which possibility is more efficient. A generally valid answer to that question can not be given, because not even ideal conditions (red line) can guarantee any desired residual to be reached. However, under reasonable requirements, the iterative approach usually turns out to be much faster. In the present example, it takes about 30 s^{15} to solve the problem based on $M_{\mu,k}^{\parallel}$ and the finest mesh resolution. Conversely, 25 fixed-point iterations on the coarsest mesh, which result in an even higher accuracy, are finished after about a second.

A more realistic application in the magnetoquasistatic time domain that takes systematic advantage of the method's iterative nature is demonstrated in Section 5.2. Its deployment in the context of FDTD, where the field information is extracted from fields that are available from the previous time step, has always led to unstable schemes in our experience. This issue is addressed more closely in Section 4.5.1.4.

We successfully used a variation of the iterative scheme to find accurate eigen-solutions of the time harmonic wave equation [Wei85]. The resonance frequencies' convergence behavior is very similar to the results shown in Fig. 4.10. However, each resonance frequency corresponds to a unique field distribution. If several eigenmodes are of interest, the field estimation needs to be performed for each of them individually, which increases the computational effort.

4.4.2. Nondiagonal Matrix Approach

In the first part of Section 4.4, we establish an approximate relation between the field information of interest and a set of grid fluxes that are allocated adjacently to the location of the current material coefficient $M_{\mu,k}$. Specifically, there are four systems of equations (cf. (4.20)) that lead to possible values of $H_t^a|_{P_k}$ and $B_n^a|_{P_k}$, and whose mean value is subsequently taken. We now postpone this averaging

¹⁵Measured on an Intel Core i7-4770K CPU, 16 GB RAM, MATLAB R2014b.

and instead formulate a similar equation for the magnetic grid voltage \widehat{h}_k . The deduction is carried out in complete analogy to that of (4.20), only this time the denominator of (4.17) is utilized. Put in a matrix-vector formulation it reads:

$$\widehat{h}_k / \widetilde{L}_k = \underbrace{\begin{bmatrix} \cos \theta_k & -\sin \theta_k \langle \mu^{-1} \rangle_{\widetilde{L}_k} \end{bmatrix}}_{\Xi_k} \begin{bmatrix} H_{\tau}^a |_{P_k} \\ B_{\eta}^a |_{P_k} \end{bmatrix} \quad (4.22)$$

If we now invert each system of equations from (4.20) and insert it separately into (4.22), we obtain four explicit relations between the voltage \widehat{h}_k , its corresponding flux \widehat{b}_k and one of the neighboring fluxes \widehat{b}_k^i :

$$\widehat{h}_k = \widetilde{L}_k \Xi_k \Theta_{k,i}^{-1} \begin{bmatrix} \widehat{b}_k / A_k \\ \widehat{b}_k^i / A_k^i \end{bmatrix}, \quad \forall i \in [1, 4] \quad (4.23a)$$

$$= \underbrace{\frac{\widetilde{L}_k}{\det \Theta_{k,i}} \begin{bmatrix} \cos^2 \theta_k + \sin^2 \theta_k \langle \mu^{-1} \rangle_{\widetilde{L}_k} \langle \mu \rangle_{A_k^i} \\ \sin \theta_k \cos \theta_k \left(1 - \langle \mu^{-1} \rangle_{\widetilde{L}_k} \langle \mu \rangle_{A_k} \right) \end{bmatrix}^T}_{\mathbf{M}_{\mu^{-1},k,i}} \begin{bmatrix} \frac{1}{A_k} & 0 \\ 0 & \frac{1}{A_k^i} \end{bmatrix} \begin{bmatrix} \widehat{b}_k \\ \widehat{b}_k^i \end{bmatrix} \quad (4.23b)$$

The last reformulation follows from explicitly writing out the inverse $\Theta_{k,i}^{-1}$ and carrying out the matrix product $\Xi_k \Theta_{k,i}^{-1}$. The resulting 1×2 matrix that transforms grid fluxes into voltages can be understood as a local inverse material matrix $\mathbf{M}_{\mu^{-1},k,i}$. The fact that the x -directed voltage \widehat{h}_k does not only depend on its corresponding flux \widehat{b}_k , but also on a total of four of its y -directed neighbors implies off-diagonal elements in the global material matrix $\mathbf{M}_{\mu^{-1}}$. For each row index k , the off-diagonal elements' values are taken from the second column of the matrix $\mathbf{M}_{\mu^{-1},k,i}$, $\forall i \in [1, 4]$. The column indices equal the canonic indices of \widehat{b}_k 's neighbors. Also, there are four contributions to each affected main diagonal element k (first column of $\mathbf{M}_{\mu^{-1},k,i}$), which we incorporate by means of their arithmetic average, just like in the iterative approach.

It is worth noting that (4.23b), despite the introduced approximations, still contains the (inverse) conventional material coefficients $M_{\mu,k}^{\parallel}$ and $M_{\mu,k}^{\perp}$ for $\theta_k = \pi/2$ or $\theta_k = 0$, respectively. The second element of $\mathbf{M}_{\mu^{-1},k,i}$ is always zero in any of these cases, thus eliminating off-diagonal matrix components of $\mathbf{M}_{\mu^{-1}}$. The first element contributes only the appropriate averaging operator $\langle \mu^{-1} \rangle_{\widetilde{L}_k}$ or $\langle \mu \rangle_{A_k}$ and the respective facet's and edge's area and length. All remaining terms cancel out.

The above deduction aims at directly obtaining the inverse matrix for the sake of employment in (4.15). For other purposes, where the noninverted matrix \mathbf{M}_{μ} is

required, the deduction should be adapted accordingly in order to avoid the need to explicitly invert a nondiagonal matrix. Opposed to the case of diagonal material matrices build upon the conventional coefficients $M_{\mu,k}^{\parallel}$ and $M_{\mu,k}^{\perp}$, we now face the inequality $\mathbf{M}_{\mu}^{-1} \neq \mathbf{M}_{\mu-1}$.

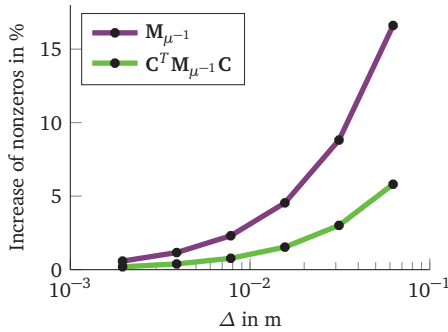
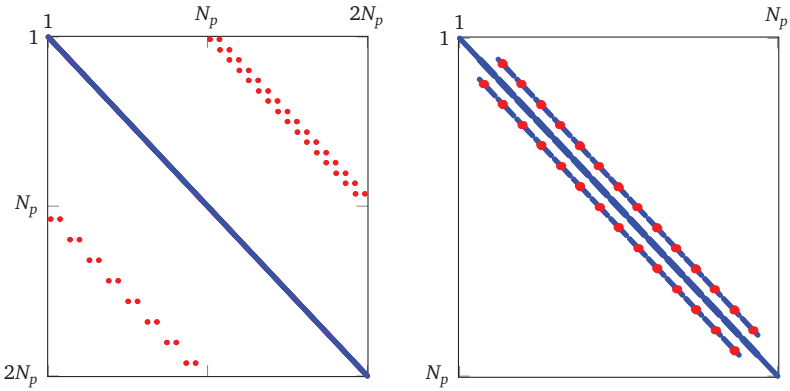
A question that arises due to its nondiagonality is whether or not it is symmetric. Each local matrix $\mathbf{M}_{\mu-1,k,i}$ invokes the neighboring mesh flux \widehat{b}_k^i . Symmetry would imply that the local matrix for this neighboring flux invoked \widehat{b}_k in exactly the same way. Apparently, this is not the case since the neighboring pair of voltage and flux needs not necessarily be cut by the material interface.

Similar to the iterative approach from the previous Section 4.4.1, the nondiagonal matrix approach enables a comparably accurate solution to be obtained much faster than by means of a mesh refinement. The main difference is the abandonment of several solution passes at the expense of a nondiagonal material matrix. Since the matrix structure for the iterative approach is exactly preserved in comparison to the conventional case, we can assume that virtually no access computer memory is required. The nondiagonal matrix, on the other hand, requires additional storage capacity that shall be assessed more closely in the following. Therefore, we visualize the matrices $\mathbf{M}_{\mu-1}$ and $\mathbf{C}^T \mathbf{M}_{\mu-1} \mathbf{C}$ for the given example and study their nonzero entries' increase in dependence of the mesh resolution Δ in Fig. 4.11.

For the coarsest investigated mesh resolution, the sparsity pattern of $\mathbf{M}_{\mu-1}$ in Fig. 4.11a clearly shows the nondiagonal, and furthermore unsymmetric, matrix structure. Fig. 4.11b highlights those elements of $\mathbf{C}^T \mathbf{M}_{\mu-1} \mathbf{C}$ that would not exist if $\mathbf{M}_{\mu-1}$ were diagonal. Apparently, the increase in storage requirements for the system matrix is relatively moderate. This observation is confirmed by Fig. 4.11c, which compares the growth of nonzero matrix entries in dependence of the mesh resolution. It states that for meshes, where a lot of nonconformal material-mesh intersections occur, the nondiagonal approach can be noticeably more demanding than the iterative one. However, if only a small percentage of edge-facet pairs face a nonconformal interface, which is usually the case on highly resolved meshes, the extra storage effort is negligible. Nevertheless, one has to keep in mind that the system matrix becomes unsymmetric, thus imposing generally negative implications in terms of an iterative solver's convergence speed.

4.4.2.1. Comparison to Existing Subpixel Smoothing Schemes

The notion of introducing nondiagonal material matrices in order to accurately handle nonconformal interfaces is actively pursued for over a decade, predominantly in the optics and photonics community. In 2006, Farjadpour et al. [Far+06] propose



(c) Relative increase of nonzero matrix entries due to the nondiagonal approach.

Figure 4.11.: Visualization of the nondiagonal material matrix $\mathbf{M}_{\mu-1}$, the corresponding system matrix $\mathbf{C}^T \mathbf{M}_{\mu-1} \mathbf{C}$ and the relative growth of nonzero matrix components with respect to the iterative approach.

a technique for finding an effective anisotropic medium that acts as a replacement for cut mesh cells. This paper coins the phrase *subpixel smoothing*, which has become a common name for methods that deal with partially filled mesh cells. The implementation of Farjadpour's tensor material in time domain turns out to be unstable [WCo7] and, furthermore, fails to consistently achieve second order accuracy in frequency domain [WCo7]. Werner and Cary introduce a method to obtain symmetric material matrices from anisotropic media that leads to numerically stable update schemes [WCo7]. This method is implemented in the free FDTD simulation software *Meep* [OKJ09; Osk+10].

Specifically in conjunction with an anisotropic effective medium from the subpixel smoothing theory, Shyroki also investigates and compares ways of inferring material matrices [Shy11]. His numerical experiments in frequency domain lead to the unproved conjecture that second order accuracy can only be achieved by sacrificing the symmetry of material matrices. The same perception is made by Werner, Bauer and Cary in [WBC13], where the authors try to symmetrize a nonsymmetric, highly accurate approach published by themselves in 2011 [BWC11].

The last-mentioned approach [BWC11] turns out to be very similar to the nondiagonal matrix approach presented herein. The key in both methods' deduction is their intermediate introduction of interface-continuous field components (here $H_t^a|_{p_k}$ and $B_n^a|_{p_k}$), which are subsequently expressed in terms of grid voltages and fluxes. In fact, both algorithms perform comparably well in practice (disregarding FDTD due to instability). A major difference, however, is the way the inverse material matrix $\mathbf{M}_{\mu-1}$ is constructed. The present method introduces off-diagonal matrix elements in all rows k , for which \tilde{L}_k or A_k are cut by a material interface. Bauer et al. also introduce off-diagonal elements in those rows that belong to directly adjacent mesh items, even if they are not cut. In our experiments the sparse matrix $\mathbf{M}_{\mu-1}$ holds three to five times more nonzero entries, thus imposing much higher requirements on system resources.

A comparison with regard to accuracy and convergence rate of the nondiagonal matrix approach to the one from Bauer et al., as well as to all other methods introduced in this chapter is given in Fig. 4.12 in the following, summarizing section.

4.5. Summary and Concluding Remarks

The generalized material coefficient $M_{\mu,k}^{\angle}$, that is the foundation of this chapter, in theory prevents the second order convergence rate of the Finite Integration Technique from being deteriorated, even if nonconformal material interfaces are

present in the computational domain. In this context, the term conformal refers to one of the cases, in which the conventional coefficients $M_{\mu,k}^{\parallel}$ or $M_{\mu,k}^{\perp}$, which are included as special cases, lead to the same second order convergence rate. We have demonstrated this by means of a numerical example with analytically known reference solution in Section 4.3.2.

In order to apply the generalized coefficient in practically relevant simulations, where no a priori field information is available, we suggest two different methods. The first one (Section 4.4.1) iteratively incorporates the material coefficient by solving the problem at hand several times. The second one (Section 4.4.2) invokes the generalized averaging formula implicitly, which leads to a nondiagonal material matrix. An existing approach [BWC11] is consulted for comparison.

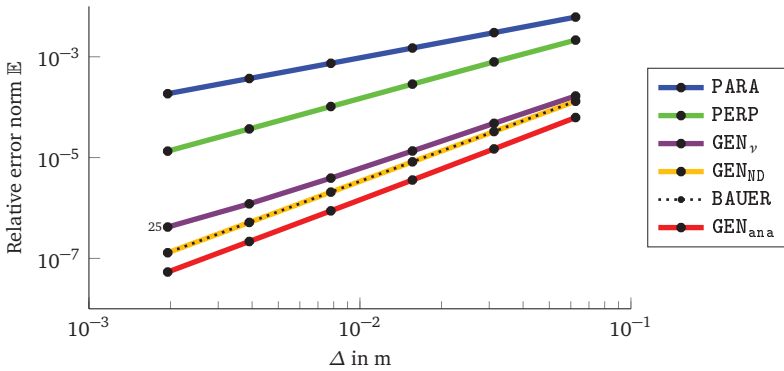


Figure 4.12.: Relative error norm of the discrete vector potential for all discussed approximations to the ideal material coefficient $M_{\mu,k} = \widehat{b}_k / \widehat{h}_k$.

For clear concision, we introduce the following abbreviations for each different method:

PARA	The conventional coefficient assuming . . .
PERP	a parallel interface, (4.4a).
PERP	a perpendicular interface, (4.4b).
GEN _{ana}	The generalized coefficient based on fields obtained from . . .
GEN _ν	the analytical solution, (4.7c).
GEN _{ND}	the iterative approach, Fig. 4.9.
BAUER	the nondiagonal matrix approach, (4.23b).
BAUER	A nondiagonal matrix approach from the literature, [BWC11].

Fig. 4.12 compares all essential results discussed so far against each other. If the generalized coefficient is evaluated based on field information taken from the analytical solution (GEN_{ana}), distinct second order convergence with drastically lower error than in the conventional approaches is noticeable. By means of the proposed field estimation methods we manage to achieve similar levels of accuracy and, furthermore, convergence rate, even in the absence of exploitable a priori knowledge.

The nondiagonal matrix approach GEN_{ND} is qualitatively indiscernible from BAUER. However, due to a much larger number of matrix entries it takes approximately 1.4 times longer to obtain its results. The iterative approach GEN_v performs slightly worse in terms of accuracy, but still drastically better than the conventional approaches PARA or PERP. This degradation results from the fact that less quantities, and therefore less information about cut ratios, are taken into account in GEN_v 's deduction. Specifically, five magnetic fluxes are used per affected index k , while GEN_{ND} resorts additionally to \hat{h}_k .

Even though the nondiagonal matrix consists of more elements and has less favorable properties with regard to its invertibility than in the iterative approach, the resulting algorithm is typically faster because it suffices to solve only once, whereas the iterative approach requires several solution runs. How many iterations are actually necessary strongly depends on the application and requirements regarding accuracy. As seen in Fig.4.10, already very few passes suffice for a distinct improvement.

The curves' progressions are in accordance with the sensitivity analysis carried out in Section 4.3.3, which confirms that both estimation methods are not able to determine the required field information exactly, but with reasonably low deviation.

Summarizing this chapter, we have shown that the generalized material coefficient provides means to significantly increase the FIT's accuracy in case the mesh is not able to conform to material discontinuities. Its application is competitive and, with regard to efficiency, even superior to existing subpixel smoothing techniques from the literature.

4.5.1. Remarks

Some points have been addressed only briefly so far or do not find detailed consideration. For the sake of completeness and encouragement for further research, they shall be recapitulated in this section.

4.5.1.1. Dielectric or Conductive Materials

The entire chapter is concerned exemplarily with magnetic materials, where the interface separates two media with different permeabilities μ_a and μ_b . Dielectric or conductive materials can be handled in exactly the same way by analogously derived coefficients $M_{\varepsilon,k}^\angle$ or $M_{\sigma,k}^\angle$. The only difference worth mentioning is that the related voltages \widehat{e}_k are defined on primary edges L_k and the respective flux terms \widehat{d}_k and \widehat{j}_k on dual facets \widetilde{A}_k . For reference, the deduction and examples in [Scho5; KCS14a; Kue15] are mainly concerned with dielectric materials.

4.5.1.2. Curved Interfaces

Being exempt from the requirement of strictly parallel or perpendicular material interfaces with respect to the mesh, it seems consequent to also dismiss their requirement on being (piecewise) straight. As shown in Section 4.2, the field information always needs to be evaluated at the intersection points P_k in terms of interface-normal and -tangential components. If the interface is no longer straight, i.e. its direction varies inside the mesh cell limit, it is not clear in what sense the terms *normal* and *tangential* have to be understood. Intuitively, we evaluate \vec{n} and \vec{t} at the point on the interface, which is closest to P_k . By that measure the discussed approaches extend straightforwardly to curved interfaces.

As an interesting side note, the generalized material coefficient can be shown to include a very similar technique for material transitions to perfect conductors as a special case [Scho5]. This approach is initially published in [Rie89] and is also described in [DM98] under the name *Locally-Conformal Technique* and in [Kri+98] as *Perfect Boundary Approximation Technique*. It is furthermore subjected to a profound theoretical analysis in [ZSW03] and, also therein, successfully applied to curved material interfaces.

4.5.1.3. Extension to 3D

Fig. 4.1 gives an impression of the complexity of a 3D mesh, inside of which the material interface has to be understood as a 2D plane. It is therefore and also for a condensed notation that we restrict ourselves to a 2D formulation inside the x - y -plane. The general principle, however, remains completely unaltered if z -dependence is taken into account.

The generalized coefficient has to be supplemented by a term that concerns the additional, linearly independent tangential field component. Alternatively, this can be achieved by a second field angle in the formulation (4.7c). The field estimation

methods presented in Section 4.4 also straightforwardly extend by additionally considering neighboring mesh elements in the z -direction.

A master's thesis that evolved from the present work has closely investigated the generalized material averaging formula for 3D applications [Kue15]. Its conclusion is that the FIT's accuracy can in fact be considerably enhanced, but multiply cut mesh facets and edges are more likely to occur and need to be dealt with adequately.

4.5.1.4. Indefiniteness of Material Matrices

Conventional material averaging, as described in Section 4.1, offers very beneficial numerical properties that are often taken for granted mistakenly. The fact that these conventional coefficients only consist of facet areas, edge lengths and (averaged) material parameters (cf. (4.4)) guarantees each of them to be nonnegative and, consequently, the resulting diagonal matrix to be positive semidefinite. This matrix property may seem to reflect the physical characteristic of positive material parameters ε , μ and σ without considering it in the context of generalized material averaging.

If the matrix is no longer symmetric, like in case of the nondiagonal matrix approach presented in Section 4.4.2, the term positive definiteness is not even defined anymore and numerical stability no longer assurable. Furthermore, we also cannot unconditionally rely on this favorable property in case we deal with diagonal, i.e. symmetric, matrices, which result by obtaining the field information from the iterative approach or an exact reference solution. This can be clearly seen from Fig. 4.3 and Fig. 4.5b, which prove that negative values of the generalized material coefficient are likely to occur¹⁶. Fig. 4.5b furthermore shows that this is no spurious effect, possibly caused by approximations in its deduction, but instead also happens for the ideal material coefficient $M_{\mu,k}$.

Apparently, the effect of positive semidefinite material matrices does not naturally arise from the positivity of physical material parameters alone. It is also influenced by the way the ideal material coefficient is approximated. The results of this chapter, especially the comparison of different approximations in Fig. 4.5, allow for the conclusion that the occurrence of indefinite, or even unsymmetric material matrices can not be ruled out, if the Finite Integration Technique's results are supposed to converge quadratically in case of nonconformal material interfaces. This observation is backed by [Shy11]'s and [BWC11]'s results, which are also mentioned in Section 4.4.2.

¹⁶In fact, all results obtained by means of the generalized coefficient in this chapter are based on indefinite material matrices.

As discussed in Section 2.3.2, positive definiteness is a necessary condition for numerical stability and, thus, convergence of FDTD schemes. We can conclude that for converging FDTD simulations, the material needs to conform with the mesh. Otherwise, it must be modified in order to do so, with significant loss of accuracy and convergence rate. By that result, the effort put in the advancement of time domain methods on cylindrical meshes in Chapter 3 becomes even more justified, because it enables circular structures to conform with a computational mesh without geometrical modifications.

The iterative scheme presented in Section 4.4.1 provides us with the ability to easily check material matrices with regard to positive definiteness, since they are always diagonal by design. As indicated in [KKS16], it may turn out beneficial to exploit this ability and replace all matrix coefficients that cause undesired numerical properties with more favorable ones. Possibilities include any of the conventional coefficients or weighted averages thereof. We do not pursue this approach in the present work because we cannot guarantee a consistently positive impact on simulation results. Further research on suitable scenarios of this technique and meaningful ways of application is required.

Practice-Oriented Applications

So far, the suggested methods from Chapters 3 and 4 are only applied to abstract examples with analytically known reference solutions. This chapter's aim is to demonstrate their use in more involved cases that are motivated by practically relevant structures. However, the focus shall not lie on a realistic reproduction of results from the literature or measurements, but rather on the comparison between the proposed approaches with other simulation techniques. Therefore, we idealize the simulated structures strongly and neglect some properties that would otherwise make it very hard to yield meaningful conclusions. These simplifications are discussed in detail in the respective sections.

While all algorithms that are introduced in this work are implemented in Mathworks MATLAB R2014b [Mat14], we also use the commercial simulation software CST Studio Suite 2015 [CST15] for comparison's sake. It offers many highly evolved and optimized simulation techniques for various applications. For that reason, it is not instructive to compete against it in terms of execution speed. Instead, we establish scenarios in which the CST Studio Suite works under similar circumstances and evaluate all results with respect to reference solutions. They are also obtained by the CST Studio Suite, but under exploitation of its full potential.

5.1. FDTD on Cylindrical Meshes

The Coupled Multi-Mode method MM3D (cf. Section 3.2.1) and the combined Hybrid Newmark-Beta approach HNB3D (cf. Section 3.2.2) are applied in the following sections to deduce the frequency spectra and resonant modes of two optical devices in the micrometer range. Besides some geometrical idealizations that make them fit perfectly to a cylindrical mesh, we treat them only in 2D inside a ϱ - φ -plane.

Another simplification is the termination of the computational domain with electric boundary conditions. In order to accurately reproduce the behavior of such devices in free space, the use of an absorbing boundary condition is advisable. Most commonly in FDTD simulations, it is realized by means of a so called *Perfectly Matched Layer (PML)* [Bér94; TC00]. Its implementation for cylindrical meshes in the Finite Integration Technique is discussed by the author in [Kir10]. However, its sophisticated deployment makes a direct comparison with results obtained from the CST Studio Suite on Cartesian meshes unfeasible. Electric boundaries, on the

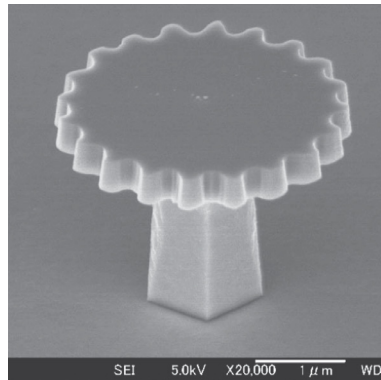
other hand, can be modeled comparably well. In the cylindrical examples, they are realized by an electric boundary condition, while the Cartesian meshes in the CST Studio Suite are terminated by circular PEC walls under employment of the Perfect Boundary Approximation technique [Rie89; Kri+98; DM98].

The following sections' investigations are already published in similar form by the author in [KS12a] and [KS13d], respectively. They comprise different setups and are based on tentative versions of the methods presented in this thesis. Opposed to the setups presented herein, they involve absorbing boundaries but lack the comparison to FDTD on Cartesian meshes and to a reference solution. One of them is restated in Appendix D.

5.1.1. Microgear Resonator

This section deals with a so called *microgear cavity* (cf. Fig. 5.1). This structure is proposed and investigated in [FB01] and [FB02] with the purpose to eliminate non-lasing modes from microcavity lasers' spectra. The characteristic grating at the dielectric structure's perimeter is supposed to selectively privilege a specific *whispering-gallery mode* [Orao2], whose azimuthal order directly corresponds to the number of cogs.

An idealized model of the microgear cavity provides a well-suited application example for the Coupled Multi-Mode approach MM3D (cf. Section 3.2.1), due to the structure's high degree of symmetry, specifically its perfect rotational symmetry up to a certain radius. For the sake of demonstration and meaningful comparison, we restrict ourselves to the actual resonator structure without its pedestal and align the grating with only 8 cogs along a cylindrical coordinate system.



Reproduced from [FB02] (M. Fujita and T. Baba. "Microgear Laser". In: *Applied Physics Letters* 80.12 (2002), pp. 2051–2053, <http://dx.doi.org/10.1063/1.1462867>), with the permission of AIP Publishing.

Figure 5.1.: Scanning electron micrograph of a microgear cavity.

As discussed above, it is placed inside a perfectly conducting, circular box instead of terminating the computational domain with absorbing boundary conditions.

The mesh configuration for MM3D is shown in Fig. 5.2a. The Multi-Mode domain covers nearly the entire rotationally symmetric part. Only the cogs and the surrounding free space are discretized by a conventional cylindrical mesh. The perfectly conducting enclosure is implemented by an electric boundary condition (cf. Section 2.2.3).

To stress the advantages of the coupled approach (MM3D), we compare its results to a highly accurate reference solution (FEM_{CST}^{ref}). It is obtained by an eigenmode calculation on a dense tetrahedral mesh in CST Microwave Studio. We also compare the results to those of a fully cylindrical approach ($FDTD_{cy1}$) on an otherwise equal mesh and, furthermore, to a Cartesian FDTD approach on a comparably coarse mesh. This Cartesian mesh is shown in Fig. 5.2b. The simulation is carried out in the CST Studio Suite under the premises described in the previous section. In order to deal with the nonconformal material interfaces, an advanced, but undisclosed¹ treatment of partially filled mesh cells ($FDTD_{CST}$), as well as the straightforward staircase technique ($FDTD_{CST}^{SC}$) come to action.

The simulation and evaluation process is based on that described for the numerical example in Section 3.2.4. We excite the given structure symmetrically by imprinting a z -directed current in its center. Its frequency spectrum covers the range from 90–110 THz. During the simulation, which runs 30 times the duration of the excitation signal, a probe signal of the z -directed electric field is recorded inside one of the cogs. For each respective approach, its Fourier spectra are given in Fig. 5.3.

The single resonance frequency inside the excited spectrum is determined distinctively and in reasonably good correspondence to its reference solution FEM_{CST}^{ref} for each respective method. Fig. 5.2c gives a visual representation of this mode's electric field. It is obtained during the simulation by an on-the-fly calculation of the discrete Fourier transform at each z -directed mesh edge. The mode is well-confined inside the cavity and also aligned with respect to the cogs.

In the following, we assess the simulation approaches quantitatively with regard to accuracy and simulation time, if applicable. Therefore, we subject each of the temporal probe signals to harmonic inversion [MT98] by means of the free software Harminv [Joho6]. The resulting resonance frequencies for the mode shown in Fig. 5.2c are then compared to the reference solution from FEM_{CST}^{ref} . This leads to the relative errors given in Table 5.1.

As expected from the results of Section 3.2.1, MM3D leads to the most accurate results. Under consideration of the findings of Chapter 4, it is also evident that the

¹It is titled *FPBA with Enhanced Accuracy* in the CST Studio Suite.

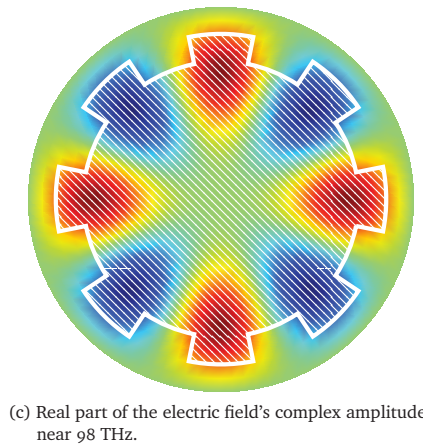
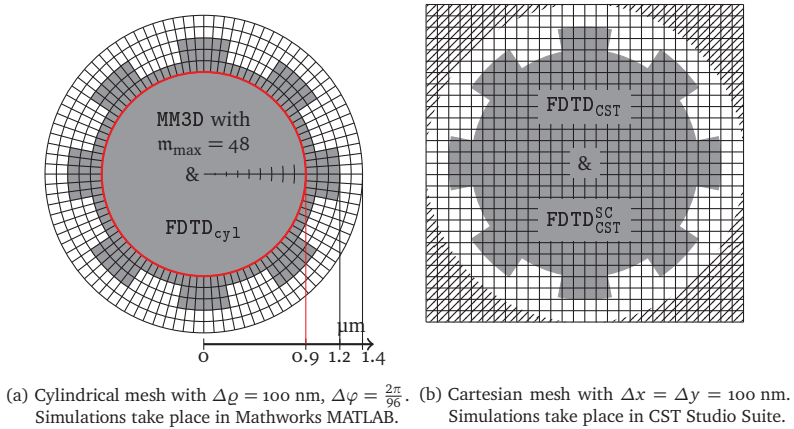


Figure 5.2.: True to scale computational setup and mode pattern of the investigated microgear resonator. The dielectric medium has the permittivity $8\epsilon_0$.

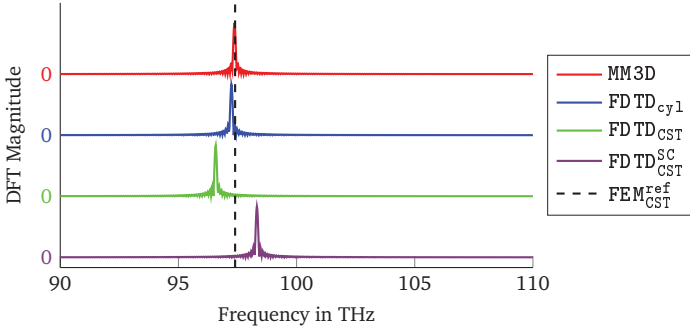


Figure 5.3.: Normalized Fourier spectra of the recorded probe signals for each different approach. The dashed line represents a highly accurate eigenmode solution from the CST Studio Suite.

MM3D	FDTD _{cyl}	FDTD _{CST}	FDTD _{CST} ^{SC}
0.03 %	0.16 %	0.84 %	0.95 %

Table 5.1.: Relative error of the resonance frequency for the mode shown in Fig. 5.2c, compared to the reference solution from FEM_{CST}^{ref}.

Cartesian mesh in FDTD_{CST}^{SC} performs worse due to nonconformal material interfaces (cf. Fig. 5.2b). Even FDTD_{CST}'s special treatment for partially filled mesh cells cannot compete with the cylindrical algorithms' accuracy.

The generalized material coefficient from Chapter 4 does not find consideration at this point, because of the microgear cavity's involved geometry and the associated complexity of the coefficients' evaluation. Furthermore, it is shown to lead to unstable FDTD schemes (cf. Section 4.5.1.4).

Despite MM3D's improved accuracy, it also performs noticeably faster than FDTD_{cyl}. This is made possible by the automated mode selection (cf. Section 3.2.1.3), which disables all negligible azimuthal modes m and, consequently, drastically increases the employable time step size. In this example, we set the threshold for disabling an azimuthal mode to a modal energy \mathcal{E}_m that is lower than 10^{-5} times the total energy in the BOR domain. Fig. 5.4 shows each modal energy in relation to the total energy. Due to the microgear's grating structure, only those azimuthal modes that stand in an integer relation to the resonator's number of cogs are excited in the first place. Amongst all azimuthal modes that are in fact excited, the automated mode

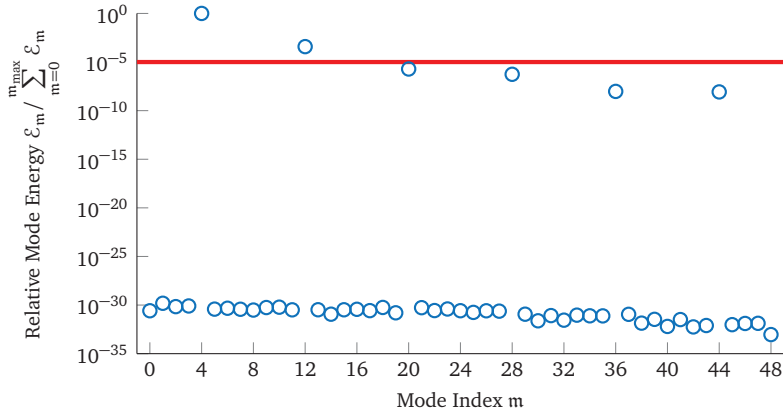
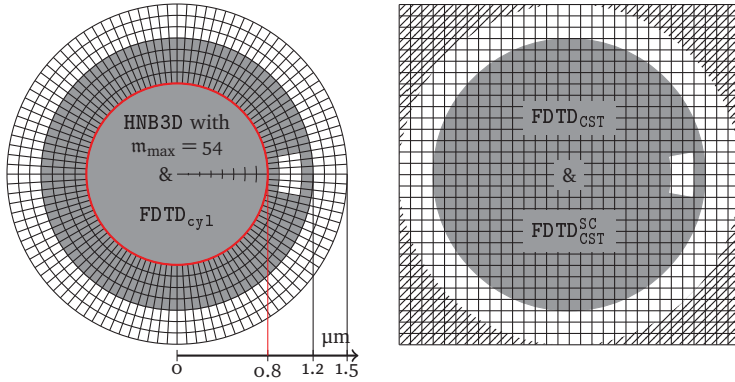


Figure 5.4.: Energy per azimuthal mode according to (3.11). Notice the close connection between the microgear resonator’s number of cogs (eight), and the relevant azimuthal modes.

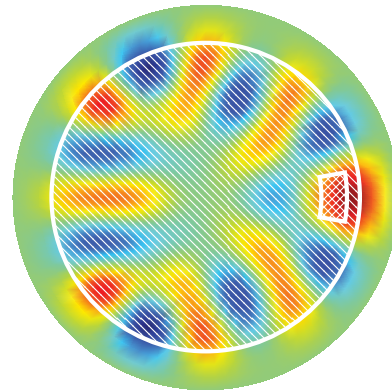
selection disables those with $m \geq 20$ and, additionally, all further azimuthal modes that are not excited. Consequently, the time step size increases from $6.94 \cdot 10^{-18}$ s to $2.76 \cdot 10^{-17}$ s, i.e. by about four times. In terms of measured execution times for the entire time loop, this leads to a speedup of 2.3. The Cartesian mesh dictates a time step size of $6.27 \cdot 10^{-17}$ s. Due to this advantage, and also due to their highly optimized implementation, FDTD_{CST} and $\text{FDTD}_{\text{CST}}^{\text{SC}}$ clearly outperform the cylindrical algorithms. However, we expect them to be similarly fast in consistent implementation frameworks, because MM3D works on a reduced set of degrees of freedom after disabling unnecessary azimuthal modes.

5.1.2. Pierced Microdisk

If a microdisk is not bordered by a grating structure, like in the previous application example of a microgear resonator, its modes are less confined and undirected radiation takes place across its boundary. In case this radiation is supposed to take place predominantly along a predefined direction, the disk’s perfect rotational symmetry needs to be disturbed. A possibility to realize such a directed radiation pattern is to manufacture the disk with a piercing in its outer perimeter. These so called *pierced microdisks* are investigated thoroughly in [Wilo8; Ban11].



(a) Cylindrical mesh with $\Delta\varrho = 100$ nm, $\Delta\varphi = \frac{2\pi}{108}$. Simulations take place in Mathworks MATLAB.
 (b) Cartesian mesh with $\Delta x = \Delta y = 100$ nm. Simulations take place in CST Studio Suite.



(c) Real part of the electric field's complex amplitude near 158 THz.

Figure 5.5.: True to scale computational setup and mode pattern of the investigated pierced microdisk. The dielectric medium has the permittivity $8\epsilon_0$.

Because of the strong perturbation of the rotational symmetry by a local piercing, the Coupled Multi-Mode approach MM3D is no longer suited for simulation. A large number of azimuthal modes would be required to accurately describe the occurring fields and the automated mode selection could not enhance the employable time step size significantly. Therefore, we turn towards the Hybrid Newmark-Beta approach with radially adjusted β (cf. Section 3.2.2). Since the inner part of the pierced disk is still rotationally symmetric, as seen in Fig. 5.5, we use the combined approach with a BOR mesh that ranges radially up to the perturbation. Like in Section 3.2.4, we abbreviate this algorithm with HNB3D. The computational mesh setup is shown in Fig. 5.5a. Except for its multi-modal BOR domain it is used unchanged for the conventional cylindrical FDTD approach FDTD_{cy1} .

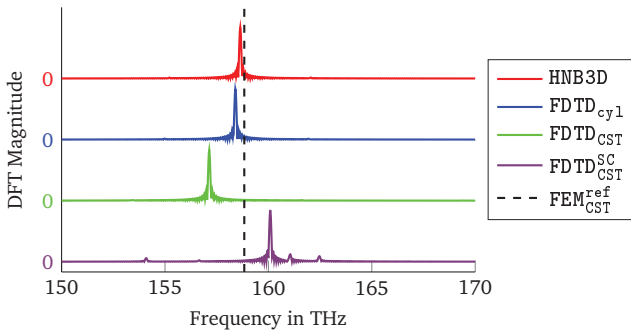


Figure 5.6.: Normalized Fourier spectra of the recorded probe signals for each different approach. The dashed line represents a highly accurate eigenmode solution from the CST Studio Suite.

The remaining simulation process and its setup are oriented on those in the previous section. A mode pattern that clearly constitutes the desired properties is obtained from FDTD_{cy1} and shown in Fig. 5.5c. It occurs at approximately 158 THz and exhibits a distinct orientation of its field pattern with respect to the piercing. Each probe signal that results from the discussed simulation approaches features this mode in its Fourier spectrum. These spectra are given in Fig. 5.6. The respective deviations to the reference solution are qualitatively noticeable and denoted numerically by means of their relative error in Table 5.2. As expected, HNB3D leads to the most accurate results, followed by FDTD_{cy1} . The Cartesian mesh approaches have to deal with partially filled mesh cells and, therefore, cannot compete in terms of accuracy. Even though $\text{FDTD}_{\text{CST}}^{\text{SC}}$ yields a smaller relative error

for this particular mode than FDTD_{CST} , parasitic modes are excited due to the inaccurate representation of the piercing on a staircase mesh.

HNB3D	FDTD_{cy1}	FDTD_{CST}	$\text{FDTD}_{\text{CST}}^{\text{SC}}$
0.12 %	0.27 %	1.07 %	0.79 %

Table 5.2.: Relative error of the resonance frequency for the mode shown in Fig. 5.5c, compared to the reference solution from $\text{FEM}_{\text{CST}}^{\text{ref}}$.

Besides the increase in accuracy, HNB3D yields an overall speedup of 8.0 with respect to FDTD_{cy1} , which can be traced back to the significant enlargement of the time step size from $9.70 \cdot 10^{-18}$ s to $1.35 \cdot 10^{-16}$ s (about 14 times larger). Since the update scheme is completely explicit and the degrees of freedom remain unchanged, we expect the speedup to be even higher if more effort is put into a speed-optimized implementation.

A more realistic version of the pierced microdisk setup is given in Appendix D. It comprises a higher mesh resolution and an absorbing boundary in radial direction.

5.2. Time Domain Magnetoquasistatics with Nonconformal Material Interfaces

This section's topic is the treatment of the structure shown in Fig. 5.7. From a geometrical point of view, it is the same like in the numerical example from Section 4.3. The tilted mesh causes nonconformal material interfaces, which we subject to treatment with the generalized material coefficient $M_{\mu,k}^{\angle}$. However, instead of the magnetostatic case, we now focus on an application based on the time domain formulation of the magnetoquasistatic approximation of Maxwell's equations (abbr. MQSTD). In the context of the Finite Integration Technique, it reads [CW99]:

$$\mathbf{C}^T \mathbf{M}_{\mu-1} \mathbf{C} \mathbf{a}(t) + \mathbf{M}_{\sigma} \frac{d}{dt} \mathbf{a}(t) = \widehat{\mathbf{j}}_s(t) \quad (5.1)$$

Notice the close resemblance to its space-continuous counterpart (2.7), except for the occurrence of source currents $\widehat{\mathbf{j}}_s(t)$. The time dependence can be discretized by means of the Backward Euler² method [CW99], which leads to the following, unconditionally stable iteration scheme:

$$\left(\mathbf{C}^T \mathbf{M}_{\mu-1} \mathbf{C} + \frac{1}{\Delta t} \mathbf{M}_{\sigma} \right) \widehat{\mathbf{a}}^{(m+1)} = \frac{1}{\Delta t} \mathbf{M}_{\sigma} \widehat{\mathbf{a}}^{(m)} + \widehat{\mathbf{j}}_s^{(m+1)} \quad (5.2)$$

²Other discretization methods are feasible as well. However, Backward Euler leads to the simplest update scheme, which is sufficient for the sake of demonstration.

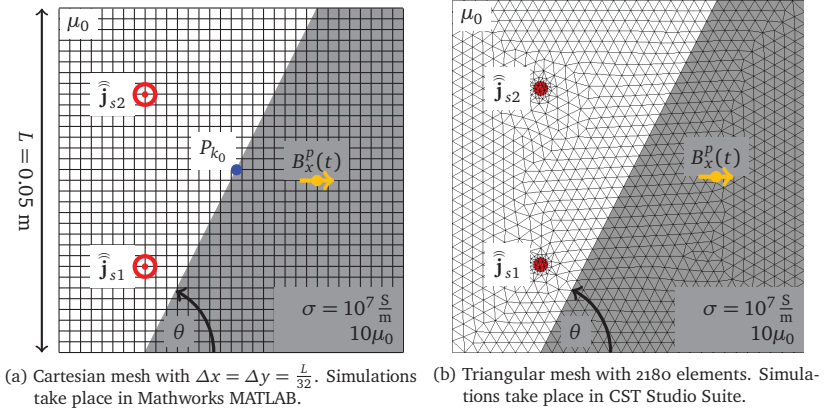


Figure 5.7.: True to scale computational setup of the tilted ($\theta = 63.43^\circ$) material interface.

For details about its derivation and numerical properties, the reader is referred to [CW99; CW01]. As we have already discussed in Section 4.4.1, the generalized material coefficient, as foundation of the matrix $\mathbf{M}_{\mu-1}$, constitutes a nonlinear material relation, which depends on the actual fields. A technique, called the *Successive Approximation Algorithm* [DW00], allows for the incorporation of nonlinear magnetic materials with given magnetization curves into (5.2). For that purpose, the vector potential $\hat{\mathbf{a}}^{(m+1)}$ is reevaluated based on the magnetization curve by means of a fixed-point iteration with index ν in every time step m :

$$\left(\mathbf{C}^T \mathbf{M}_{\mu-1}(\hat{\mathbf{a}}_v^{(m+1)}) \mathbf{C} + \frac{1}{\Delta t} \mathbf{M}_\sigma \right) \hat{\mathbf{a}}_{\nu+1}^{(m+1)} = \frac{1}{\Delta t} \mathbf{M}_\sigma \hat{\mathbf{a}}^{(m)} + \hat{\mathbf{j}}_s^{(m+1)} \quad (5.3)$$

Applied to the present case, we can adapt the Successive Approximation Algorithm in order to obtain the updated value of the field-dependent material matrix $\mathbf{M}_{\mu-1}(\hat{\mathbf{a}}_v^{(m+1)})$ via the generalized material coefficient's definition (4.7c) in combination with the field estimation method from Section 4.4. Effectively, this equals a repetition of the iterative scheme presented in Fig. 4.10 for each consecutive time step based on (5.3). We stress the fact that the simulated materials are not inherently nonlinear in the following example, but instead are treated by a mathematical model, which turns out to be nonlinear. If they are inherently nonlinear and the Successive Approximation Algorithm is employed already, then

an additional incorporation of the generalized material coefficient in each update cycle can be achieved very efficiently.

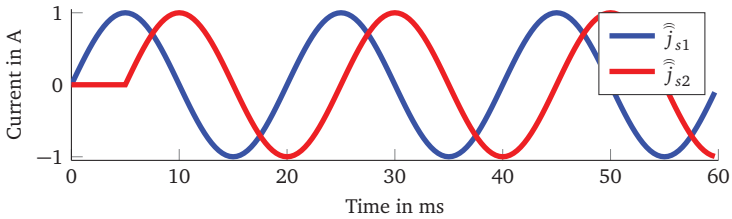
In order to induce and observe a temporal variation of the generalized coefficients at the material interface, we imprint two spatially distinct source currents into the computational domain that are constituted by phase shifted sines, as shown in Fig. 5.8a. By that measure, the field incidence angles α_k , which the coefficients $M_{\mu,k}^{\angle}$ are built upon, change in every time step. We monitor a probe signal $B_x^p(t)$ of the magnetic flux density's x -component at a different location inside a conductive region of the domain. Two different variants of the computational setup are depicted true to scale in Fig. 5.7. For the sake of comparison, we not only rely on a Cartesian (cf. Fig. 5.7a), but also on a triangular mesh (cf. Fig. 5.7b). The latter is used in conjunction with the Finite Element method, implemented by the CST Studio Suite [CST15]. An MQSTD solver on Cartesian meshes is not available in the CST Studio Suite.

We assign abbreviations to the different simulation approaches:

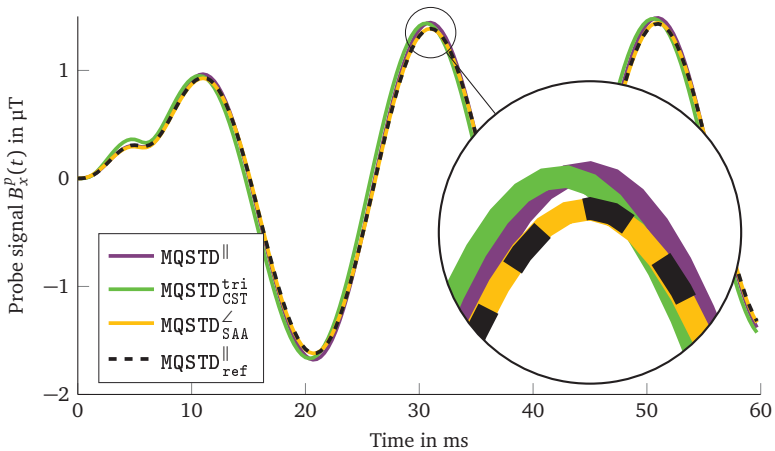
MQSTD	Conventional material averaging on the Cartesian mesh (cf. (4.4a)).
MQSTD _{ref}	Same as MQSTD , but higher mesh resolution with $\Delta x = \Delta y = \frac{L}{256}$.
MQSTD ^{<} _{SAA}	Successive Approximation Algorithm based on generalized material coefficient (4.7c) on the Cartesian mesh.
MQSTD ^{tri} _{CST}	Finite Element method on the triangular mesh, implemented by the CST Studio Suite.

There are some conceptual peculiarities in the simulation setup for the CST Studio Suite, which need to be addressed. The current sources, implemented as so called *coil segments*, cannot be made infinitely thin like in the MATLAB implementation of the Cartesian mesh. Making them reasonably small leads to a very inhomogeneous mesh in their vicinity (cf. Fig. 5.7b). Furthermore, the utilized time integration scheme is undisclosed and very likely based on a more advanced and more accurate technique than Backward Euler, which we use for our schemes on the Cartesian mesh. By these considerations, it seems advisable not to rely on MQSTD^{tri}_{CST} as a suitable reference solution, but instead verify our schemes against MQSTD^{||}_{ref}.

Fig. 5.8b shows the transient behavior of the recorded probe signals. All methods, including MQSTD^{tri}_{CST}, lead to qualitatively indiscernible results. A closer look reveals that the reference solution MQSTD^{||}_{ref} is approximated most accurately by MQSTD[<]_{SAA}, i.e. the iterative method based on the generalized material coefficient. This perception is confirmed by Table 5.3, which shows each probe signal's root-mean-square (RMS) error with respect to MQSTD^{||}_{ref}.



(a) Phase shifted excitation currents that are imprinted at the positions given in Fig. 5.7. The sines' frequency is 50 Hz. A total of 180 time samples is used, which results in a step size of $\Delta t = 1/3$ ms.



(b) The monitored probe signals that are recorded at the position given in Fig. 5.7 for different simulation approaches.

Figure 5.8.: Temporal dependence of excitation current and monitored probe signal.

	MQSTD $^{\angle}_{\text{SAA}}$	MQSTD $^{\parallel}$	MQSTD $^{\text{tri}}_{\text{CST}}$	MQSTD $^{\parallel}_{\text{ref}}$
RMS error in μT	0.0087	0.038	0.12	0
sim. time in s	14	1	41	21

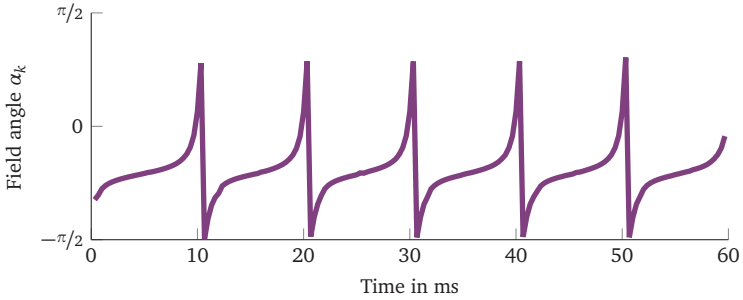
Table 5.3.: RMS error of probe signals and required time for simulation. The RMS error is given with respect to the reference solution MQSTD $^{\parallel}_{\text{ref}}$.

MQSTD $^{\text{tri}}_{\text{CST}}$'s large deviation has to be understood in the context of the chosen reference solution, which comprises some substantial conceptual differences (see above). With respect to a hypothetical exact solution of (5.1) for this example, it is likely to turn out more accurate than MQSTD $^{\angle}_{\text{SAA}}$ and MQSTD $^{\parallel}$ due to its ideally material-conforming mesh and its more elaborate time integration scheme.

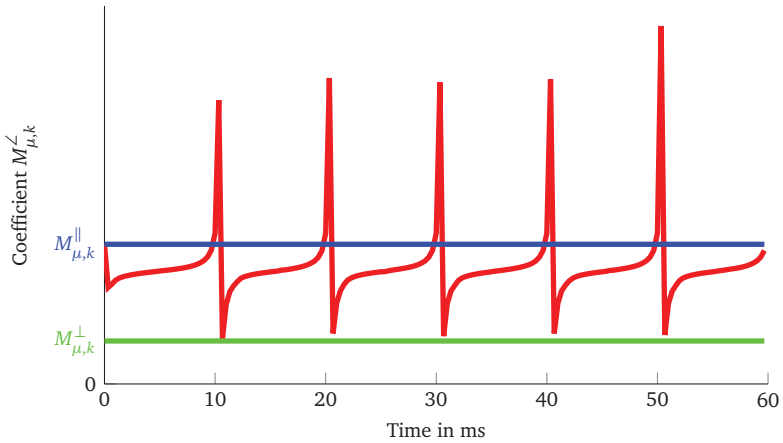
In terms of simulation times³, MQSTD $^{\parallel}$ is uncontestedly fast. However, the iterative approach MQSTD $^{\angle}_{\text{SAA}}$ offers a reasonable compromise between improved accuracy and reduced simulation time that cannot be achieved by a mesh refinement. Its speedup can be further increased by a more resource economical implementation that has not been the main focus of this work. All Cartesian mesh based algorithms even outperform the triangular mesh approach in the CST Studio Suite, which has to deal with approximately twice as much mesh cells in this example.

The remaining Figures 5.9a and 5.9b are given to demonstrate the working principle of the generalized material coefficient. Fig. 5.9a shows the estimated field incidence angle α_k for one particular facet/edge-pair $k = k_0$, which is cut by the interface (cf. Fig 5.7a). The periodically recurring pattern, which results from the spatially and temporally shifted, yet sinusoidal, excitation currents is clearly visible. Its smooth appearance is evidence for good accuracy of the field angles' estimation by means of the method described in Section 4.4. Under consideration of the interface angle $\theta_k = \theta$, as well as the respective cut- and material ratios, evaluating (4.7c) leads directly to the generalized material coefficient $M^{\angle}_{\mu,k}$, as shown in Fig. 5.9b. In this case, it ranges mostly between the conventional approximations $M^{\perp}_{\mu,k}$ and $M^{\parallel}_{\mu,k}$. An exception of this bounded behavior occurs whenever $\alpha_k > 0$. In conjunction with the positive interface angle θ_k , this directly reflects the predication of Fig. 4.3.

³Measured on an Intel Core i7-4770K CPU, 16 GB RAM, MATLAB R2014b.



(a) Progression of the estimated field angle α_k for $k = k_0$.



(b) The material coefficient $M_{\mu,k}^{\angle}$ after 15 iterations in each time step for $k = k_0$.

Figure 5.9.: Temporal dependence of monitored field angle and generalized material coefficient.

Summary and Outlook

The superordinate topic of this thesis are material interfaces that do not conform well with a Cartesian mesh system. Even though we extend the generally accepted meaning of the term *conformal* from perfect alignment of mesh facets and material interfaces to a more general definition that also permits partially filled cells under some constraints (cf. Fig. 4.1), typical simulations still suffer from a significant loss of accuracy. We trace this loss of accuracy back to a strongly simplified, yet commonly employed, approximation of the ideal material coefficient, which converges only linearly in the nonconformal case (cf. (4.9)). The awareness of this fundamental and restrictive property can be seen as the present thesis' central motivation, which emerges into two distinctive approaches with the aim to restore a second order accurate discretization.

The first approach, which is dealt with in Chapter 3, assumes the simulated object to be shaped in a way that qualifies it for being represented in a directly conformal sense by a cylindrical mesh. This constitutes a rather problem-specific approach that is readily described in the scope of the Finite Integration Technique in [Wei83; Deh93; DW94]. Our efforts focus on the employment of cylindrical meshes in time domain simulations, which is a rarely used combination due to severe restrictions that a cylindrical mesh imposes on the conventional FDTD algorithm. In order to quantify these restrictions, mesh specific CFL conditions for a time step size that leads to numerical stability are derived in Section 3.1. They clearly indicate that cylindrical FDTD comes at the price of a strongly diminished time step size in comparison to its deployment on comparable Cartesian meshes. Consequently, the extra effort due to a large number of required update cycles is likely to have yielded a more favorable outcome if it were invested in a highly resolved Cartesian simulation.

Therefore, we dedicate ourselves to modifications of the conventional FDTD scheme. The *Coupled Multi-Mode method* (cf. Section 3.2.1) is inspired by a similar approach for frequency domain simulations [Deh93; DW94]. Within its context, a technique called *Automated Mode Detection* enables unnecessary, yet strongly time step limiting, modal field contributions to be disabled. The outcome is shown to not even speed up the calculation significantly, but also increases its accuracy due to a better balanced ratio of temporal and spatial error terms (cf. Appendix B). A different FDTD modification, the *Hybrid Newmark-Beta method* (cf. Section 3.2.2),

achieves the same goals, but on an unaltered mesh system. Any Newmark-Beta scheme can be made unconditionally stable at the expense to be less accurate than FDTD. We apply it in a hybrid fashion very precisely only to those mesh components that are responsible for the time step degradation. Ultimately, a combination of both methods is shown to lead to very beneficial properties in many use cases and unifies each method's advantages.

The second main pillar of this thesis is constituted by Chapter 4 and takes an entirely different way to address the issue of nonconformal material interfaces. The concept of *generalized material modeling* (cf. (4.7)), which is mentioned in similar form in [Scho5], is first of all formally proven to converge quadratically even for arbitrarily tilted interfaces, as desired. After deducing the implications of the widely employed staircase approximation by means of this formula, two different means of implementing it in practice are discussed in Section 4.4. The first relies on a successive iteration, while the other yields results directly, based on a nondiagonal and unsymmetric material matrix. The latter is comparable to an existing *subpixel smoothing technique* [BWC11]. Despite the additional effort for both of them, they can be shown to reach a certain level of accuracy much faster than by a conventional mesh refinement. The extensibility to other areas of application, i.e. for dielectric materials, in three dimensions or for curved interfaces, is reasoned for in Section 4.5.1. We also address the side effect of indefinite material matrices with regard to the generalized coefficient's applicability in FDTD simulations with a most likely negative outcome.

Chapter 5 demonstrates the application of all essential concepts introduced in this thesis to practice-oriented examples. The Coupled Multi-Mode method and Hybrid Newmark-Beta come to action with the aim of determining the spectrum and resonant modes of optical devices in the micrometer regime. Their characteristic properties are highlighted and significant speedups are achieved. Comparisons to the commercial simulation software CST Studio Suite [CST15] prove to be favorable for the algorithms presented herein, at least in terms of accuracy. We also give a more realistic simulation example in Appendix D.

The accurate handling of nonconformal material interfaces is demonstrated by means of a time domain formulation of the magnetoquasistatic approximation of Maxwell's equations, like it is commonly used in electric machine simulations. Especially the iterative approach (cf. Section 4.4.1) turns out to integrate itself very well in an existing technique for handling nonlinear magnetic materials [DWoo].

In order for the presented methods to find consideration in user-friendly simulation software tools, some hurdles need to be overcome. Both the cylindrical, as well as the nonconformal Cartesian mesh approach make high demands on the mesh

generation process. There exist highly evolved mesh generators for unstructured tetrahedral meshes, e.g. Gmsh [GR09]. Nevertheless, versatile and user-friendly software for this purpose with regard to cylindrical meshes is not publicly available to the best of the author's knowledge. Cartesian mesh generators often rely on the staircase approximation or at least do not expose the edge's and facet's material cut ratios to the user without further measures. However, the generalized material coefficient's applicability is tightly limited without a possibility to obtain this information automatically.

Maxwell's Grid Equations for Bodies of Revolution

We carry out the following deduction in close analogy to [Deh93; DW94]. The main difference is the φ -dependence's description by complex exponentials instead of two separate sets of sines and cosines. This makes both polarizations treatable by means of the same (complex) equation.

As motivated in Section 2.2.5.4, the electric field and magnetic flux in a rotationally symmetric domain read:

$$\vec{E} = \sum_{m=-\infty}^{\infty} \vec{\mathfrak{E}}_m(\varrho, z) e^{jm\varphi} \quad (\text{A.1a})$$

$$\vec{B} = \sum_{m=-\infty}^{\infty} \vec{\mathfrak{B}}_m(\varrho, z) e^{jm\varphi} \quad (\text{A.1b})$$

$\vec{\mathfrak{E}}_m$ and $\vec{\mathfrak{B}}_m$ are Fourier coefficients that are also called azimuthal modes in the scope of this thesis. In the following, Maxwell's grid equations are derived based on considering the fields' Fourier expansions (A.1) for an arbitrary mode m . This is done exemplary for Faraday's Law, which is evaluated on a primary mesh facet A separately for each coordinate direction.

For a ϱ -facet situated at $\varrho = \varrho_0$ and ranging from $z = z_1$ to $z = z_2$ this yields:

$$\oint_{\partial A} \vec{E} \cdot d\vec{s} = -\frac{d}{dt} \iint_A \vec{B} \cdot d\vec{A} \quad (\text{A.2a})$$

$$\begin{aligned} \Leftrightarrow & \begin{cases} \int_{-\Delta\varphi/2}^{\Delta\varphi/2} E_\varphi(\varrho_0, \varphi, z_1) \varrho_0 d\varphi + \int_{z_1}^{z_2} E_z(\varrho_0, \Delta\varphi/2, z) dz \\ - \int_{-\Delta\varphi/2}^{\Delta\varphi/2} E_\varphi(\varrho_0, \varphi, z_2) \varrho_0 d\varphi - \int_{z_1}^{z_2} E_z(\varrho_0, -\Delta\varphi/2, z) dz \end{cases} \quad (\text{A.2b}) \\ & = -\frac{d}{dt} \int_{z_1}^{z_2} \int_{-\Delta\varphi/2}^{\Delta\varphi/2} B_\varrho(\varrho_0, \varphi, z) \varrho_0 d\varphi dz \end{aligned}$$

Substituting A.1 and carrying out the integrations results in:

$$\widehat{\mathbf{e}}_{m,\varphi}(z_1) - \widehat{\mathbf{e}}_{m,\varphi}(z_2) + jm\Delta\varphi \widehat{\mathbf{e}}_{m,z} = -\frac{d}{dt} \widehat{\mathbf{b}}_{m,\varrho} \quad (\text{A.3})$$

Analogously, evaluating Faraday's Law on a φ -directed facet yields:

$$\widehat{\mathbf{e}}_{m,\varrho}(z_2) - \widehat{\mathbf{e}}_{m,\varrho}(z_1) + \widehat{\mathbf{e}}_{m,z}(\varrho_1) - \widehat{\mathbf{e}}_{m,z}(\varrho_2) = -\frac{d}{dt} \widehat{\mathbf{b}}_{m,\varphi} \quad (\text{A.4})$$

Finally, choosing a z -directed facet results in:

$$-jm\Delta\varphi \widehat{\mathbf{e}}_{m,\varrho} - \widehat{\mathbf{e}}_{m,\varphi}(\varrho_1) + \widehat{\mathbf{e}}_{m,\varphi}(\varrho_2) = -\frac{d}{dt} \widehat{\mathbf{b}}_{m,z}. \quad (\text{A.5})$$

Since the φ dependence is explicitly integrable, the azimuthal step size is arbitrary and, for the sake of simplicity, set to $\Delta\varphi = 1$.

Inspecting the above equations allows for drawing conclusions about the partial derivative matrices' appearance. Specifically, \mathbf{P}_ϱ and \mathbf{P}_z seem to remain unchanged compared to the conventional case (cf. Section 2.2.5.1). The azimuthal operator, however, is constituted by an imaginary, diagonal matrix $\mathbf{P}_\varphi = -jm\mathbf{I}$.

The above deduction can be performed analogously for Ampère's Law, i.e. for dual mesh facets, which reveals that the duality relation 2.16 still holds by means of Hermitian transposition. The dual azimuthal operator, therefore, reads $\widehat{\mathbf{P}}_\varphi = -\mathbf{P}_\varphi^H = \mathbf{P}_\varphi = -jm\mathbf{I}$.

Evaluating Ampère's Law for a dual z -facet \tilde{A} at $\varrho = 0$ also leads to an important special case:

$$\oint_{\partial\tilde{A}} \vec{H} \cdot d\vec{s} = \frac{d}{dt} \iint_{\tilde{A}} \vec{D} \cdot d\vec{A} \quad (\text{A.6a})$$

$$\int_0^{2\pi} H_\varphi(\tilde{\varrho}_1, \varphi, z_0) \tilde{\varrho}_1 d\varphi = \frac{d}{dt} \int_0^{\tilde{\varrho}_1} \int_0^{2\pi} D_z(\varrho, \varphi, z_0) \varrho d\varphi d\varrho \quad (\text{A.6b})$$

$$\int_0^{2\pi} \sum_{m=-\infty}^{\infty} \mathfrak{H}_{m,\varphi}(\tilde{\varrho}_1, z_0) e^{jm\varphi} \tilde{\varrho}_1 d\varphi = \frac{d}{dt} \int_0^{\tilde{\varrho}_1} \int_0^{2\pi} \sum_{m=-\infty}^{\infty} \mathfrak{D}_{m,z}(\varrho, z_0) e^{jm\varphi} \varrho d\varphi d\varrho \quad (\text{A.6c})$$

$$\implies \hat{h}_{0,\varphi}(\tilde{\varrho}_1) = \frac{d}{dt} \hat{d}_{0,z}(\varrho = 0) \quad (\text{A.6d})$$

Because $\int_0^{2\pi} e^{jm\varphi} d\varphi$ vanishes for all $m \neq 0$, the electric grid flux $\hat{d}_{m,z}$ at $\varrho = 0$ exists only in case $m = 0$. This reflects on the radial derivative matrix \mathbf{P}_ϱ , which implements A.6d only for $m = 0$ and establishes no connection between $\hat{h}_{m,\varphi}(\tilde{\varrho}_1)$ and $\hat{d}_{m,z}(\varrho = 0)$ otherwise.

Conclusively, Maxwell's grid equations for an azimuthal mode m are obtained by adapting the pseudo-two-dimensional mesh geometry with $\Delta\varphi = 1$ and modifying the partial derivative operators \mathbf{P}_ϱ and \mathbf{P}_φ as described above.

Stability and Accuracy of Newmark-Beta Schemes

B.1. Discrete Dispersion Relation

The deduction of an equation that generalizes the continuous dispersion relation $k_x^2 + k_y^2 + k_z^2 = \omega^2/c^2$ to apply for discrete field quantities on equidistant Cartesian meshes in a homogeneous medium is outlined in [TH05]. The basic idea is to insert plane wave solutions for the electric and magnetic field into the discrete form of Maxwell's equations. The result for the conventional leapfrog method is as follows [TH05]:

$$\frac{\sin^2\left(\tilde{k}_x \frac{\Delta x}{2}\right)}{\left(\frac{\Delta x}{2}\right)^2} + \frac{\sin^2\left(\tilde{k}_y \frac{\Delta y}{2}\right)}{\left(\frac{\Delta y}{2}\right)^2} + \frac{\sin^2\left(\tilde{k}_z \frac{\Delta z}{2}\right)}{\left(\frac{\Delta z}{2}\right)^2} = \frac{\sin^2\left(\omega \frac{\Delta t}{2}\right)}{c^2 \left(\frac{\Delta t}{2}\right)^2} \quad (\text{B.1})$$

The wave numbers \tilde{k}_x , \tilde{k}_y and \tilde{k}_z are the so-called *discrete wave numbers* that arise from the discrete mesh representation when a temporal frequency ω is given. The discrete wave numbers are associated with a frequency $\tilde{\omega}$, which is called the *discrete frequency*. Since the entire left hand side only accounts for the spatial discretization, it is not affected by incorporating the Newmark-Beta extension. Therefore, in order to derive the dispersion relation's right hand side in dependence of β , it suffices to investigate (2.33), i.e.

$$\left(\Delta t^2 \beta \mathbf{A}_{\text{CC}} + \mathbf{I}\right) \bar{\mathbf{e}}^{(m+1)} = \begin{cases} -\left(\Delta t^2 (1 - 2\beta) \mathbf{A}_{\text{CC}} - 2\mathbf{I}\right) \bar{\mathbf{e}}^{(m)} \\ -\left(\Delta t^2 \beta \mathbf{A}_{\text{CC}} + \mathbf{I}\right) \bar{\mathbf{e}}^{(m-1)} \end{cases} \quad (\text{B.2})$$

in a spatially continuous domain ($\Delta x \rightarrow 0$, $\Delta y \rightarrow 0$ and $\Delta z \rightarrow 0$). In this limit, (B.1)'s left hand side results in $\tilde{\omega}^2/c^2$ and the matrix \mathbf{A}_{CC} equals the squared speed of light times the Laplacian¹, i.e. $\mathbf{A}_{\text{CC}} \rightarrow -c^2 \nabla^2$. Incorporating a plane wave $\bar{\mathbf{e}} = \bar{e}_0 \mathbf{e}^{j(\tilde{k}_x x + \tilde{k}_y y + \tilde{k}_z z)} \mathbf{e}^{j\omega t}$ with constant and scalar amplitude \bar{e}_0 then yields:

$$\left(\Delta t^2 \beta \tilde{\omega}^2 + 1\right) \mathbf{e}^{j\omega(m+1)\Delta t} = \begin{cases} -\left(\Delta t^2 (1 - 2\beta) \tilde{\omega}^2 - 2\right) \mathbf{e}^{j\omega m \Delta t} \\ -\left(\Delta t^2 \beta \tilde{\omega}^2 + 1\right) \mathbf{e}^{j\omega(m-1)\Delta t} \end{cases} \quad (\text{B.3})$$

¹This direct relationship between discrete and continuous operators is possible because the Finite Integration Technique results in a grid representation of Maxwell's equations that preserves their original appearance (cf. Section 2.2).

After several algebraic simplifications and resubstituting the left hand side of (B.1) for $\frac{\omega^2}{c^2}$, the resulting discrete dispersion relation for a Newmark-Beta scheme reads:

$$\frac{\sin^2\left(\tilde{k}_x \frac{\Delta x}{2}\right)}{\left(\frac{\Delta x}{2}\right)^2} + \frac{\sin^2\left(\tilde{k}_y \frac{\Delta y}{2}\right)}{\left(\frac{\Delta y}{2}\right)^2} + \frac{\sin^2\left(\tilde{k}_z \frac{\Delta z}{2}\right)}{\left(\frac{\Delta z}{2}\right)^2} = \frac{\sin^2\left(\omega \frac{\Delta t}{2}\right)}{c^2 \left(\frac{\Delta t}{2}\right)^2 (1 - 4\beta \sin^2\left(\omega \frac{\Delta t}{2}\right))} \quad (\text{B.4})$$

For $\beta = 0$, as expected, (B.1) results.

B.2. Numerical Stability

As also described in [TH05], the discrete dispersion relation permits the derivation of a CFL stability criterion for the time step size Δt in order to avoid numerical instability. A numerically stable algorithm does not have decaying or increasing field amplitudes in the absence of exciting currents and conductivities. Therefore, a monochromatic wave's frequency ω needs to be real and, consequently, the right hand side sine terms in (B.4) range between zero and one. The left hand side sine terms also can not be greater than one for real wave numbers, which allows for rearranging (B.4) to yield an upper bound for the time step size:

$$\Delta t \leq \frac{1}{c \sqrt{1 - 4\beta} \sqrt{\frac{1}{\Delta x^2} + \frac{1}{\Delta y^2} + \frac{1}{\Delta z^2}}} \quad (\text{B.5})$$

Again, the well-known CFL criterion for Cartesian meshes (2.29) results for $\beta = 0$. For $\beta \geq 1/4$ this formula loses its validity because the update scheme then becomes unconditionally stable [New59].

B.3. Accuracy

In order to quantitatively investigate the accuracy of an electromagnetic wave simulated on a Cartesian mesh with Newmark-Beta time integration, the discrete dispersion relation (B.4) is evaluated for a wave traveling along a specific direction. Only in that case it is possible to solve it explicitly for the discrete wave number. In the following the x -direction is chosen, so that only \tilde{k}_x exists:

$$\tilde{k}_x = \frac{2}{\Delta x} \arcsin\left(\frac{\Delta x}{c \Delta t} \frac{\sin\left(\omega \frac{\Delta t}{2}\right)}{\sqrt{1 - 4\beta \sin^2\left(\omega \frac{\Delta t}{2}\right)}}\right) \quad (\text{B.6})$$

Introducing the number of lines per (continuous) wavelength $\mathcal{S}_s = \frac{2\pi}{k_x \Delta x}$ and the number of time samples per (continuous) period $\mathcal{S}_t = \frac{2\pi}{\omega \Delta t}$, i.e. the spatial and temporal sampling rates, (B.6) equates to:

$$\tilde{k}_x = \frac{\mathcal{S}_s k_x}{\pi} \arcsin \left(\frac{\mathcal{S}_t}{\mathcal{S}_s} \frac{\sin\left(\frac{\pi}{\mathcal{S}_t}\right)}{\sqrt{1 - 4\beta \sin^2\left(\frac{\pi}{\mathcal{S}_t}\right)}} \right) \quad (\text{B.7})$$

This formulation allows for a closed form expression of the discrete wave number's relative error $\delta_{\tilde{k}_x} = \frac{\tilde{k}_x - k_x}{k_x}$:

$$\delta_{\tilde{k}_x} = \frac{\mathcal{S}_s}{\pi} \arcsin \left(\frac{\mathcal{S}_t}{\mathcal{S}_s} \frac{\sin\left(\frac{\pi}{\mathcal{S}_t}\right)}{\sqrt{1 - 4\beta \sin^2\left(\frac{\pi}{\mathcal{S}_t}\right)}} \right) - 1 \quad (\text{B.8})$$

Furthermore, investigating (B.8) in the limit of infinite sampling rates allows for closed form expressions of the spatial and temporal relative error, respectively. The spatial error equates to

$$\lim_{\mathcal{S}_t \rightarrow \infty} \delta_{\tilde{k}_x} = \frac{\mathcal{S}_s}{\pi} \arcsin \left(\frac{\pi}{\mathcal{S}_s} \right) - 1 \quad (\text{B.9})$$

whereas the temporal error results in

$$\lim_{\mathcal{S}_s \rightarrow \infty} \delta_{\tilde{k}_x} = \frac{\mathcal{S}_t}{\pi} \frac{\sin\left(\frac{\pi}{\mathcal{S}_t}\right)}{\sqrt{1 - 2\beta + 2\beta \cos\left(\frac{2\pi}{\mathcal{S}_t}\right)}} - 1 \quad (\text{B.10})$$

These individual errors, whose sum very well approximates the overall relative error, are visualized in Fig. B.1 in dependence of their respective sampling rate. In case $\beta = 0$ (conventional FDTD), both errors' superposition results in a vanishing overall error, which is known from [TH05] under the notion *magic time step*. Unfortunately, the spatial and temporal sampling rates can only be chosen equally in the one-dimensional case. Considering β and a three-dimensional, equidistantly meshed computational domain, the relationship between spatial and temporal sampling rate follows as:

$$\mathcal{S}_t = \mathcal{S}_s \sqrt{3} \sqrt{1 - 4\beta} \quad (\text{B.11})$$

It can be inferred from (B.5). By this result, it becomes impossible to generally extinct the overall simulation error, especially if a wave's propagation direction is no longer unique and known a priori.

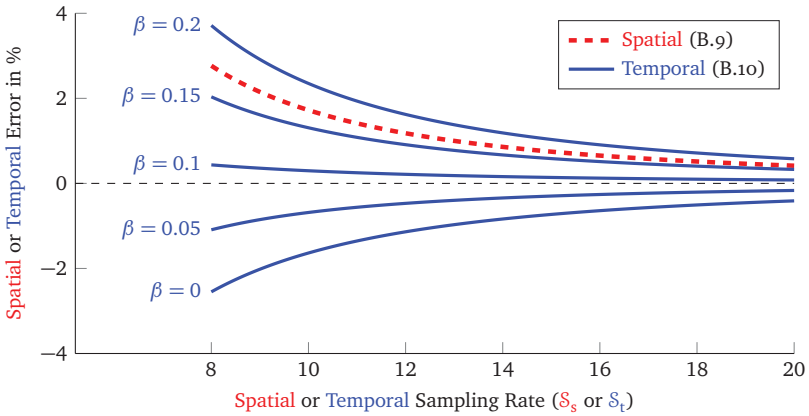


Figure B.1.: Spatial and temporal discretization error in dependence of the respective sampling rate, evaluated for several choices of β .

Fig. B.1 also allows for drawing the conclusion that, typically, large choices of β turn out to be disadvantageous in terms of accuracy. Beyond a certain value of β the temporal error even changes its sign and, therefore, emphasizes the overall error instead of diminishing it.

Due to the extensive simplifications made to obtain these results, their implications on accuracy for realistic applications have to be reasoned carefully. Nevertheless, it seems reasonable to infer that exploiting Newmark-Beta's relaxed CFL criterion to full extent, especially for large values of β , drastically deteriorates accuracy. Numerical results from [GN95] support this conclusion. Newmark-Beta should, therefore, be used only if the positive effects of an increased time step size prospectively outweigh the disadvantage of reduced accuracy. It is, furthermore, advisable to take measures that restrict the method to small parts of the simulation and to make sure that β is only chosen as high as necessary (cf. Section 3.2.2).

Another important implication of Fig. B.1, specifically for conventional FDTD methods ($\beta = 0$), is that the time step size should be chosen as close to the stability limit as possible. Otherwise, the temporal sampling rate S_t becomes even larger compared to the spatial sampling rate S_s than it already is due to (B.11). Both error terms are then even more unlikely to cancel out. This result, which is also known from [TH05], is used in Section 3.1.3 to explain why increasing the time step size in time domain methods on cylindrical meshes is usually favorable in terms of accuracy.

Detailed Deduction of Convergence Rates

The convergence rates of approximations of the ideal material coefficient $M_{\mu,k} = \widehat{b}_k/\widehat{h}_k$ are of great importance in order to make accurate predictions about the convergence rates of the Finite Integration Technique in case of nonconformal material interfaces (cf. Section 4.2.3.1). They are motivated and given in Sections 4.1 and 4.2 with only a very brief mathematical deduction. To better comprehend their origin, we carry out the deductions in the following in more detail. Therefore, let us restate (4.6), the starting point of their derivation:

$$M_{\mu,k} = \frac{\int_{A_k^a} (\mu_a H_t^a \cos \theta - B_n^a \sin \theta) dA + \int_{A_k^b} (\mu_b H_t^b \cos \theta - B_n^b \sin \theta) dA}{\int_{\bar{I}_k^a} (H_t^a \cos \theta - \frac{1}{\mu_a} B_n^a \sin \theta) ds + \int_{\bar{I}_k^b} (H_t^b \cos \theta - \frac{1}{\mu_b} B_n^b \sin \theta) ds} \quad (\text{C.1})$$

C.1. Generalized Material Coefficient

In order to reformulate (C.1) in terms of the generalized material coefficient $M_{\mu,k}^{\triangleleft}$ and an error term (cf. (4.7)), we exemplarily evaluate one integral from the numerator and one from the denominator after inserting the Taylor series expansion (4.2). As indicated in Fig. 4.1, the Taylor expansion points P_k coincide with the intersection point of primary facet and dual edge. It suffices to integrate H_t^a and B_n^a , for which we use the placeholder Ψ . Their continuity is assured by the absence of material discontinuities in their respective region of integration. Furthermore, we assume them to be sufficiently differentiable.

An exemplary calculation for the numerator then reads:

$$\int_{A_k^a} \Psi dA = \iint_{A_k^a} \left(\Psi|_{P_k} + \frac{\partial \Psi}{\partial v} \Big|_{P_k} v + \frac{\partial \Psi}{\partial w} \Big|_{P_k} w + \mathcal{O}(v^2, w^2) \right) dv dw \quad (\text{C.2a})$$

$$= A_k^a \Psi|_{P_k} + \mathcal{O}(\Delta) \left(\frac{\partial \Psi}{\partial v} \Big|_{P_k} \frac{\mathcal{O}(\Delta^2)}{2} + \frac{\partial \Psi}{\partial w} \Big|_{P_k} \frac{\mathcal{O}(\Delta^2)}{2} \right) + \mathcal{O}(\Delta^4) \quad (\text{C.2b})$$

$$= A_k^a \Psi|_{P_k} + \mathcal{O}(\Delta^3) \quad (\text{C.2c})$$

The second order terms $\mathcal{O}(\Delta^2)$ in (C.2b) result from substituting the bounds of a parameterization of A_k^a for the integrated linear terms. Since the Taylor series' expansion point P_k is aligned centrally on A_k , the asymmetric integration region (A_k^a) prevents the non-constant parts of the Taylor series from canceling out after integration. Along with a linearly converging contribution from the other variable, this ultimately adds a cubically converging error to the desired solution.

We now perform a similar integration along the dual edge's direction u for a denominator term of (C.1). In this case, u_1^a and u_2^a are the supposed limits of the present (sub-)edge \tilde{L}_k^a :

$$\int_{\tilde{L}_k^a} \Psi ds = \int_{u_1^a}^{u_2^a} \left(\Psi|_{P_k} + \frac{\partial \Psi}{\partial u} \Big|_{P_k} u + \frac{\partial^2 \Psi}{\partial u^2} \Big|_{P_k} \frac{u^2}{2} + \mathcal{O}(u^3) \right) du \quad (\text{C.3a})$$

$$= \tilde{L}_k^a \Psi|_{P_k} + \underbrace{\left[\frac{\partial \Psi}{\partial u} \Big|_{P_k} \frac{u^2}{2} \right]_{u_1^a}^{u_2^a}}_{\mathcal{O}(\Delta^2)} + \underbrace{\left[\frac{\partial^2 \Psi}{\partial u^2} \Big|_{P_k} \frac{u^3}{6} \right]_{u_1^a}^{u_2^a}}_{\mathcal{O}(\Delta^3)} + \mathcal{O}(\Delta^4) \quad (\text{C.3b})$$

$$= \tilde{L}_k^a \Psi|_{P_k} + \mathcal{O}(\Delta^2) \quad (\text{C.3c})$$

The denominator's error term therefore converges quadratically. These results lead directly to (4.7b), which we restate and explicitly reformulate several times until we arrive at the generalized material coefficient's definition (4.7c):

$$M_{\mu,k} = \frac{\overbrace{\left[H_t^a \cos \theta \right]_{P_k} \left(A_k^a \mu_a + A_k^b \mu_b \right) - \left[B_n^a \sin \theta \right]_{P_k} A_k}^{\Gamma \in \mathcal{O}(\Delta^2)}}{\underbrace{\left[H_t^a \cos \theta \right]_{P_k} \tilde{L}_k - \left[B_n^a \sin \theta \right]_{P_k} \left(\tilde{L}_k \frac{1}{\mu_a} + \tilde{L}_k \frac{1}{\mu_b} \right)}_{\Pi \in \mathcal{O}(\Delta)}} + \mathcal{O}(\Delta^3) \quad (\text{C.4a})$$

$$= \frac{\Gamma(1 + \mathcal{O}(\Delta))}{\Pi(1 + \mathcal{O}(\Delta))} = \frac{\Gamma}{\Pi} (1 + \mathcal{O}(\Delta))(1 - \mathcal{O}(\Delta)) \quad (\text{C.4b})$$

$$= \frac{\Gamma}{\Pi} (1 + \mathcal{O}(\Delta)) = \frac{\Gamma}{\Pi} + \mathcal{O}(\Delta^2) = M_{\mu,k}^{\angle} + \mathcal{O}(\Delta^2) \quad (\text{C.4c})$$

C.2. Conventional Material Coefficient

The previous deduction also covers the conventional material coefficients' definitions $M_{\mu,k}^{\parallel}$ and $M_{\mu,k}^{\perp}$ in the conformal case (cf. (4.4)), as well as their convergence rates.

Under the assumption of conformity, either H_t^a (parallel case) or B_n^a (perpendicular case) in (C.4a) can be set to zero, without altering the error terms.

As described in Section 4.2.1, the deployment of the conventional coefficients $M_{\mu,k}^{\parallel}$ and $M_{\mu,k}^{\perp}$ in the nonconformal case is possible as well and leads to a generalization of the well-known staircase approximation. Their reduced convergence rate can be reasoned for elegantly by means of a small modification of the previous deduction. We still need to make sure that either H_t^a or B_n^a vanish. Since this does no longer happen by virtue of the conformity of material and mesh, it has to be induced artificially. We realize this omission exemplarily for H_t^a by replacing it in (C.1) with a constant error term $\mathcal{O}(1)$:

$$M_{\mu,k} = \frac{\int_{A_k^a} (\mathcal{O}(1) - B_n^a \sin \theta) dA + \int_{A_k^b} (\mathcal{O}(1) - B_n^a \sin \theta) dA}{\int_{\tilde{L}_k^a} (\mathcal{O}(1) - \frac{1}{\mu_a} B_n^a \sin \theta) ds + \int_{\tilde{L}_k^b} (\mathcal{O}(1) - \frac{1}{\mu_b} B_n^a \sin \theta) ds} \quad (\text{C.5})$$

The following relations hold:

$$\int_{A_k^a} \mathcal{O}(1) dA \in \mathcal{O}(\Delta^2) \quad (\text{C.6a})$$

$$\int_{\tilde{L}_k^a} \mathcal{O}(1) ds \in \mathcal{O}(\Delta) \quad (\text{C.6b})$$

Subsequently, the numerator's and denominator's convergence rates are diminished by one order with respect to (C.4a), while the remaining field terms cancel out:

$$M_{\mu,k} = \frac{A_k + \mathcal{O}(\Delta^2)}{\tilde{L}_k \langle \mu^{-1} \rangle_{\tilde{L}_k} + \mathcal{O}(\Delta)} = \frac{A_k (1 + \mathcal{O}(1))}{\tilde{L}_k \langle \mu^{-1} \rangle_{\tilde{L}_k} (1 + \mathcal{O}(1))} \quad (\text{C.7a})$$

$$= \frac{A_k}{\tilde{L}_k \langle \mu^{-1} \rangle_{\tilde{L}_k}} (1 + \mathcal{O}(1)) = \frac{A_k}{\tilde{L}_k \langle \mu^{-1} \rangle_{\tilde{L}_k}} + \mathcal{O}(\Delta) \quad (\text{C.7b})$$

$$= M_{\mu,k}^{\parallel} + \mathcal{O}(\Delta) \quad (\text{C.7c})$$

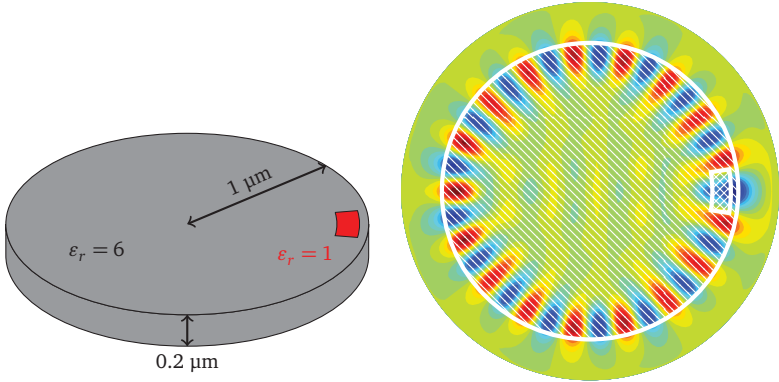
The perpendicular coefficient $M_{\mu,k}^{\perp}$ resulted in the same manner if B_n^a were replaced by a constant error term instead of H_t^a .

Extended Example of Pierced Microdisk

The application example provided herein represents an extension of the pierced microdisk example from Section 5.1.2 in combination with the algorithm HNB3D from Section 3.2.3. It is taken unmodified from the author's publication [KS13d] and the associated presentation [KS13e]. Besides slightly modified geometry and material parameters (cf. Fig. D.1a), the main difference to the example from Section 5.1.2 is a much finer mesh that also extends along the z -coordinate, as shown in Fig. D.1c. Furthermore, the computational domain is terminated radially by means of a 75 nm thick Perfectly Matched Layer [Bér94; TCoo] in order to absorb radiated fields. The PML's implementation in time domain with specific regard to the cylindrical mesh system is carried out as described in [Kir10].

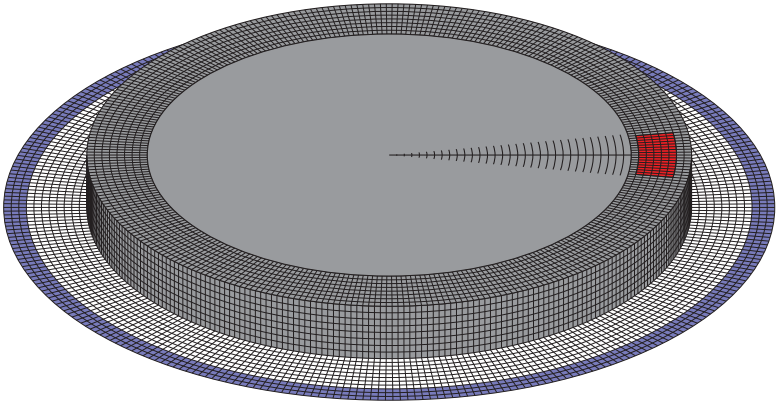
A reference simulation on an entirely three-dimensional mesh comprises about 850,000 degrees of freedom and leads to a time step size of $\Delta t = 2.0 \cdot 10^{-18}$ s. The discretization of the computational domain's inner part with a BOR mesh enlarges the time step size to $\Delta t = 4.1 \cdot 10^{-17}$ s, i.e. by 20 times. Along with the reduction to only about 360,000 degrees of freedom, this leads to a total speedup of 11.5.

Due to the presence of an absorbing boundary in radial direction, Fig. D.1a shows the radiation of fields in the direction given by the piercing much clearer than Fig. 5.5c, which is based on conventional, i.e. reflecting, boundary conditions.



(a) Geometry and material parameters.

(b) Real part of the electric field's z -component in a central cutting plane at 411.8 THz.



(c) True to scale mesh setup. The inner part (up to $0.8 \mu\text{m}$) is discretized by means of a multi-modal BOR mesh with 20 azimuthal modes. The mesh step sizes are $\Delta\rho = \Delta z = 25 \text{ nm}$ and $\Delta\varphi = \frac{2\pi}{302}$. Blue cells indicate the location of the Perfectly Matched Layer.

Figure D.1.: Computational setup and results of a pierced microdisk, as shown in [KS13e].

Nomenclature

General and Mathematical Symbols

(u, v, w)	General, orthogonal coordinates
(x, y, z)	Cartesian coordinates
$(\tilde{x}, \tilde{y}, \tilde{z})$	tilted Cartesian coordinate system
(ϱ, φ, z)	Cylindrical coordinates
$A, \partial A$	facet and its boundary path
δ_{ij}	Kronecker's Delta
$d\vec{s}, d\vec{A}, dV$	infinitesimal path, facet and volume element
\vec{e}_u	unit vector in u -direction
e	Euler's number, $e = 2.7182\dots$
h_u	metric coefficient for u
\mathbf{I}	identity matrix
j	imaginary unit, $j = \sqrt{-1}$
∇	nabla operator
\mathcal{N}	Gaussian normal distribution
\mathcal{O}	Landau operator
π	ratio of a circle's circumference to its diameter, $\pi = 3.1415\dots$
\vec{r}	spatial variable
\Re	real part operator
t	temporal variable
$V, \partial V$	volume and its boundary facet

Space- and Time-Continuous Field Theory

\vec{A}	vector potential
a, b	indices of materials on both sides of interface \mathcal{J}
\vec{B}	magnetic flux density
B_n, H_t	normal and tangential flux density and field components w.r.t the interface
c, c_0	speed of light inside a medium and in vacuum
\vec{D}	electric flux density
\vec{E}	electric field strength
$\vec{\mathcal{E}}_m, \vec{\mathcal{D}}_m$	electric field's and flux density's mth Multi-Mode coefficient
ε	permittivity
ε_0	free-space permittivity
ε_r	relative permittivity
Φ	scalar potential
\vec{H}	magnetic field strength
$\vec{\mathcal{H}}_m, \vec{\mathcal{B}}_m$	magnetic field's and flux density's mth Multi-Mode coefficient
\mathcal{J}	interface between different materials
\vec{J}	electric current density
\vec{J}_c, \vec{J}_s	conduction and source current density
\vec{K}	surface current density
k_x	wave number along x
m	azimuthal mode order
μ	permeability
μ_0	free-space permeability

μ_r	relative permeability
\vec{n}, \vec{t}	normal and tangential unit vector on interface J
ρ_q	electric charge density
σ	conductivity
ς_q	surface charge density
Ψ	placeholder for quantities subject to Taylor series expansion
ω	angular frequency

(Time-Discrete) Finite Integration Technique

(ξ, η, ζ)	index triplet to address a mesh element
$\langle \mu^{-1} \rangle_{\tilde{L}_k}$	edge-weighted average of inverse permeability
$\langle \mu \rangle_{A_k}$	facet-weighted average of permeability
α, α_k	angle between field and interface J (in general and locally at P_k)
\mathbf{A}_{CC}	curl-curl-matrix $\mathbf{A}_{CC} = \mathbf{M}_\varepsilon^{-1} \mathbf{C}^T \mathbf{M}_\mu^{-1} \mathbf{C}$
A_k, \tilde{A}_k	primary and dual facet
$\mathbf{A}_\varrho, \mathbf{A}_z$	system matrices for semi-implicit update scheme
$\vec{\mathbf{a}}_z, \vec{\mathbf{a}}_{z,\text{ref}}$	vector of z -directed line integrals over magnetic vector potential \vec{A} and its analytically computed reference solution
β, γ	Newmark-Beta parameters
β_ξ	radially dependent parameter β
$\vec{\mathbf{b}}, \vec{\mathbf{b}}_k$	magnetic grid flux vector and its k th element
$B_x^p(t)$	temporal probe signal recorded during simulation
$\mathbf{C}, \tilde{\mathbf{C}}$	primary and dual curl matrix
\mathbf{D}_ε	averaged permittivity matrix

\mathbf{D}_μ	averaged permeability matrix
\mathbf{D}_σ	averaged conductivity matrix
$\delta_{\tilde{k}_x}$	relative error of discrete wave number w.r.t. the continuous one
Δ	largest mesh step size
Δt	time step size
Δt_{3D}	time step size in three-dimensional part of computational domain
Δt_{BOR}	time step size in multi-modal part of computational domain
Δu_ξ	mesh step size in u -direction
$\widehat{\mathbf{d}}, \widehat{\mathbf{d}}_k$	electric grid flux vector and its k th element
$\widehat{\mathbf{e}}_{aux}, \widehat{h}_{aux,m}$	auxiliary grid voltages for three-dimensional and multi-modal domain
$\widehat{\mathbf{e}}, \widehat{e}_k$	electric grid voltage vector and its k th element
$\widehat{\mathbf{e}}_m, \widehat{\mathbf{d}}_m$	m th Multi-Mode coefficient vector of $\widehat{\mathbf{e}}$ and $\widehat{\mathbf{d}}$
$\widehat{\mathbf{e}}^{(m)}, \widehat{\mathbf{h}}^{(m+1/2)}$	temporally discrete electric and magnetic grid voltage
$\mathcal{E}_{k,m}$	cell- and mode-wise contribution to discrete electromagnetic energy at time step m
$\mathcal{E}_m^{(m)}, \mathcal{E}_{BOR}^{(m)}$	discrete electromagnetic energy per mode m and the total energy in the multi-modal domain
$\mathcal{E}^{(m)}, \mathcal{E}_k^{(m)}$	discrete electromagnetic energy at time step m and its cell-wise contribution
\mathbb{E}	relative error norm of FIT quantity w.r.t. reference solution
$\mathcal{G}, \widetilde{\mathcal{G}}$	primary and dual mesh
Γ, Π	abbreviations for generalized material coefficient's numerator and denominator
$\widehat{\mathbf{h}}, \widehat{h}_k$	magnetic grid voltage vector and its k th element

$\widehat{\mathbf{h}}_m, \widehat{\mathbf{b}}_m$	mth Multi-Mode coefficient vector of $\widehat{\mathbf{h}}$ and $\widehat{\mathbf{b}}$
i	locally assigned index of k 's directly adjacent neighbors
$\widehat{\mathbf{J}}, \widehat{J}_k$	electric grid current vector and its k th element
k	canonical index
L_k, \widetilde{L}_k	primary and dual edge
$\mathbf{L}_\varrho, \mathbf{U}_\varrho$	LU decomposition of \mathbf{A}_ϱ with $\mathbf{A}_\varrho = \mathbf{L}_\varrho \mathbf{U}_\varrho$
m	time step index
$\mathbf{M}_\varepsilon, M_{\varepsilon,k}$	dielectric material matrix and its k th main diagonal entry
$\mathbf{M}_\mu, M_{\mu,k}$	magnetic material matrix and its k th main diagonal entry
$\mathbf{M}_\sigma, M_{\sigma,k}$	conductivity material matrix and its k th main diagonal entry
$\mathbf{M}_{\mu^{-1}}$	(generally nondiagonal) reluctivity material matrix
$\mathbf{M}_{\mu^{-1},k,i}$	contribution of i to k th row of nondiagonal reluctivity matrix $\mathbf{M}_{\mu^{-1}}$
\mathbf{M}_β	diagonal matrix for edge-wise assignment of parameter β
$\mathcal{M}, \mathcal{M}_k$	symmetric energy matrix and its cell-wise contribution
$\mathfrak{M}_m, \widetilde{\mathfrak{M}}_m$	mth primary and dual Multi-Mode transformation matrix
m_{\max}	highest azimuthal mode order
$M_{\mu,k}^\angle$	generalized material coefficient
$M_{\mu,k}^\parallel, M_{\mu,k}^\perp$	material coefficient in parallel and perpendicular case
M_u	increment of canonical index k along u
ν	fixed-point iteration index
N_p	number of mesh nodes
N_u	number of nodes along u
P_k	intersection point of primary facet A_k and dual edge \widetilde{L}_k

$\mathbf{P}_u, \tilde{\mathbf{P}}_u$	primary and dual partial difference matrix w.r.t. u
\mathbf{q}	electric grid charge vector
θ, θ_k	angle between mesh axis and interface \mathcal{J} (in general and locally at P_k)
$\Theta_{k,i}$	local 2×2 -matrix to obtain grid fluxes from interface-continuous components
Ξ_k	local 1×2 -matrix to obtain grid voltage from interface-continuous components
$\varrho_{\text{BOR}}, \tilde{\varrho}_{\text{BOR}}$	primary and dual radius of interface between multi-modal and three-dimensional mesh
$\tilde{\varrho}_{\text{min}}$	dual radius of innermost mesh cell
s_α	standard deviation of field angle α_k
$\mathbf{S}, \tilde{\mathbf{S}}$	primary and dual source matrix
S_s, S_t	mesh lines per wavelength and time samples per period, i.e. spatial and temporal sampling rate
τ	offset multiplier
t_{exc}	duration of excitation signal
$\tilde{\omega}, \tilde{k}_x$	discrete frequency and wave number along x

Bibliography

External Literature

In alphabetical order

- [Ban11] B. Bandlow. “Zur Berechnung elektromagnetischer Eigenwertprobleme in der numerischen Simulation von Nanostrukturen mit periodischen und transparenten Randbedingungen”. PhD thesis. Universität Paderborn, 2011.
- [Bér94] J.-P. Bérenger. “A Perfectly Matched Layer for the Absorption of Electromagnetic Waves”. In: *Journal of Computational Physics* 114.2 (1994), pp. 185–200.
- [Bro65] C. G. Broyden. “A Class of Methods for Solving Nonlinear Simultaneous Equations”. In: *AMS Mathematics of Computation* 19 (1965), pp. 577–593.
- [Büs11] H. Büssing. *Finite Integration auf Tetraedergittern*. Verlag Dr. Hut, 2011.
- [BWC11] C. A. Bauer, G. R. Werner, and J. R. Cary. “A Second-Order 3D Electromagnetics Algorithm for Curved Interfaces between Anisotropic Dielectrics on a Yee Mesh”. In: *Journal of Computational Physics* 230.5 (2011), pp. 2060–2075.
- [CBS12] C. Classen, B. Bandlow, and R. Schuhmann. “Local Approximation Based Material Averaging Approach in the Finite Integration Technique”. In: *IEEE Transactions on Magnetics* 48.2 (2012), pp. 447–450.
- [CF94] Q. Chen and V. Fusco. “Three Dimensional Cylindrical Coordinate Finite-Difference Time-Domain Analysis of Curved Slotline”. In: *Second International Conference on Computation in Electromagnetics*. 1994, pp. 323–326.
- [CFL28] R. Courant, K. Friedrichs, and H. Lewy. “Über die partiellen Differenzengleichungen der mathematischen Physik”. In: *Mathematische Annalen* 100.1 (1928), pp. 32–74.
- [CN47] J. Crank and P. Nicolson. “A Practical Method for Numerical Evaluation of Solutions of Partial Differential Equations of the Heat-Conduction Type”. In: *Mathematical Proceedings of the Cambridge Philosophical Society*. Vol. 43. 1. Cambridge University Press. 1947, pp. 50–67.

- [Coro08] M. Corral. *Vector Calculus*. Online, accessed November 10th, 2015, 2008. URL: <http://www.mecmath.net/calc3book.pdf>.
- [CW01] M. Clemens and T. Weiland. “Discrete Electromagnetism with the Finite Integration Technique”. In: *Progress In Electromagnetics Research* 32 (2001), pp. 65–87.
- [CW07] J. Chen and J. Wang. “Stability Condition for Body-of-Revolution Finite-Difference Time-Domain Method”. In: *Electronics Letters* 43.21 (2007), p. 1126.
- [CW08] J. Chen and J. Wang. “The Body-of-Revolution Hybrid Implicit-Explicit Finite-Difference Time-Domain Method With Large Time Step Size”. In: *IEEE Transactions on Electromagnetic Compatibility* 50.2 (2008), pp. 369–374.
- [CW11] J. Chen and J. Wang. “Improved Hybrid Implicit-Explicit Finite-Difference Time-Domain Method with Higher Accuracy and User-Defined Stability Condition”. In: *AEÜ - International Journal of Electronics and Communications* 65.3 (2011), pp. 265–267.
- [CW12] J. Currie and D. I. Wilson. “OPTI: Lowering the Barrier Between Open Source Optimizers and the Industrial MATLAB User”. In: *Foundations of Computer-Aided Process Operations*. Ed. by N. Sahinidis and J. Pinto. Savannah, Georgia, USA, 2012.
- [CW99] M. Clemens and T. Weiland. “Numerical Algorithms for the FDiTD and FDFD Simulation of Slowly Varying Electromagnetic Fields”. In: *International Journal of Numerical Modelling: Electronic Networks, Devices and Fields* 12.1-2 (1999), pp. 3–22.
- [DDH01] A. Ditkowski, K. Dridi, and J. Hesthaven. “Convergent Cartesian Grid Methods for Maxwell’s Equations in Complex Geometries”. In: *Journal of Computational Physics* 170.1 (2001), pp. 39–80.
- [Deh93] M. Dehler. “Numerische Lösung der Maxwell’schen Gleichungen auf kreiszylindrischen Gittern”. PhD thesis. Technische Hochschule Darmstadt, 1993.
- [Dem97] J. W. Demmel. *Applied Numerical Linear Algebra*. Siam, 1997.
- [Dib+99] N. Dib, T. Weller, M. Scardelletti, and M. Imparato. “Analysis of Cylindrical Transmission Lines with the Finite-Difference Time-Domain Method”. In: *IEEE Transactions on Microwave Theory and Techniques* 47.4 (1999), pp. 509–512.

- [DM98] S. Dey and R. Mittra. “A Locally Conformal Finite Difference Time Domain Technique for Modeling Arbitrary Shaped Objects”. In: *IEEE Antennas and Propagation Society International Symposium*. Vol. 1. 1998, pp. 584–587.
- [Doh92] M. Dohlus. “Ein Beitrag zur Berechnung elektromagnetischer Felder im Zeitbereich”. PhD thesis. Technische Hochschule Darmstadt, 1992.
- [DW00] S. Drobny and T. Weiland. “Numerical Calculation of Nonlinear Transient Field Problems with the Newton-Raphson Method”. In: *IEEE Transactions on Magnetics* 36.4 (2000), pp. 809–812.
- [DW94] M. Dehler and T. Weiland. “A New Spectral Domain Technique for the Calculation of Eigenvalues in Curvilinear Coordinates”. In: *IEEE Transactions on Magnetics* 30.5 (1994), pp. 3574–3577.
- [ESW04] F. Edelvik, R. Schuhmann, and T. Weiland. “A General Stability Analysis of FIT/FDTD Applied to Lossy Dielectrics and Lumped Elements”. In: *International Journal of Numerical Modelling: Electronic Networks, Devices and Fields* 17.4 (4 2004), pp. 407–419.
- [Far+06] A. Farjadpour, D. Roundy, A. Rodriguez, M. Ibanescu, P. Bermel, J. D. Joannopoulos, S. G. Johnson, and G. W. Burr. “Improving Accuracy by Subpixel Smoothing in the Finite-Difference Time Domain”. In: *Optics Letters* 31.20 (2006), pp. 2972–2974.
- [FB01] M. Fujita and T. Baba. “Proposal and Finite-Difference Time-Domain Simulation of Whispering Gallery Mode Microgear Cavity”. In: *IEEE Journal of Quantum Electronics* 37.10 (2001), pp. 1253–1258.
- [FB02] M. Fujita and T. Baba. “Microgear Laser”. In: *Applied Physics Letters* 80.12 (2002), pp. 2051–2053.
- [Fus90] M. Fusco. “FDTD Algorithm in Curvilinear Coordinates”. In: *IEEE Transactions on Antennas and Propagation* 38.1 (1990), pp. 76–89.
- [GN95] S. Gedney and U. Navsariwala. “An Unconditionally Stable Finite Element Time-Domain Solution of the Vector Wave Equation”. In: *IEEE Microwave and Guided Wave Letters* 5.10 (1995), pp. 332–334.
- [Gus75] B. Gustafsson. “The Convergence Rate for Difference Approximations to Mixed Initial Boundary Value Problems”. English. In: *Mathematics of Computation* 29.130 (1975), pp. 396–406.
- [Hen15] H. Henke. *Elektromagnetische Felder: Theorie und Anwendung*. 5th ed. Springer Vieweg, 2015.

- [HJ12] R. A. Horn and C. R. Johnson. *Matrix Analysis*. Cambridge University Press, 2012.
- [Hol93] R. Holland. “Pitfalls of Staircase Meshing”. In: *IEEE Transactions on Electromagnetic Compatibility* 35.4 (1993), pp. 434–439.
- [Jac98] J. D. Jackson. *Classical Electrodynamics*. Vol. 3. Wiley, New York, 1998.
- [KCo3] F. Kung and H. T. Chuah. “Stability of Classical Finite-Difference Time-Domain (FDTD) Formulation with Nonlinear Elements — A New Perspective”. In: *Progress In Electromagnetics Research* 42 (2003), pp. 49–89.
- [KK73] R. D. Krieg and S. W. Key. “Transient Shell Response by Numerical Time Integration”. In: *International Journal for Numerical Methods in Engineering* 7.3 (1973), pp. 273–286.
- [Kot33] V. A. Kotelnikov. “On the Carrying Capacity of the Ether and Wire in Telecommunications”. In: *Material for the First All-Union Conference on Questions of Communication, Izd. Red. Upr. Svyazi RKKa, Moscow*. 1933.
- [Kri+98] B. Krietenstein, R. Schuhmann, P. Thoma, and T. Weiland. “The Perfect Boundary Approximation Technique Facing the Big Challenge of High Precision Field Computation”. In: *Proceedings of the XIX International Linear Accelerator Conference (LINAC 98), Chicago, USA*. 1998, pp. 860–862.
- [Kue15] L. Kuen. “Lösungsverfahren zur Behandlung teilgefüllter Zellen in der Finiten Integrationstechnik”. MA thesis. Technische Universität Berlin, 2015.
- [Lie+13] T. Liebig, A. Rennings, S. Held, and D. Erni. “openEMS – A Free and Open Source Equivalent-Circuit (EC) FDTD Simulation Platform Supporting Cylindrical Coordinates Suitable for the Analysis of Traveling Wave MRI Applications”. In: *International Journal of Numerical Modelling: Electronic Networks, Devices and Fields* 26.6 (2013), pp. 680–696.
- [LR56] P. D. Lax and R. D. Richtmyer. “Survey of the Stability of Linear Finite Difference Equations”. In: *Communications on Pure and Applied Mathematics* 9.2 (1956), pp. 267–293.
- [Max65] J. C. Maxwell. “A Dynamical Theory of the Electromagnetic Field”. In: *Philosophical Transactions of the Royal Society of London* (1865).

- [Mono3] P. Monk. *Finite Element Methods for Maxwell's Equations*. Oxford University Press, 2003.
- [MT98] V. A. Mandelshtam and H. S. Taylor. "Erratum: "Harmonic Inversion of Time Signals and its Applications"[J. Chem. Phys. 107, 6756 (1997)]". In: *The Journal of Chemical Physics* 109.10 (1998), p. 4128.
- [Mül+82] W. Müller, J. Krueger, A. Jacobus, R. Winz, T. Weiland, H. Euler, U. Hamm, and W. Novender. "Numerical Solution of 2- or 3-Dimensional Nonlinear Field Problems by Means of the Computer Program PROFI". In: *Archiv für Elektrotechnik* 65.4–5 (1982), pp. 299–307.
- [New59] N. M. Newmark. "A Method of Computation for Structural Dynamics". In: *Journal of the Engineering Mechanics Division, ASCE* 85.3 (1959), pp. 67–94.
- [OKJ09] A. F. Oskooi, C. Kottke, and S. G. Johnson. "Accurate Finite-Difference Time-Domain Simulation of Anisotropic Media by Subpixel Smoothing". In: *Optics Letters* 34.18 (2009), pp. 2778–2780.
- [Orao2] A. N. Oraevsky. "Whispering-Gallery Waves". In: *Quantum Electronics* 32.5 (2002), pp. 377–400.
- [Osk+10] A. F. Oskooi, D. Roundy, M. Ibanescu, P. Bermel, J. Joannopoulos, and S. G. Johnson. "Meep: A Flexible Free-Software Package for Electromagnetic Simulations by the FDTD Method". In: *Computer Physics Communications* 181.3 (2010), pp. 687–702.
- [Petoo] P. G. Petropoulos. "Numerical Dispersion and Absorbing Boundary Conditions". In: *International Journal of Numerical Modelling: Electronic Networks, Devices and Fields* 13.5 (2000), pp. 483–498.
- [RB02] T. Rylander and A. Bondeson. "Stability of Explicit–Implicit Hybrid Time-Stepping Schemes for Maxwell's Equations". In: *Journal of Computational Physics* 179.2 (2002), pp. 426–438.
- [Rie89] U. van Rienen. "Zur numerischen Berechnung zeitharmonischer elektromagnetischer Felder in offenen, zylindersymmetrischen Strukturen unter Verwendung von Mehrgitterverfahren". PhD thesis. Technische Hochschule Darmstadt, 1989.
- [RT06] V. S. Ryaben'kii and S. V. Tsynkov. *A Theoretical Introduction to Numerical Analysis*. CRC Press, 2006.

- [RW85] U. van Rienen and T. Weiland. “Triangular Discretization Method for the Evaluation of RF-Fields in Cylindrically Symmetric Cavities”. In: *IEEE Transactions on Magnetics* 21.6 (1985), pp. 2317–2320.
- [Scho5] M. Schauer. “Ein Beitrag zur Simulation statischer und niederfrequenter Felder in nichtlinearen und hochpermeablen Materialien”. PhD thesis. Technische Universität Darmstadt, 2005.
- [Sch99] R. Schuhmann. *Die Nichtorthogonale Finite-Integrations-Methode zur Simulation elektromagnetischer Felder*. Der Andere Verlag, 1999.
- [Sha49] C. Shannon. “Communication in the Presence of Noise”. In: *Proceedings of the IRE* 37.1 (1949), pp. 10–21.
- [Shy11] D. Shyrokı. “Modeling of Sloped Interfaces on a Yee Grid”. In: *IEEE Transactions on Antennas and Propagation* 59.9 (2011), pp. 3290–3295.
- [SWo1] R. Schuhmann and T. Weiland. “Conservation of Discrete Energy and Related Laws in the Finite Integration Technique”. In: *Progress In Electromagnetics Research* 32 (2001), pp. 301–316.
- [TCoo] F. L. Teixeira and W. C. Chew. “Complex Space Approach to Perfectly Matched Layers: A Review and Some New Developments”. In: *International Journal of Numerical Modelling: Electronic Networks, Devices and Fields* 13.5 (2000), pp. 441–455.
- [THo5] A. Taflove and S. C. Hagness. *Computational Electrodynamics: The Finite-Difference Time-Domain Method*. 3rd ed. Norwood, MA: Artech House, 2005.
- [TW96] P. Thoma and T. Weiland. “A Consistent Subgridding Scheme for the Finite Difference Time Domain Method”. In: *International Journal of Numerical Modelling: Electronic Networks, Devices and Fields* 9.5 (1996), pp. 359–374.
- [TW98] P. Thoma and T. Weiland. “Numerical Stability of Finite Difference Time Domain Methods”. In: *IEEE Transactions on Magnetics* 34.5 (1998), pp. 2740–2743.
- [WBC13] G. R. Werner, C. A. Bauer, and J. R. Cary. “A More Accurate, Stable, FDTD Algorithm for Electromagnetics in Anisotropic Dielectrics”. In: *Journal of Computational Physics* 255 (2013), pp. 436–455.
- [WC07] G. R. Werner and J. R. Cary. “A Stable FDTD Algorithm for Non-Diagonal, Anisotropic Dielectrics”. In: *Journal of Computational Physics* 226.1 (2007), pp. 1085–1101.

- [Wei77] T. Weiland. “A Discretization Model for the Solution of Maxwell’s Equations for Six-Component Fields”. In: *Archiv Elektronik und Übertragungstechnik* 31 (1977), pp. 116–120.
- [Wei79] T. Weiland. “Lossy Waveguides with Arbitrary Boundary Contour and Material Distribution”. In: *Archiv Elektronik und Übertragungstechnik* 33 (1979), pp. 170–174.
- [Wei83] T. Weiland. “On the Computation of Resonant Modes in Cylindrically Symmetric Cavities”. In: *Nuclear Instruments and Methods in Physics Research* 216.3 (1983), pp. 329–348.
- [Wei85] T. Weiland. “Three Dimensional Resonator Mode Computation by Finite Difference Method”. In: *IEEE Transactions on Magnetics* 21.6 (1985), pp. 2340–2343.
- [Wei96] T. Weiland. “Time Domain Electromagnetic Field Computation with Finite Difference Methods”. In: *International Journal of Numerical Modelling: Electronic Networks, Devices and Fields* 9.4 (1996), pp. 295–319.
- [Wilo8] F. Wilde. “Unidirectional Photoluminescence Emission of Pierced Microdisks”. PhD thesis. Universität Hamburg, 2008.
- [Yee66] K. Yee. “Numerical Solution of Initial Boundary Value Problems Involving Maxwell’s Equations in Isotropic Media”. In: *IEEE Transactions on Antennas and Propagation* 14.3 (1966), pp. 302–307.
- [ZSW03] I. Zagorodnov, R. Schuhmann, and T. Weiland. “A Uniformly Stable Conformal FDTD-Method in Cartesian Grids”. In: *International Journal of Numerical Modelling: Electronic Networks, Devices and Fields* 16.2 (2003), pp. 127–141.
- [ZW02] I. Zagorodnov and T. Weiland. “A Conformal Scheme for Wake Field Calculation”. In: *8th European Particle Accelerator Conference, Paris, France*. 2002, pp. 1682–1684.
- [ZYM91] S. Zivanovic, K. Yee, and K. Mei. “A Subgridding Method for the Time-Domain Finite-Difference Method to Solve Maxwell’s Equations”. In: *IEEE Transactions on Microwave Theory and Techniques* 39.3 (1991), pp. 471–479.

Own Publications

In chronological order

- [KKS16] S. Kirsch, L. Kuen, and R. Schuhmann. “Accurate Treatment of Non-conformal Material Interfaces in the Finite Integration Technique”. In: *IEEE Transactions on Magnetics* 52.3 (2016), pp. 1–4.
- [KCS14a] S. Kirsch, C. Classen, and R. Schuhmann. “A Material Averaging Scheme for the Finite Integration Technique Based on Local Field Information”. In: *Proceedings of the 10th International Conference on Scientific Computing in Electrical Engineering, Wuppertal, Germany*. 2014.
- [KS13c] S. Kirsch and R. Schuhmann. “Comparison of Cylindrical FDTD with Cartesian Subcell Modeling for Circularly Shaped Objects”. In: *Proceedings of Progress in Electromagnetics Research Symposium (PIERS), Stockholm, Sweden*. 2013, p. 1032.
- [KS13d] S. Kirsch and R. Schuhmann. “Cylindrical FDTD with Improved Time Step Size Based on Hybrid Newmark-Beta Discretization”. In: *Proceedings of URSI International Symposium on Electromagnetic Theory (EMTS), Hiroshima, Japan*. 2013, pp. 995–998.
- [KS12a] S. Kirsch and R. Schuhmann. “A Hybrid 2D/3D Cylindrical FDTD Method Based on Azimuthal Mode Decomposition”. In: *Proceedings of IEEE Antennas and Propagation Society International Symposium (APSURSI), Chicago, IL, USA*. 2012.
- [Kir10] S. Kirsch. “Absorbierende Randbedingungen für die kreiszylindrische Formulierung der Methode der Finiten Integration”. diploma thesis. Universität Paderborn, 2010.

Own Talks and Poster Presentations

In chronological order

- [KKS15a] S. Kirsch, L. Kuen, and R. Schuhmann. “Accurate Treatment of Nonconformal Material Interfaces in the Finite Integration Technique”. In: *KWT Workshop on Advances in Electromagnetic Research*. Poster presentation. Riezlern, Austria, 2015.
- [KKS15b] S. Kirsch, L. Kuen, and R. Schuhmann. “Accurate Treatment of Non-conformal Material Interfaces in the Finite Integration Technique”. In: *COMPUMAG*. Poster presentation. Montréal, Canada, 2015.

- [KCS14b] S. Kirsch, C. Classen, and R. Schuhmann. “A Material Averaging Scheme for the Finite Integration Technique Based on Local Field Information”. In: *Scientific Computing in Electrical Engineering (SCEE)*. Oral presentation. Wuppertal, Germany, 2014.
- [Kir+14] S. Kirsch, L. Kuen, C. Classen, and R. Schuhmann. “A Material Averaging Scheme for the Finite Integration Technique Based on Local Field Information”. In: *KWT Workshop on Advances in Electromagnetic Research*. Oral presentation. Hirschegg, Austria, 2014.
- [KS13a] S. Kirsch and R. Schuhmann. “Comparison of Cylindrical FDTD with Cartesian Subcell Modeling for Circularly Shaped Objects”. In: *Progress In Electromagnetics Research Symposium (PIERS)*. Poster presentation. Stockholm, Sweden, 2013.
- [KS13b] S. Kirsch and R. Schuhmann. “Comparison of Cylindrical FDTD with Cartesian Subcell Modeling for Circularly Shaped Objects”. In: *KWT Workshop on Advances in Electromagnetic Research*. Poster presentation. Riezlern, Austria, 2013.
- [KS13e] S. Kirsch and R. Schuhmann. “Cylindrical FDTD with Improved Time Step Size Based on Hybrid Newmark-Beta Discretization”. In: *International Symposium on Electromagnetic Theory (EMTS)*. Oral presentation. Hiroshima, Japan, 2013.
- [KS12b] S. Kirsch and R. Schuhmann. “A Hybrid 2D/3D Cylindrical FDTD Method Based on Azimuthal Mode Decomposition”. In: *IEEE International Symposium on Antennas and Propagation and USNC/URSI National Radio Science Meeting (AP-S URSI)*. Oral presentation. Chicago, IL, USA, 2012.
- [KS12c] S. Kirsch and R. Schuhmann. “A Hybrid 2D/3D Cylindrical FDTD Method Based on Azimuthal Mode Decomposition”. In: *KWT Workshop on Advances in Electromagnetic Research*. Oral presentation. Riezlern, Austria, 2012.
- [KS11] S. Kirsch and R. Schuhmann. “Energy Based Investigation of Numerical Stability for FDTD Schemes with Locally Refined Time Steps”. In: *KWT Workshop on Advances in Electromagnetic Research*. Poster presentation. Riezlern, Austria, 2011.
- [KS10] S. Kirsch and R. Schuhmann. “Some Extensions for FIT on Cylindrical Meshes”. In: *KWT Workshop on Advances in Electromagnetic Research*. Oral presentation. Waren, Germany, 2010.

Software

In alphabetical order

- [CST15] CST Computer Simulation Technology AG. *CST STUDIO SUITE*. 2015. URL: <https://www.cst.com/Products/CSTS2>.
- [Cur15] J. Currie. *OPTI Toolbox. Version 2.16*. 2015. URL: <http://www.i2c2.aut.ac.nz/Wiki/OPTI/index.php/Main/HomePage>.
- [GR09] C. Geuzaine and J.-F. Remacle. “Gmsh: A 3-D Finite Element Mesh Generator with Built-In Pre- and Post-Processing Facilities”. In: *International Journal for Numerical Methods in Engineering* 79.11 (2009), pp. 1309–1331.
- [Joho06] S. G. Johnson. *Harminv. Version 1.3.1*. 2006. URL: <http://ab-initio.mit.edu/wiki/index.php/Harminv>.
- [Mat14] MathWorks, Inc. *MATLAB 8.4.0*. 2014. URL: <http://mathworks.com/products/matlab/>.
- [Max15] Maxima. *Maxima, a Computer Algebra System. Version 5.37.0*. 2015. URL: <http://maxima.sourceforge.net/>.
- [MGH80] J. Moré, B. Garbow, and K. Hillstom. *User Guide for MINPACK-1*. Tech. rep. ANL-80-74. Argonne, IL, USA: Argonne National Laboratory, 1980.
- [Wol10] Wolfram Research, Inc. *Mathematica. Version 8.0*. 2010.